https://doi.org/10.15388/vu.thesis.173
https://orcid.org/0000-0002-3764-0605

VILNIUS UNIVERSITY
CENTER FOR NATURAL SCIENCES AND TECHNOLOGY

Agnė
ŠUMINIENĖ

Supercontinuum generation in semiconductor and narrow band gap dielectric crystals

DOCTORAL DISSERTATION

Natural Sciences
Physics (N 002)

VILNIUS 2021

This dissertation was written between 2017 and 2021 at Vilnius University Laser Research Center. The research was supported by the Research Council of Lithuania.

Academic supervisor:
prof. habil. dr. Audrius Dubietis (Vilnius University, Natural Sciences, Physics, N 002)

Dissertation Defense Panel:

Chairman – prof. dr. Aidas Matijošius (Vilnius University, Natural Sciences, Physics, N 002)

Members:
assoc. prof. dr. Vygandas Jarutis (Vilnius University, Natural Sciences, Physics, N 002)
dr. Audrius Pugžlys (Vienna University of Technology, Natural Sciences, Physics, N 002)
habil. dr. Virgilijus Vaičaitis (Vilnius University, Natural Sciences, Physics, N 002)
dr. Arūnas Varanavičius (Vilnius University, Natural Sciences, Physics, N 002)

The dissertation shall be defended at a public meeting of the Dissertation Defense Panel at 14:00 on 18th of June 2021 in Room 306 at Laser Research Center.
Address: Saulėtekio al. 10, Laser Research Center, Room 306, Vilnius, Lithuania.
Tel. +370 5 236 6005;

The text of this dissertation can be accessed at the Vilnius University Library, as well as on the website of Vilnius University:
www.vu.lt/naujienos/ivykiu-kalendorius

https://doi.org/10.15388/vu.thesis.173
https://orcid.org/0000-0002-3764-0605

VILNIAUS UNIVERSITETAS
FIZINIŲ IR TECHNOLOGIJOS MOKSLŲ CENTRAS

Agnė
ŠUMINIENĖ

Superkontinuumo generacija puslaidininkiuose ir siauros draustinės juostos dielektriniuose kristaluose

DAKTARO DISERTACIJA

Gamtos mokslai
Fizika (N 002)

VILNIUS 2021

Disertacija rengta 2017–2021 metais Vilniaus universitete, Lazerinių tyrimų centre. Mokslinius tyrimus rėmė Lietuvos mokslo taryba.

Mokslinis vadovas:
prof. habil. dr. Audrius Dubietis (Vilniaus universitetas, gamtos mokslai, fizika, N 002)

Gynimo taryba:

Pirmininkas – prof. dr. Aidas Matijošius (Vilniaus universitetas, gamtos mokslai, fizika, N 002)

Nariai:
doc. dr. Vygandas Jarutis (Vilniaus universitetas, gamtos mokslai, fizika, N 002)
dr. Audrius Pugžlys (Vienos technikos universitetas, gamtos mokslai, fizika, N 002)
habil. dr. Virgilijus Vaičaitis (Vilniaus universitetas, gamtos mokslai, fizika, N 002)
dr. Arūnas Varanavičius (Vilniaus universitetas, gamtos mokslai, fizika, N 002)

Disertacija ginama viešame Gynimo tarybos posėdyje 2021 m. birželio mėn. 18 d. 14:00 val. Lazerinių tyrimų centro 306 auditorijoje. Adresas: Saulėtekio al. 10, Lazerinių tyrimų centras, 306 aud., Vilnius, Lietuva.
Tel. +370 5 236 6005;

Disertaciją galima peržiūrėti Vilniaus universiteto bibliotekoje ir VU interneto svetainėje adresu: www.vu.lt/naujienos/ivykiu-kalendorius

CONTENTS

LIST OF ABBREVIATIONS

BBO	Beta barium borate, β-BaB_2O_4
BaF_2	Barium fluoride
CaF_2	Calcium fluoride
CCD	Charge-coupled device
DFG	Difference frequency generation
FS	Fused silica
FWHM	Full width at half maximum
GaAs	Gallium arsenide
GVD	Group velocity dispersion
GVM	Group velocity mismatch
IR	Infrared
KBr	Potassium bromide
KRS-5	Thallium bromo-iodide
KRS-6	Thallium bromo-chloride
KTA	Potassium titanyl arsenate
KTP	Potassium titanyl sulphate
LiF	Lithium fluoride
NaCl	Sodium chloride
OPA	Optical parametric amplification
OPCPA	Optical parametric chirped-pulse amplification
SBN	Strontium barium niobate
SC	Supercontinuum
Si	Silicon
SiC	Silicon carbide
SPM	Self-phase modulation
UV	Ultraviolet
YAG	Yttrium aluminium garnet
ZnSe	Zinc selenide
ZnS	Zinc sulfide

INTRODUCTION

Supercontinuum (SC) generation is a remarkable nonlinear phenomenon which can be observed in transparent media during propagation and filamentation of intense ultrashort laser pulses. SC can be described as an effect of extreme spectral expansion (the input laser pulse spectrum can expand hundreds or even thousands of times) caused by an intricate interplay of processes such as beam self-focusing, self-phase modulation, chromatic dispersion, nonlinear absorption, free electron plasma formation and more [1]. SC generation of femtosecond pulses was first observed back in 1983 [2], through the years it evolved together with our knowledge of nonlinear optics and with available femtosecond lasers, and has become a versatile, low-cost, robust, efficient and easy-maintenance source of broadband femtosecond coherent radiation in a wide range of wavelengths.

There is a number of effects governing femtosecond filamentation and supercontinuum generation during the femtosecond pulse nonlinear propagation in transparent solid-state media. Some of the most important effects are based on the third order optical susceptibility of the media, for example the effect of beam self-focusing. It stems from the optical Kerr effect which can be described as the dependence of the medium refractive index on the radiation intensity:

$$n = n_0 + n_2 I, \tag{1}$$

where n_0 and n_2 are the linear and nonlinear indexes of refraction, respectively and I is the radiation intensity. The nonlinear refractive index is linked to the third order optical susceptibility of the material:

$$n_2 = \frac{3}{4n_0^2 c\epsilon_0}\chi^{(3)}(\omega;\omega,\omega,-\omega), \tag{2}$$

where c is the speed of light in vacuum, ϵ_0 is the vacuum permittivity and $\chi^{(3)}(\omega;\omega,\omega,-\omega)$ is the third order nonlinear optical susceptibility.

Evidently, the nonlinear index of refraction is linearly proportional to the third order optical susceptibility. Therefore, an intense Gaussian beam travelling in a medium with a positive nonlinear refractive index, will self-focus - the more intense central part of the beam will experience a larger refractive index than the less-intense beam periphery. In other words, the material will act as a convex lens. If the nonlinear refractive index is negative, the material will act as a concave lens and the beam will self-defocus.

The self-focusing threshold is described by the critical power for self-focusing

P_{cr}. It is defined as the power needed for the self-focusing effect to fully compensate the diffractive spreading of the laser beam and for a Gaussian beam is defined as follows:

$$P_{cr} = \frac{3.77\lambda^2}{8\pi n_0 n_2}, \tag{3}$$

where λ is the radiation wavelength. When the beam power is greater than P_{cr}, the beam will self-focus at a distance described by the Marburger law [3]:

$$z_{sf} = \frac{0.367 z_R}{\sqrt{[(P/P_{cr})^{1/2} - 0.852]^2 - 0.0219}}, \tag{4}$$

where $z_R = \pi n_0 w_0^2/\lambda$ denotes the Rayleigh (diffraction) length of the input Gaussian beam of a radius w_0, taken at $1/e^2$ intensity level. Although Eq. (4) is generally derived in the case of continuous wave laser beams, it gives a fairly accurate approximation of the nonlinear focus for femtosecond laser pulses as well [4].

Another phenomenon determined by the nonlinear refractive index is pulse self-phase modulation and it is sometimes referred to as a temporal analogue for beam self-focusing. Time-dependent intensity causes the refractive index of the medium to change in time which induces a nonlinear phase shift:

$$\phi_{nl} = \frac{\omega_0}{c} n_2 I(t) z, \tag{5}$$

where ω_0 is the carrier frequency, $I(t)$ is the time-varying intensity and z is the propagation distance. The nonlinear phase shift accumulates together with the increasing propagation distance. A time-dependent phase determines the change of the instantaneous frequency, therefore one can write:

$$\delta\omega(t, z) = \frac{\partial \phi_{nl}(t)}{\partial t} = \frac{\omega_0 z}{c} n_2 \frac{\partial I(t)}{\partial t}, \tag{6}$$

where $\phi_{nl}(t)$ is the time-varying nonlinear phase. As can be seen, the phase modulation of the pulse causes the pulse carrier frequency modulation, i. e. the spectrum of the pulse is enriched with new frequency components and it becomes broader. For a Gaussian pulse with a duration of t_p, the change of the instantaneous frequency can be described as:

$$\delta\omega(t,z) = -2\frac{\omega_0 tz}{ct_p^2} n_2 I_0 exp(-\frac{t^2}{t_p^2}), \tag{7}$$

where I_0 is the peak intensity. If the nonlinear index of refraction is positive, the front of the pulse will experience a negative (Stokes) and the back of the pulse - a positive (anti-Stokes) frequency shift, that is the front of the pulse will be supplemented with red and the back of the pulse - with blue spectral components. The opposite is true, if $n_2 < 0$.

The formation of light filaments can be seen as a dynamic balance between the cycles of self-focusing and defocusing [5]. Once the power of the wavepacket exceeds the critical power of self-focusing, it should shrink into infinitesimally small dimensions and reach spatial collapse while the intensity approaches infinity. However, in reality after reaching the sufficient intensity, which usually happens when approaching the nonlinear focus, certain effects such as multiphoton absorption, free electron plasma generation and plasma absorption restrict the light beam from collapse. Through the multiphoton absorption, electrons are excited and transfer into the conduction band, thus forming free electron plasma, characteristic of which is a negative nonlinear index of refraction, and as a consequence, the beam is defocused. This effect is called intensity clamping. Therefore, the most intense central part of the beam experiences nonlinear losses and electron plasma defocusing. On the other hand, if the power of the wavepacket still exceeds the P_{cr}, the beam is able to self-focus for the second time and the cycle continues.

The spatial structure of the femtosecond light filament is rather complex: it consists of an intense central peak and a low-intensity, high-energy periphery shaped as concentric rings around the filament core. During the nonlinear propagation, only the central part of a filament interacts with the media while the energy losses are replenished by the beam periphery, acting as an energy reservoir. Only around 10% of the filament energy is located at the central peak which, if blocked, self-reconstructs from the periphery. However, if the periphery is blocked, the central peak readily experiences diffraction and dissipates. Therefore, light filaments can be treated as conical beams [6].

Femtosecond filamentation and nonlinear propagation are closely intertwined with the phenomenon of supercontinuum generation. It has been shown experimentally that the threshold power for SC generation is slightly above the critical power for self-focusing. Spectral broadening during the SC generation is governed by a number of physical factors, one of which is the order of multiphoton absorption:

$$K = \langle U_g/\hbar\omega_0 \rangle + 1, \tag{8}$$

where U_g is the energy band gap of the medium, and $\hbar\omega_0$ is the incident photon energy. The higher the order of multiphoton absorption, the higher the intensity can be reached within the nonlinear focus before the intensity clamping sets in and thus, the broader SC spectrum can be achieved [7, 8]. Consequently, the broadest SC spectra are demonstrated in wide band gap dielectrics. On the other hand, if the order of multiphoton absorption is smaller than 3, SC generation is not possible. Another interesting observation has been made about the relationship between the medium band gap and the nonlinear refractive index: the larger is the energy bandgap, the smaller is n_2 [9]. Finally, according to the numerical modeling results, the chromatic dispersion of the medium is also an important characteristic when considering the width and shape of SC spectrum. The influence of dispersion can be accounted for by applying the model of effective three-wave mixing when SC generation is considered as the generation of new frequencies caused by the incident optical field scattering via nonlinear polarization [10, 11]. To put it more simply, lower material dispersion ensures the fulfillment of the phase matching conditions for a broader range of frequencies.

Temporal and spectral SC generation dynamics also depend on the material dispersion which can be described as the group velocity dispersion (GVD) coefficient:

$$GVD = k_0^{''} = \partial^2 k/\partial\omega^2|_{\omega_0}, \tag{9}$$

where $k = \omega_0 n_0/c$ is the wavenumber. If the GVD is positive (or normal), the red-shifted frequency components in the medium travel faster than the blue-shifted ones. If the GVD is negative (or anomalous), the opposite is true. Qualitatively three regimes of SC generation are distinguished depending on the GVD coefficient for the pump wavelength: the normal, zero and anomalous GVD.

In the case of normal GVD, SC generation dynamics are governed by temporal pulse-splitting. Self-phase modulation ensures that new red-shifted frequency components emerge at the front and blue-shifted components - at the back of the pulse. The positive GVD of the material separates the red-shifted and the blue-shifted components even further and causes pulse splitting at the nonlinear focus after which two sub-pulses with different carrier frequencies emerge. Therefore, in the time frame of the initial pulse, the formed sub-pulses move in different directions. Pulse splitting event is followed by an abrupt spectral broadening which is caused by the self-steepening of the fronts of the sub-pulses. The self-steepening occurs due to different velocities between the intense sub-pulse peak and the low intensity tail. This results in a remarkable intensity gradient in the temporal pulse profile. The scale of self-steepening for the two sub-pulses is different which explains the asymmetric broadening of the SC spectrum. Upon typical focusing conditions, an especially steep front is formed at the back of the second sub-pulse which is responsible for the spectral blue-shift. The spectral red-shift is less pronounced since the steepening of the front of the first pulse is not as strong. Such explanation of SC generation dynamics in the normal GVD regime has been experimentally proven and seems to be universal for various nonlinear media [12].

When the pump pulse wavelength falls into the anomalous GVD region of the medium, a completely different SC generation scenario takes place. In this case, the beam self-focusing, self-phase modulation and the anomalous GVD of the material force the wavepacket to self-compress both in space and time, leading to the formation of a light bullet [13]. Due to self-phase modulation, the leading front of the pulse is supplemented with red-shifted spectral components which, due to the anomalous GVD, move slower than the blue-shifted components, which emerge at the trailing front of the pulse. Therefore, both red- and blue-shifted components move towards the center of the pulse and temporal compression takes place. Numerical modeling has confirmed the described spectral and spatiotemporal dynamics and the potential for self-compression of the pulse to a single optical cycle [14–16].

Lastly, if the pump pulse wavelength coincides with the zero GVD of the medium, the dynamics of SC generation shares characteristics from both normal and anomalous GVD regimes. SC spectra produced in the zero GVD regime are rather symmetric, unlike those generated in the normal GVD case which demonstrate a much larger blue-shift. In the temporal domain, the zero GVD SC generation scenario includes pulse-splitting at the nonlinear focus, that is the temporal dynamics of the wave-packet resembles the case of normal GVD. It has been shown that even a weakly anomalous GVD is not able to ensure the compression of a spectrally broadened pulse and stop pulse-splitting [17].

Supercontinuum generation has been known for quite some time as a compact, versatile and efficient way of producing broadband femtosecond radiation in the visible spectral region. However, with rapidly growing fields such as development of OPCPA [18], vibrational spectroscopy [19, 20], semiconductor optoelectronics [21], frequency comb technology [22], gas detection [23], etc., recently there has been an increasing demand for broadband coherent femtosecond radiation in the near and mid-infrared. Supercontinuum generation in the infrared spectral region can easily meet the demand for such radiation. However, the most popular media for SC generation in the visible and near-infrared spectral range like sapphire, YAG and fused silica are not applicable in the mid-infrared due to their absorption edge being in this region: fused silica starts absorbing at 3.5 μm and the absorption of sapphire and YAG starts at around 5.2 μm [24]. Also, with longer pump wavelengths, SC spectra produced in fluoride crystals, such as BaF_2 and CaF_2 become discontinuous and show detached peaks [25,26]. Therefore, SC generation in the infrared requires different materials with certain optical properties.

Recent experimental and theoretical investigations show that there is a number of alternative materials such as narrow band gap dielectrics which have the potential of being suitable for SC generation in the infrared spectral range. It should be noted that in the scope of this dissertation narrow band gap dielectrics are considered those whose energy band gap does not exceed 4.5 eV. Dielectric crystals whose band gap is greater than 4.5 eV are referred to as wide band gap. Broadband SC generation spanning into the mid-infrared has been demonstrated in fluoride [27], tellurite [28,29], lanthanum [30] and chalcogenide [31] glasses. Furthermore, due to their increased transparency in the mid-infrared spectral region and large values of nonlinear refractive index, semiconductor crystals also emerge as attractive nonlinear media for mid-IR SC generation. Up to date, experiments have been carried out in GaAs demonstrating multi-octave femtosecond SC generation in the mid-IR with excellent temporal compression to few-cycle duration [32–34]. Successful broadband femtosecond SC generation spanning from the mid-IR to the visible spectral range was also reported in polycrystalline semiconductor materials, such as ZnS and ZnSe crystals [35–37]. However, from the abundance of the materials with attractive properties for SC generation in the infrared, only a small amount were thoroughly investigated so far.

The objective of the thesis

The objective of this dissertation is investigation of femtosecond filamentation and supercontinuum generation in narrow energy band gap dielectric and semiconductor crystals in the near- and mid-infrared spectral range.

The main tasks of the thesis

- Development of a femtosecond mid-infrared light source based on difference frequency generation, delivering pulses in the 3-5 μm spectral range which serve as a pump for supercontinuum generation in the nonlinear materials of interest.
- Experimental study of supercontinuum generation in narrow band gap dielectric crystals thallium bromoiodide (KRS-5), thallium bromochloride (KRS-6) and strontium barium niobate (SBN) and semiconductor crystals silicon and silicon carbide (6H-SiC) with femtosecond pump pulses tunable in the 1.2-4.7 μm spectral range.
- Measurement of spatiotemporal intensity distributions at various stages of femtosecond filament formation in bulk silicon.

- Investigation of the influence of color centers on supercontinuum generation in alkali halide crystals NaCl and KBr when pumping with mid-infrared femtosecond laser pulses.

Practical and scientific novelty

- A compact mid-infrared laser source based on difference frequency generation, providing 60-130 fs pulses of up to 11 μJ in the 3-5 μm spectral region was developed which was used in femtosecond filamentation and supercontinuum generation experiments.
- A simple method for evaluation of material nonlinear refractive index by measurement of nonlinear energy transmission during femtosecond filamentation was proposed. Using this method n_2 of KRS-5, KRS-6 and SBN crystals was evaluated.
- It was demonstrated that narrow band gap dielectrics such as KRS-5, KRS-6, SBN together with undoped semiconductor crystals like silicon and 6H-SiC are suitable materials for efficient supercontinuum generation in the infrared spectral range when pumped by near- and mid-infrared femtosecond laser pulses.
- It was shown that pulse splitting during supercontinuum generation in silicon crystal with input pulse wavelength falling in the normal group velocity dispersion region of the material is a universal physical characteristic of femtosecond filamentation in undoped semiconductors as well as in dielectrics.
- It was demonstrated that ultrabroadband multi-octave infrared supercontinuum spectra generated in alkali metal halide crystals NaCl and KBr are prone to a rapid narrowing due to color center formation which effectively decreases the energy band gap.

Statements to be defended

1. Broad infrared transmittance and high cubic nonlinearity of narrow band gap dielectric (KRS-5, KRS-6, SBN) and semiconductor (silicon and 6H-SiC) crystals ensure low energy threshold femtosecond supercontinuum generation with more than an octave spanning spectra in the infrared.
2. Energy transmission measurements of a light filament allows to pinpoint the nonlinear focus formation at the back face of the medium that can be used to evaluate the nonlinear refractive index of the material using Marburger's law.

3. Color center formation in alkali metal halides NaCl and KBr results in narrowing of the effective energy band gap of the material which leads to supercontinuum spectral shrinking and decrease of energy transmittance.
4. Femtosecond filamentation in undoped semiconductor media with incident pulse wavelength falling into normal group velocity dispersion region of the material results in splitting of the input pulse into two sub-pulses.
5. Undoped semiconductor and narrow band gap dielectric crystals exhibit a fairly stable cut-off wavelength of supercontinuum spectrum and increasing blue-shift with increasing the pump wavelength, indicating that group velocity dispersion of the material and the order of multiphoton absorption are the main factors which define the extent of supercontinumm spectrum in these materials.

Layout of the dissertation

The dissertation is prepared on the basis of a set of six scientific articles. The *Experimental Methods* section is dedicated to descriptions of our built mid-IR laser source (based on article A1) along with other laser sources, measurement equipment and methods used in all of the performed experiments. Two dissertation chapters are organized to consist of supercontinuum generation experiments in narrow band gap dielectrics (Chapter 1, based on articles A2, A3 and A4) and in semiconductor crystals (Chapter 2, based on articles A5 and A6).

Contribution of the author

The main co-authors of the results presented in this thesis in no particular order are: dr. Rosvaldas Šuminas, dr. Vytautas Jukna, dr. Nail Garejev, dr. Gintaras Tamošauskas and prof. habil. dr. Audrius Dubietis. Detailed contributions can be found in the *Acknowledgements* section. Contribution of the author for the publications this thesis is based on is as follows:

A1 - assembled the experimental setup of the OPA source (DFG and OPA stage), performed experiments and carried out data analysis and presentation for publishing.

A2, A3, A5 - performed experiments, carried out data analysis and presentation for publishing.

A4 - performed experiments.

A6 - performed experiments, carried out data analysis and presentation for publishing, prepared the initial draft of the article.

LIST OF PUBLICATIONS

On the dissertation topic

[A1] **A. Marcinkevičiūtė**, N. Garejev, R. Šuminas, G. Tamošauskas, A. Dubietis, A compact, self-compression-based sub-3 optical cycle source in the 3-4 μm spectral range, J. Opt. **19**, 105505 (2017).

[A2] **A. Marcinkevičiūtė**, G. Tamošauskas, A. Dubietis, Supercontinuum generation in mixed thallous halides KRS-5 and KRS-6, Opt. Mater. **78**, 339–344 (2018).

[A3] **A. Marcinkevičiūtė**, V. Jukna, R. Šuminas, N. Garejev, G. Tamošauskas, A. Dubietis, Supercontinuum generation in the absence and in the presence of color centers in NaCl and KBr, Results Phys. **14**, 102396 (2019).

[A4] R. Šuminas, N. Garejev, **A. Šuminienė**, V. Jukna, G. Tamošauskas, A. Dubietis, Femtosecond filamentation, supercontinuum generation, and determination of n_2 in polycrystalline SBN, J. Opt. Soc. Am. B **37**(4), 1530–1534 (2020).

[A5] **A. Marcinkevičiūtė**, V. Jukna, R. Šuminas, N. Garejev, G. Tamošauskas, A. Dubietis, Femtosecond filamentation and supercontinuum generation in bulk silicon, Opt. Lett. **44**(6), 1343–1346 (2019).

[A6] **A. Šuminienė**, V. Jukna, R. Šuminas, G. Tamošauskas, A. Dubietis, Femtosecond infrared supercontinuum generation in 6H-SiC, OSA Continuum **4**(3), 911–917 (2021).

Other publications

- [A7] **A. Šuminienė**, V. Jukna, R. Šuminas, G. Tamošauskas, M. Vengris, A. Dubietis, LiSAF: an efficient and durable nonlinear material for supercontinuum generation in the ultraviolet, Lith. J. Phys. **60**(4), 217–224 (2020).
- [A8] R. Šuminas, **A. Marcinkevičiūtė**, G. Tamošauskas, A. Dubietis, Even and odd harmonics-enhanced supercontinuum generation in zinc-blende semiconductors, J. Opt. Soc. Am. B **36**(2), A22–A27(2019).
- [A9] **A. Marcinkevičiūtė**, K. Michailovas, R. Butkus, Generation and parametric amplification of broadband chirped pulses in the near-infrared, Opt. Commun. **415**, 70–73 (2018).
- [A10] K. Stankevičiūtė, I. Pipinytė, J. Vengelis, **A. Marcinkevičiūtė**, R. Šuminas, R. Grigonis, R. C. Eckardt, V. Sirutkaitis, Optical parametric oscillators synchronously pumped by fundamental and second harmonic radiation of femtosecond Yb:KGW laser, Proc. SPIE **8845**, 884519(2013).

Conference presentations

- [C1] **A. Marcinkevičiūtė**, V. Jukna, R. Šuminas, G. Tamošauskas, A. Dubietis, Influence of color centers on filamentation and supercontinuum generation in alkali metal halides NaCl and KBr, Ultrafast Optics UFO XII, Bol, Croatia, 2019.
- [C2] R. Šuminas, N. Garejev, **A. Marcinkevičiūtė**, V. Jukna, G. Tamošauskas, A. Dubietis, Filamentation and supercontinuum generation in polycrystalline strontium barium niobate (SBN) using infrared femtosecond laser pulses, Ultrafast Optics UFO XII, Bol, Croatia, 2019.
- [C3] **A. Marcinkevičiūtė**, V. Jukna, R. Šuminas, S. Balandytė, G. Tamošauskas, A. Dubietis, Femtosecond filamentation of mid-infrared pulses in bulk silicon, 8th EPS-QEOD Europhoton Conference, Barcelona, Spain, 2018.
- [C4] R. Šuminas, J. Lukošiūnas, **A. Marcinkevičiūtė**, G. Tamošauskas, A. Dubietis, Filamentation induced ultrabroadband nonlinear interactions in polycrystalline zinc-blende semiconductors, 8th EPS-QEOD Europhoton Conference, Barcelona, Spain, 2018.
- [C5] **A. Marcinkevičiūtė**, V. Jukna, R. Šuminas, S. Balandytė, G. Tamošauskas, A. Dubietis, Filamentation of femtosecond mid-infrared pulses in crystalline silicon, 11th International Conference on Photo-Excited Processes and Applications, Vilnius, Lithuania, 2018.

[C6] R. Šuminas, J. Lukošiūnas, **A. Marcinkevičiūtė**, G. Tamošauskas, A. Dubietis, Simultaneous ultrabroadband nonlinear interactions in polycrystalline ZnS and ZnSe, 11th International Conference on Photo-Excited Processes and Applications, Vilnius, Lithuania, 2018.

[C7] **A. Marcinkevičiūtė**, N. Garejev, R. Šuminas, G. Tamošauskas, A. Dubietis, Keleto optinių ciklų trukmės impulsų generacija ir spūda 3-4 µm spektrinėje srityje, 42-oji Lietuvos nacionalinė fizikos konferencija, Vilnius, Lithuania, 2017.

[C8] G. Tamošauskas, G. Beresnevičius, J. Lukošiūnas, **A. Marcinkevičiūtė**, A. Dubietis, Vienalaikis femtosekundinių impulsų charakterizavimas dažnių skyros laiko sklendės (FROG) metoduploname BBO kristale 1,3 - 4 µm spektro srityje, 42-oji Lietuvos nacionalinė fizikos konferencija, Vilnius, Lithuania, 2017.

EXPERIMENTAL METHODS

This chapter describes the developed mid-IR femtosecond pulse source used in the experiments of the thesis together with other laser sources, equipment and measurement techniques. Also, main parameters of the pump laser pulses and investigated nonlinear media are given at the end of the chapter. If needed, more in-depth descriptions of the experimental methods can be found in the reprinted publications.

A COMPACT FEMTOSECOND LASER SOURCE IN THE MID-INFRARED

Firstly, in order to carry out femtosecond filamentation and supercontinuum generation in the mid-infrared spectral range in various nonlinear media, a suitable femtosecond laser source is needed. Together with providing femtosecond pulses in the mid-infrared spectral region, it also should be wavelength-tunable, thus allowing to access different filamentation regimes according to the dispersive properties of the nonlinear materials that are being investigated.

Development of laser sources, which emit ultrashort pulses in the mid-infrared spectral range is dictated by the emerging applications in ultrafast vibrational spectroscopy, mid-infrared nonlinear optics and strong-field physics [38]. Generation of mid-infrared pulses with durations as short as few optical cycles is exclusively based on the optical parametric amplification, which supports large amplification bandwidths necessary to maintain short pulse widths, see e.g. [39].

Technically simple, low cost and easily implementable setups for generation of ultrashort mid-infrared pulses rely on using widely available amplified femtosecond Ti:sapphire driving lasers. Several configurations that involve optical parametric amplification, difference frequency generation (DFG), or both, have been demonstrated so far. The first configuration is based on either collinear or noncollinear optical parametric amplification in bulk and periodically poled nonlinear crystals, extracting the idler wave, which lies in the mid-infrared spectral range. Here the fundamental laser wavelength (800 nm) serves as a pump, while the seed signal is provided by either supercontinuum (SC) generation in bulk dielectric media or using the idler pulses produced by the near-infrared optical parametric amplifier (OPA). To this end, OPAs based on nonlinear crystals which possess transparency and phase matching in the mid-infrared, such as potassium titanyl phosphate (KTP) and potassium titanyl arsenate (KTA) [40, 41], potassium niobate ($KNbO_3$) [40–45], lithium niobate ($LiNbO_3$) [41, 44–46], lithium iodate ($LiIO_3$) [47] and periodically poled stoichiometric lithium tantalate [48] crystals were demonstrated to provide pulses with durations from sub-100 fs to few optical cycles in the 2–5 µm wavelength range.

The second configuration employs DFG between the signal and idler pulses from the near-infrared OPA (e.g. that based on commonly used BBO crystal), see e.g. [49]. The third configuration uses DFG between broadband pulses from second harmonic-pumped noncollinear OPA and the fundamental laser pulses, providing few optical cycle pulses with stable carrier envelope phase, which are subsequently amplified in a broadband OPA [38, 50, 51].

The experimental scheme of our mid-infrared laser source is depicted in Fig. 1. The entire setup is driven by regeneratively amplified Ti:sapphire system (Spitfire PRO, Newport-Spectra Physics), which delivers 100 fs pulses at 800 nm with an energy up to 3 mJ at a repetition rate of 1 kHz. A fraction of the laser energy (0.9 mJ) was used to pump a commercial BBO crystal-based OPA (Topas-Prime, Light Conversion Ltd.), which provided the near-infrared signal and idler pulses with energies in the range of 100-150 μJ and sub-100 fs pulsewidths.

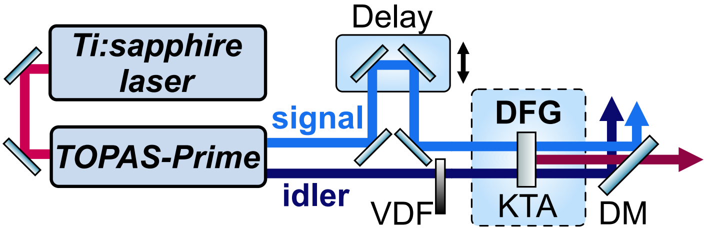

Figure 1: Schematic of the mid-infrared laser source. DFG - difference frequency generation, VDF - variable density filter, DM - dielectric mirror.

The difference frequency generation between the o-polarized signal and e-polarized idler pulses was performed in a 1 mm thick KTA crystal, cut for type II phase matching ($\theta = 43$, $\phi = 0$), which provides broad conversion bandwidth in the wavelength range of interest [52]. Proper timing between the input signal and idler pulses entering the DFG crystal was set by adjusting the temporal delay stage, hence compensating their temporal walk-off originating in BBO OPA. The DFG stage delivered o-polarized pulses tunable in a 3-4.7 μm spectral region and with pulsewidths ranging from 60 to 130 fs and energy of up to 11 µJ. If needed, smaller energy of the DFG radiation was achieved by translation of the variable density filter (NDL-25C-2, Thorlabs Inc.) placed in the optical path of an idler wave.

It should be noted that our mid-IR femtosecond pulse source also had an OPA stage, based on 1 mm $LiIO_3$ crystal cut for type-I phase matching, pumped by fundamental 800 nm, 0.7 mJ laser pulses. After the DFG stage, 3.5 μm pulses were amplified up to 35 μJ and later self-compressed in a 4 mm thick CaF_2 plate down to 31 fs (or 2.7 optical cycles) with an energy throughput of

93.5%. By tuning the wavelength of the nonlinear stages, we also demonstrated lossless self-compression of 3 μm, 31 μJ and 70 fs pulses in 3 mm thick YAG plate down to 31 fs (2.3 optical cycles) and self-compression of 4 μm, 14 μJ, 97 fs pulses down to 42 fs (3.2 optical cycles) in BaF_2 plate of 4 mm. However, the OPA and self-compression stages were not used in the experiments of this dissertation, since the DFG stage provided pulses of sufficient energy for femtosecond filamentation in the studied materials and the short durations of the self-compressed pulses would have readily increased due to dispersion of the optical elements of our setup.

EXPERIMENTAL EQUIPMENT

- BBO crystal-based optical parametric amplifier (Topas-Prime, Light Conversion, Ltd.), providing 1.2-2.4 μm, sub-100 fs, 100-150 μJ pulses.
- Non-collinear optical parametric amplifier pumped by second harmonic radiation of Ti:sapphire laser (Topas-White, Light Conversion Ltd.) provides 20-30 fs, 530-720 nm pulses of up to 30 μJ energy. The pulses were used for gating in spatiotemporal imaging measurements, described in Section 1.2.
- Home-built scanning prism spectrometer equipped with Si, Ge, PbSe and InAsSb detectors (either one or two at a time) offering an effective detection range of 0,2-5,8 μm. High dynamic range is ensured by a rotating wheel of neutral density filters after the end slit of the spectrometer. This device was used for spectral measurements throughout all of the experiments.
- Microbolometer camera (WinCamD-FIR2-16-HR, DataRay), pixel size 17 μm, 14-bit dynamic range. Used for beam measurements of both input beams and light filaments in all of the experiments.
- DSLR camera (Nikon D7200) used for imaging the filament-induced colour center traces in Section 2.1.
- CCD camera (Grasshopper 2, Point Grey), pixel size 4.4 μm, 14-bit dynamic range. Used for spatiotemporal imaging in Section 1.2.
- Spectrophotometer (Shimadzu UV-3101PC) with 190-3200 nm spectral range and 0.1 nm resolution. Used for transmission measurements of the samples in Section 1.1.

MEASUREMENT METHODS

A generalized schematic of the experiments is depicted in Fig 2. Part of the infrared femtosecond pump radiation (either from the near-infrared OPA, or our developed mid-infrared source) of the chosen wavelength and energy is reflected towards a reference energy detector by a reference plate. Further, the transmitted radiation is focused by a plano-convex BaF_2 lens onto the entrance face of the sample of the nonlinear medium. The focal length of the lense used was chosen in a way that loose focusing conditions would be ensured. Upon escaping the sample the beam is imaged onto a particular unit of diagnostic equipment (slit of the spectrometer, microbolometric camera, energy detector, etc.) via silver-coated parabolic mirrors arranged in a 4f-imaging geometry.

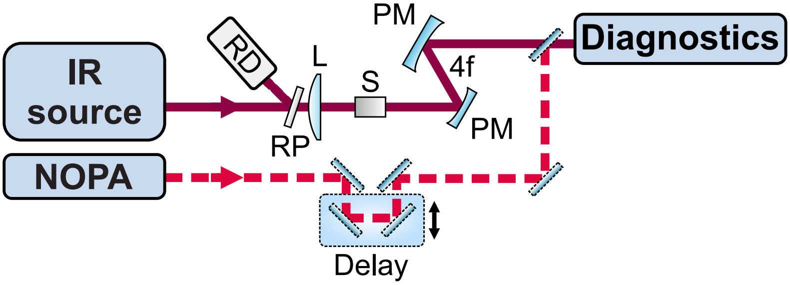

Figure 2: Generalized experimental scheme, RD - reference detector, RP - reference plate, L - lens, S - sample, PM - parabolic mirror, NOPA - noncollinear optical parametric amplifier.

Several techniques for spectral, temporal and energy measurements of light filament were used throughout the experiments.

Firstly, in sections 1.1, 1.2 and 2.2 energy transmission measurements were carried out in a following way. Two detectors were used for simultaneous measurement of the pulse energy before and after the nonlinear propagation in the sample. The input pulse energy was varied by automated translation of the variable density filter.

Also in section 2.1 light pulses were characterized by implementing spatiotemporal imaging, alternatively termed as three dimensional laser tomography. A series of cross-correlation images were taken with a CCD camera while varying the time delay between the object and the reference pulses thus unveiling the spatiotemporal dynamics of a wave-packet during light filamentation. Cross-correlation functions were measured in 20 μm-thick BBO crystal using 27 fs 720 nm reference pulses from the NOPA source in order to ensure appropriate sum frequency conversion bandwidth and temporal resolution.

Finally, a homebuilt intensity autocorrelator based on 20 μm-thick BBO crystal was used for measuring the input pulse durations.

Table 1: Summary of the main parameters of the input radiation and nonlinear media samples investigated in Chapter 1, L - thickness of the sample, E_g - energy bandgap, T - transmission, λ_0 - zero GVD wavelength, τ - pulse duration, λ - pump wavelength, ω - beam radius taken at $1/e^2$ intensity level.

Material	KRS-5 (58% mol TlI)	KRS-6 (60% mol TlCl)	NaCl	KBr	SBN:61
L (mm)	2; 6	2; 6	5	5	5
E_g (eV)	$2.5^{(d)}$	$3.25^{(d)}$	$9^{(a)}$	$7.6^{1(a)}$	$3.4^{(a)}$
T (μm)	0.58-$42^{(a)}$	0.42-$27^{(a)}$	0.17-$18^{(a)}$	0.2-$30.6^{(a)}$	0.45-$5.5^{(a)}$
λ_0 (μm)	$6.6^{(e)}$	-	$2.76^{(a)}$	$3.83^{(a)}$	$1.96^{(b)}$
n_2 ($\times 10^{-16}$ cm^2/W)	$98^{(c)}$	$39^{(c)}$	$4.35^{(c)}$	$7.95^{(c)}$	$52.4^{(c)}$
λ (μm)	3.1; 3.6	3.1; 3.6	3.6	3.6	1.2; 2.0; 2.4
τ (fs)	60	60	60	60	85; 95; 125
ω (μm)	40; 70	40; 70	55	55	36; 54; 53

$^{(a)}$ The transmission range is taken from [24] and defined at 10% transmission level in a 1 mm thick sample.
$^{(b)}$ Data taken from [53].
$^{(c)}$ Evaluated according to the method provided in [54] with an updated parameter K from [55].
$^{(d,e)}$ Data taken from [56, 57].

This section provides a brief summary of input pulse and nonlinear media parameters used throughout the experiments in a form of two separate tables for two chapters of this dissertation, respectively. Also, the GVD plots of the investigated materials are given at the end of the section.

GVD curves for KRS-5 (thallium bromoiodide, Tl(Br, I)) and KRS-6 (thallium bromochloride, Tl(Cl, Br)) are depicted in Fig. 3. It should be noted that there is a lack of knowledge on the dispersion of KRS-6. The available dispersion equation for KRS-6 with a composition of 60 mol% TlCl is based on the Sellmeier coefficients reported many years ago, in 1948, which gives the zero GVD wavelength of KRS-6 at 1.6 µm [62]. However, another KRS-6 GVD (68 mol % of TlCl) curve derived from newer measurements is available only in the visible range [63]. If it is extended into the infrared, a stark difference between the two GVD curves for KRS-6 can be observed, as seen from Fig. 3.

Table 2: Summary of the main parameters of the input radiation and nonlinear media samples investigated in Chapter 2, L - thickness of the sample, E_g- energy bandgap, T - transmission, λ_0 - zero GVD wavelength, τ - pulse duration, d - beam diameter taken at $1/e^2$ intensity level.

Material	Si	6H-SiC
L (mm)	6.4	5
E_g (eV)	1.124(e)	2.6(c)
T (μm)	1.1-6.5(a)	0.5-4(a)
λ_0 (μm)	>23(e)	2.1(f)
n_2 ($\times 10^{-16}$ cm^2/W)	270(g)	86(h)
λ (μm)	3.25; 3.6; 4.0; 4.7	1.3; 1.5; 1.7; 2.0; 2.2; 2.4
τ (fs)	60; 60; 125; 110	87; 95; 85; 95; 127; 125
d (μm)	60; 60; 68; 73	75; 85; 90; 105; 110; 125

(a) The transmission range is taken from [24] and defined at 10% transmission level in a 1 mm thick sample.
(b−h) Data taken from [24, 56–61].

Given this large mismatch, in our view the zero GVD wavelength of KRS-6 at 1.6 µm from the dispersion equation taken from [62] could not be considered as reliable.

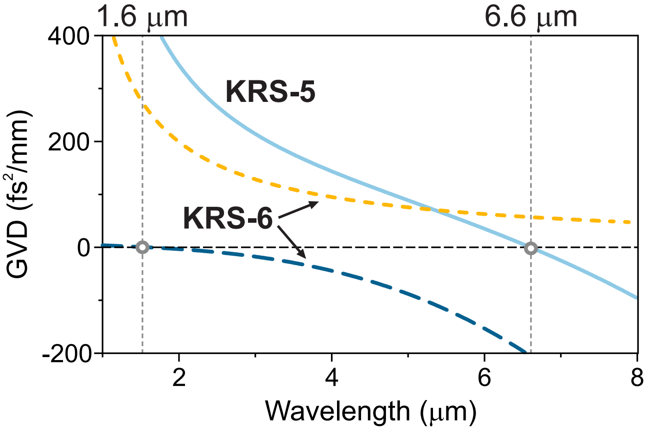

Figure 3: GVD of KRS-5 (solid, light blue line [57]) and two GVD curves for KRS-6, (short-dashed, yellow line [63] and long-dashed dark blue line [62]). Grey hollow circles together with dashed grey vertical lines denote zero GVD wavelengths.

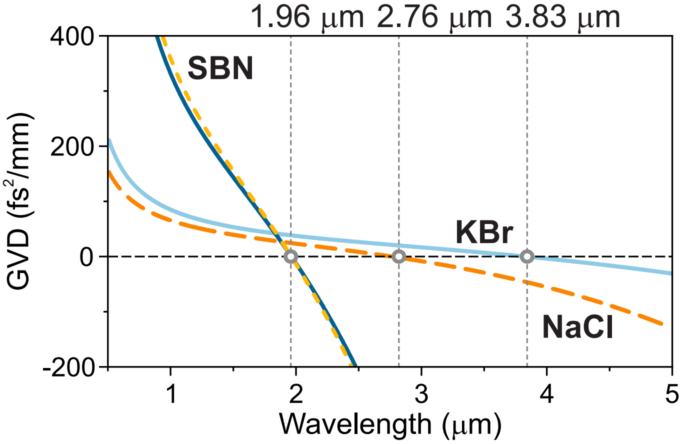

Figure 4: GVD of KBr (solid light blue line), NaCl (long-dashed orange line) [24], SBN for ordinary (short-dashed yellow line) and extraordinary (solid dark blue line) polarization [53]. Grey hollow circles together with dashed grey vertical lines denote zero GVD wavelengths.

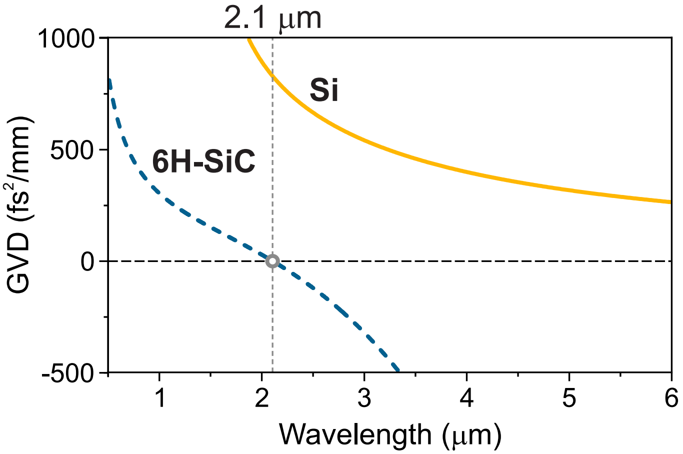

Figure 5: GVD curves of 6H-SiC (dashed dark blue line) [59] and Si (solid yellow line) [58]. Grey hollow circle together with dashed grey vertical line denote zero GVD wavelength.

NONLINEAR REFRACTIVE INDEX EVALUATION

Since there is a lack of knowledge about nonlinear optical properties of KRS-5, KRS-6 (Section 1.1) and 6H-SiC (Section 2.2), we carried out the evaluation of nonlinear refractive index of these materials. The evaluation procedure is based on finding the energy (or power) at which the self-focusing distance (the position of the nonlinear focus) is equal to the length of the nonlinear medium (L) or, in other words, the nonlinear focus is formed at the back face of the medium. This can be achieved by measuring the energy transmission (T) through the sample (the ratio of measured energy after and before the sample) and by calculating the energy transmission derivative with respect to pump pulse energy (E), termed as fractional losses (dT/dE). The basic principle of the evaluation method is explained in Fig. 6 where a simplified view of energy transmission and fractional losses dependence on the input pulse energy is depicted in (a) and (b), respectively. Fig. 6 (c) illustrates how the beam self-focuses when the geometrical focus of the lens is located at the front face of the sample.

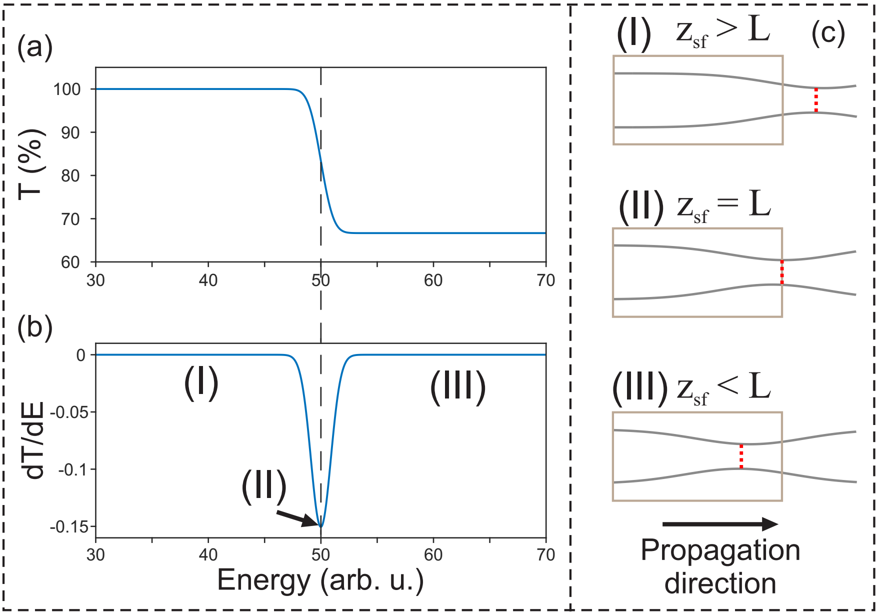

Figure 6: Explanation of nonlinear refractive index evaluation: (a) energy transmission and (b) fractional losses versus the input pulse energy and (c) shows the position of nonlinear focus with increasing the input energy. The brown rectangle represents the sample and the red dashed lines indicate the position of the nonlinear focus.

At first, the input energy is small and the beam can only self-focus after the sample, hence there are no nonlinear losses in the sample. In this case, the output energy changes linearly together with the input energy and the energy transmission is constant. This regime corresponds to sector (I) in Fig. 6 (b) and (c). When increasing the input pulse energy, the nonlinear focus shifts closer to the back face of the sample, hence the intensity at the back of the sample increases and the nonlinear losses due to multiphoton and free-electron plasma absorption come into play. With enough input energy there comes a point when the nonlinear focus is formed exactly at the back face of the sample (sector (II)) which is indicated by the extremum of fractional losses (since the beam diameter at the nonlinear focus is the smallest, the intensity and nonlinear losses are the largest). With further increase of the input pulse energy, the position of nonlinear focus moves towards the front face of the sample and the energy transmission settles down (sector (III)).

Then, we can express the nonlinear refractive index from the formula of critical power for self-focusing (Eq. 3):

$$n_2 = \frac{3.77\lambda^2}{8\pi n_0 P_{cr}}. \tag{10}$$

Since we know the exact self-focusing distance ($z_{sf} = L$) and the corresponding pulse power (P), P_{cr} can be found from the empirical Marburger law, see Eq. 4 and after that the n_2 can be calculated from Eq. 10.

It should be noted that the extremum of fractional losses in Section 1.1 is a minimum and in Section 2.2 it is a maximum due to an added minus sign before dT/dE. However, the sign of fractional losses is not important for our n_2 evaluation, since we need to find only an input pulse energy value corresponding to the extremum, be it maximum or minimum.

Finally, for the sake of justifying the experimentally measured values, the van Stryland analysis was employed for analytical calculation of n_2 [54]. In the case of KRS-5 and KRS-6, an updated dimensionless parameter $K_0 = 7.33 \cdot 10^{-9}$ was used [55].

1. Femtosecond filamentation and supercontinuum generation in narrow band gap dielectric crystals

Motivation

A widely used approach for SC generation in the mid-infrared wavelength range relies on femtosecond filamentation at laser wavelengths falling into the region of anomalous group velocity dispersion of wide-bandgap dielectric crystals and glasses, yielding generation of multioctave SC with continuous spectral coverage from the ultraviolet to the mid-infrared [64–71].

However, the most popular SC hosts such as fused silica, sapphire or YAG are not as easily applicable in the mid-infrared due to their absorption band laying in this spectral region. In addition, an explicit numerical study of SC generation in various nonlinear materials with mid-infrared laser pulses suggested that the zero GVD wavelength may serve as a reasonably good indicator for attainable redshift of the SC spectrum [72]. For what concerns this criterion, the zero GVD points of the above mentioned materials are located in the near infrared, at wavelengths generally shorter than 2 µm. Therefore, materials such as narrow bandgap dielectric crystals [73] whose zero GVD points are located in the mid-infrared (MIR), emerge as potentially efficient nonlinear media for SC generation in this spectral range.

First of all, mixed thallous halides KRS-5 and KRS-6 stand out as promising nonlinear materials for this spectral range. KRS-5 and KRS-6 are well-known infrared window materials [57], which also find applications in the mid-infrared [74] and gamma-ray [75] spectroscopy, and astronomical instrumentation [76, 77]. KRS-5 was recently considered for use in acousto-optics [78, 79]. However, from the perspective of nonlinear optics, KRS-5 and KRS-6 appear exotic, and to the best of our knowledge, these crystals were never considered as nonlinear optical materials. Secondly, recent numerical simulations predicted that filamentation of femtosecond mid-infrared pulses in alkali metal halides, which possess extremely broad mid-infrared transmittance and whose zero GVD points are located deeply in the mid-infrared, are capable of producing multi-octave SC spectra with remarkable red shifts [72]. However, no experimental investigations of the femtosecond filamentation and SC generation in alkali halides NaCl and KBr have been conducted so far. Finally, disordered narrow band gap dielectrics with random quasi phase matching such as strontium barium niobate (SBN), also promise interesting perspectives of mid-infrared SC generation enriched with non-zero second-order nonlinearity enabled broadband frequency generation [80].

This Chapter consists of three sections that are based on the supplied articles A2, A3 and A4, respectively. The first section is dedicated to an experimental study of SC generation in mixed thallous halides: thallium bromoiodide (KRS-5) and thallium chlorobromide (KRS-6) as produced by self-focusing of 60 fs pulses with central wavelengths of 3.1 μm and 3.6 μm, in single and multiple filamentation regimes. The second section reports on SC generation in alkali halide crystals NaCl and KBr using 70 fs 3.6 μm pump pulses, which fall slightly above the zero GVD point of NaCl and slightly below that of KBr. The third and last section is a short study of supercontinuum generation in polycrystalline SBN with femtosecond near- and mid-infrared laser pulses with carrier wavelengths falling into the range of normal, zero and anomalous GVD of the crystal.

1.1. Supercontinuum generation in mixed thallous halides KRS-5 and KRS-6

This section is dedicated to the experimental study of SC generation in mixed thallous halides in the mid-infrared. Mixed thallous halides KRS-5 and KRS-6 are dielectric crystals of cubic symmetry, which possess relatively small energy band gaps and very broad infrared transparency, which extends into far infrared, see the parameters in Table 1 of *Experimental Methods* chapter. These materials also exhibit a certain transparency in the visible spectral range: Fig. 1.1 shows the measured transmittance in the visible and near-infrared spectral ranges of 2 mm thick KRS-5 and KRS-6 samples, indicating the short wave cut-off wavelengths of 550 nm and 400 nm for KRS-5 and KRS-6, respectively.

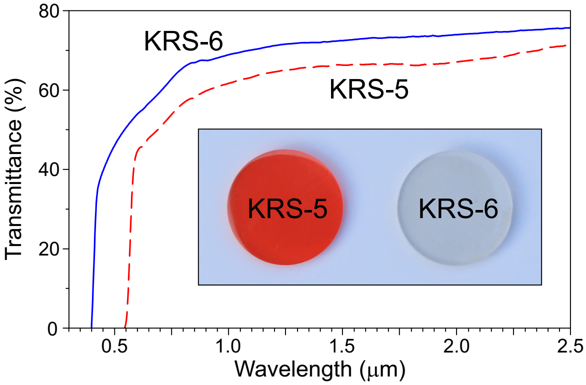

Figure 1.1: Measured transmittance of 2 mm thick KRS-5 and KRS-6 samples in the visible and near-infrared spectral ranges. The inset shows a photo of the used samples.

For a summary of the experimental setup and measurement equipment used the reader is referred to the *Experimental Methods* chapter. The chosen input wavelengths of 3.1 μm and 3.6 μm fall into the range of normal group velocity dispersion of KRS-5, which has a zero GVD wavelength at 6.6 μm, as calculated from the dispersion equation provided in Ref. [57]. It is expected that the input wavelengths fall into the range of normal GVD of KRS-6 as well, however, the exact value of its zero GVD point is not known with a reasonable precision, for more information please see the *Experimental Methods* chapter. The measurements of nonlinear transmission, which were used for evaluation of the nonlinear refractive indexes, were performed by focusing the input beam with BaF_2 lens ($f = 50$ mm) onto the input face of 2 mm-thick samples of KRS-5 and KRS-6. In the SC generation experiments, looser focusing of the input beam (BaF_2 lens, $f = 100$ mm) and longer samples of KRS-5 and KRS-6 (both of 6 mm thickness) were used.

Since the nonlinear optical properties of KRS-5 and KRS-6 are basically unknown, first we carried out an experiment in order to evaluate the nonlinear refractive indexes of these materials. The evaluation procedure is based on measuring the energy transmission through the samples and is described in-depth in the *Nonlinear Refractive Index Evaluation* section of the *Experimental Methods* chapter. We measured the energy transmission of 2 mm-thick KRS-5 and KRS-6 samples at 3.1 μm versus the input pulse energy, as illustrated in Fig. 1.2 (a). Taking into account the incident photon energy of 0.4 eV and the band gap values listed in Table 1, the measured nonlinear losses are associated with 7 and 9 photon absorption in KRS-5 and KRS-6, respectively, and to some extent with the absorption of free electron plasma via inverse Bremsstrahlung effect [5].

The determined n_2 values ($(105 \pm 19) \times 10^{-16}$ cm^2/W for KRS-5 and $(54 \pm 10) \times 10^{-16}$ cm^2/W for KRS-6) are fairly close to those calculated analytically ($n_2 = 98\times10^{-16}$ cm^2/W for KRS-5 and $n_2 = 39\times10^{-16}$cm^2/W for KRS-6) using the formalism described in Ref. [54]. In the case of KRS-6 the discrepancy between the evaluated and theoretically calculated values could be attributed to the lack of accurate Sellmeier equation in this spectral range. In order to further experimentally justify the validity of our approach for estimation of n_2, we measured the nonlinear transmission of 3 mm-thick YAG sample, whose nonlinear refractive index is known rather precisely: the value of $n_2 = 6.2\times10^{-16}$ cm^2/W has been reported for the input wavelength of 1.06 μm [81]. The results for nonlinear transmission and fractional losses in YAG are added to Fig. 1.2 for a comparison. Note a significantly increased input pulse energy required to produce the nonlinear focus at the output face of 3 mm thick YAG sample. Also notice generally smaller fraction of the absorbed energy, which is formally due to 17-photon absorption, taking into account the band gap of YAG of 6.5 eV. Our evaluation procedure yields n_2 value of $(6.0\pm0.6)\times10^{-16}$ cm^2/W, which almost perfectly coincides with that specified in literature, also bearing in mind the general dispersion law of n_2, which suggests a slight decrease of nonlinear refractive index values with longer wavelengths.

The estimated large values of n_2 in KRS-5 and KRS-6 suggest remarkably

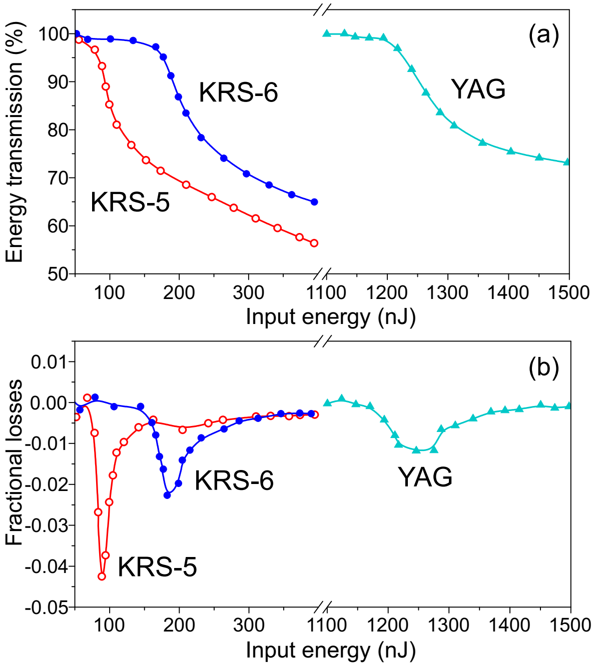

Figure 1.2: (a) Normalized energy transmission of 2 mm-thick KRS-5 and KRS-6 samples and 3 mm-thick YAG sample versus the energy of 60 fs, 3.1 μm input pulses. (b) Fractional losses, whose minima indicate that the position of the nonlinear focus is located at the output face of the sample.

low critical power for self-focusing in these materials: 0.58 MW in KRS-5 and 1.22 MW in KRS-6, respectively, with input pulses of 3.1 μm. In comparison, critical power for self-focusing in YAG at this wavelength is more than by an order of magnitude higher (13.1 MW). Indeed, the threshold energies for filamentation and supercontinuum generation in 6 mm-thick KRS-5 and KRS-6 samples were found to be just few hundreds of nanojoules. Fig. 1.3(a)-(d) show the SC spectra in KRS-5 recorded with different input pulse energies, resulting in single and multiple filamentation regimes, as verified by the near-field intensity distributions of the output beams that are shown in the insets. SC spectrum in KRS-5 produced by the 3.1 μm, 260 nJ input pulses, provides a continuous wavelength coverage from 1.57 to 5.0 μm (at the 5×10^{-4} intensity level) and exhibits a prominent double dip around 4.25 μm that is attributed to absorption of atmospheric CO_2, as illustrated in Fig. 1.3(a). The inset shows the intensity distribution measured at the output face of the sample, indicating a single filament with FWHM diameter of 27 μm, surrounded by a characteristic ring-shaped periphery. As the input pulse energy is increased to 390 nJ, the SC spectrum shows a stable short-wave cutoff at 1.57 μm due to the intensity clamping effect and exhibits a slight broadening to 5.3 μm on the long-wavelength side, while maintaining a single filament, as illustrated in Fig. 1.3(b). The SC spectra in the single filament regime demonstrate smooth spectral features, and yield reasonably high spectral energy density: 2-30 pJ/nm in the 1.7-2.5 μm range, 50-100 pJ/nm in the 3.5-4.2 μm range and >200 pJ/nm around the pump wavelength.

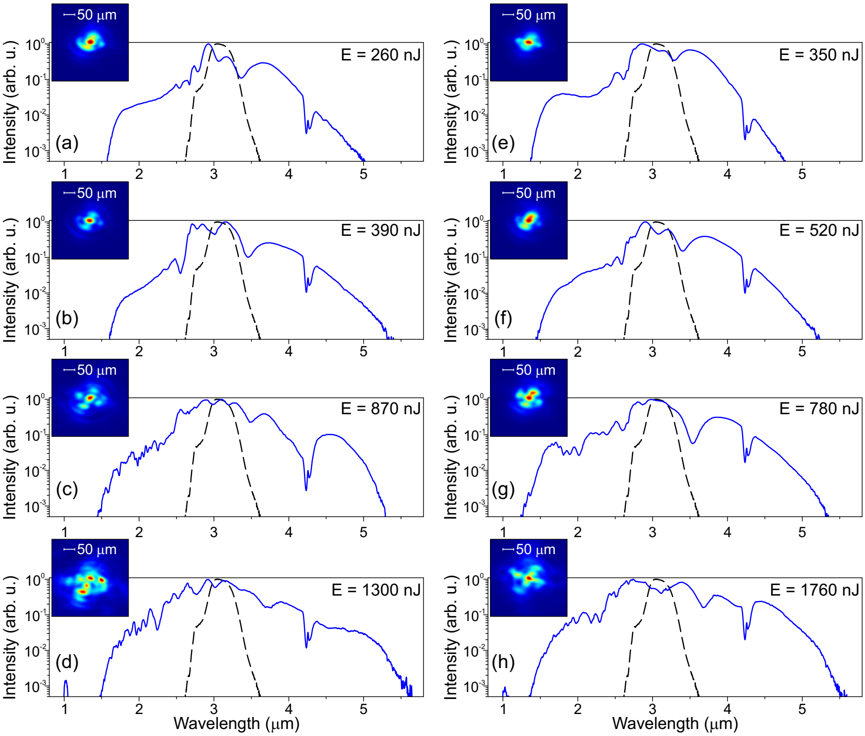

Figure 1.3: Supercontinuum spectra in 6 mm thick KRS-5 (left panel) and KRS-6 (right panel) samples as functions on the energy of 60 fs, 3.1 μm pump pulses. The input pulse energies are indicated in the plots and the input pulse spectra are depicted by dashed curves. Insets show filamentation profiles as measured at the output face of the sample.

A further increase of the input pulse energy leads to multiple filamentation. With the input pulse energy of 870 nJ, multiple filaments emerge in the form of a symmetric and well-reproducible pattern, as illustrated in the inset of Fig. 1.3(c). The occurrence of such multi-filamentation pattern is attributed to small ellipticity of the input beam [82]. The secondary filaments evolve as a result of nucleation of annular rings surrounding the central filament and reside along the major and minor axes of an ellipse. Even higher input pulse energy (1.3 μJ) leads to random distribution of the individual filaments, as shown in the inset of Fig. 1.3(d). The regime of multiple filamentation produces slightly broader SC spectra spanning wavelengths from 1.5 to 5.6 μm. However, in this case, the SC spectra exhibit a significant intensity modulation, which is especially well-pronounced on the short-wave side. Spectral modulation originates from the filament refocusing [83] and in part due to beating between the SC spectra produced by individual filaments. Interestingly, with the input pulse energy of 1.3 μJ we also capture a detached narrow spectral peak centered at 1.03 μm, which is attributed to the third harmonic of the pump. A very similar trend of the spectral broadening and transition from the single to multiple filamentation regimes versus the input pulse energy was recorded in KRS-6, as shown Fig. 1.3(e)-(h). Due to lower values of n_2, the SC spectra in KRS-6 were generated with slightly higher input pulse energies. On the other hand, due to larger bandgap of KRS-6, the measured SC spectra exhibit slightly shorter cut-off wavelengths (1.37 μm) at the short-wavelength side, while the spectral broadening toward long-wavelength side remained essentially identical.

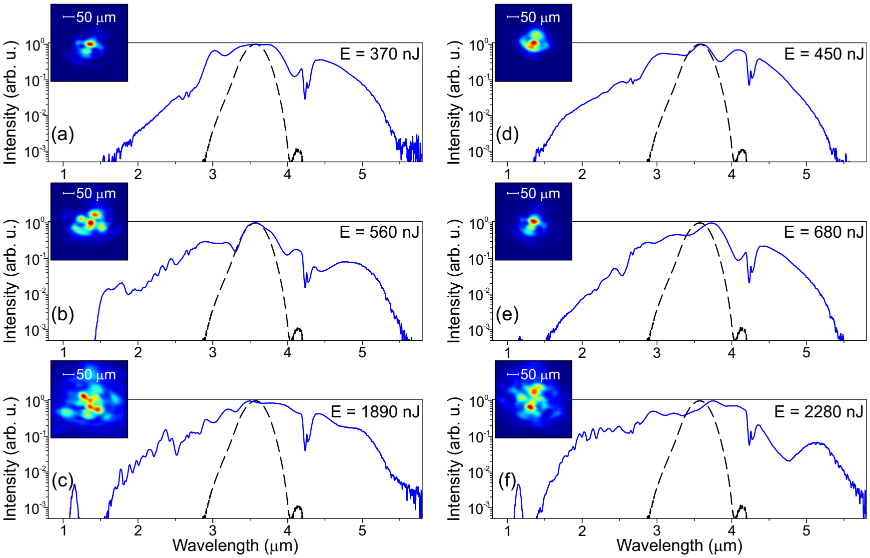

Figure 1.4: Supercontinuum spectra in 6 mm thick KRS-5 (left panel) and KRS-6 (right panel) samples as functions on the energy of 60 fs, 3.6 μm pump pulses. The input pulse energies are indicated in the plots and the input pulse spectra are depicted by dashed curves. Insets show filamentation profiles as measured at the output face of the sample.

The experiments performed with the longer wavelength (3.6 μm) input pulses revealed very similar dynamics of the spectral broadening and filamentation versus the input pulse energy in both materials, as illustrated in Fig. 1.4. However, in the present case, in both samples a slightly larger spectral broadening on the long-wavelength side of the SC was recorded: up to 5.5 μm and slightly beyond 5.8 μm (which is the limit of our spectrometer detection range) in the regimes of single and multiple filamentation, respectively. Notice that in addition to prominent CO_2 absorption, a more shallow but clearly distinguishable dips around 2.7 μm as due to absorption of water vapor emerge in the SC spectra. Also note more intense third harmonic peaks at 1.2 μm in KRS-5 and KRS-6, which emerge in the multiple filamentation regime.

Finally, in order to test the suitability of KRS-5 and KRS-6 for SC generation under real experimental settings, we examined the long-term reproducibility of the SC spectra in these materials, which is important for the major part of practical applications. Fig. 1.5 compares the reference SC spectra with the spectra recorded after 1 and 2 hours of operation at 1 kHz repetition rate in KRS-5 and KRS-6 samples. The SC spectrum in KRS-5 shows an excellent long-term reproducibility: no apparent changes in either SC spectral shape or spectral intensity were detected over 2 hours of operation, as shown in Fig. 1.5(a).

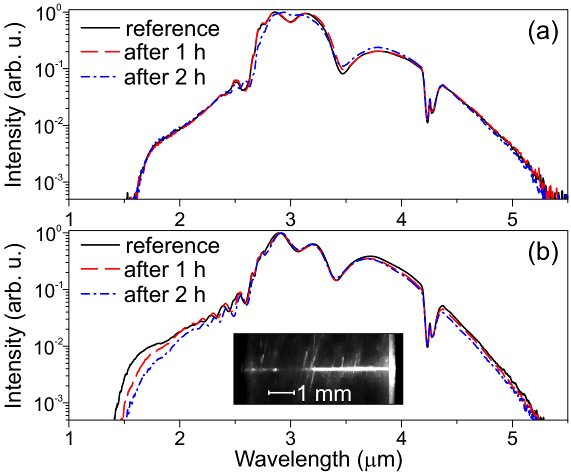

Figure 1.5: Long-term reproducibility of SC spectra in (a) KRS-5 and (b) KRS-6. The input pulse wavelength is 3.1 μm, the input pulse energies are 350 nJ and 500 nJ, respectively. Inset shows the side view of KRS-6 sample, as illuminated by He-Ne laser beam.

In contrast, the SC spectrum in KRS-6 exhibits a slight but noticeable shrinking on the short-wavelength side, which progresses with the exposure time, whereas the part of the SC spectrum on the long-wavelength side remains constant, as shown in Fig. 1.5(b). The observed spectral changes in KRS-6 could be attributed to filament-induced material modification under multiple laser pulse exposure. The material modification was visualized by launching a He-Ne laser beam along the path of the filament, showing a clearly detectable scattering from the modified volume, as depicted in the inset of Fig. 1.5(b). On the other hand, the time scale of the spectral changes suggests that degradation of KRS-6, whatever is its origin, is relatively slow, so these detrimental effects could be easily avoided by the translation of the sample.

1.2. The influence of color centers on supercontinuum generation in NaCl and KBr

In this section an investigation of supercontinuum generation with femtosecond mid-infrared laser pulses in NaCl and KBr crystals pumped at the vicinity of their zero GVD points is presented. The experimental setup along with measurement equipment and methods can be found in the *Experimental Methods* chapter. The nonlinear media used were uncoated NaCl and KBr samples of 5 mm thickness. NaCl and KBr are crystals with cubic symmetry and exhibit remarkable transparency ranges from the UV to the far-infrared and relatively large nonlinear indexes of refraction. The chosen pump wavelength of 3.6 µm falls close to their zero GVD points: in NaCl, GVD is weakly anomalous, while in KBr, GVD is weakly normal. The relevant optical parameters of these materials are presented in Table 1 of *Experimental Methods* chapter.

It is a well known fact that most of alkali metal halide crystals are prone to formation of color centers that affect the SC spectrum to a certain degree, as experimentally demonstrated in LiF [26, 84–87] and to some extent, in PbF_2 [73]. The color centers are associated with electron trapping at a halide vacancy (F centers) and two F centers on adjacent sites (M centers, or the so-called F_2 centers) [88]. Color centers are responsible for the occurrence of broad absorption bands, whose peak wavelengths are located in the visible (F centers) and near infrared (M centers). More specifically, broad absorption bands in NaCl are centered at 460 nm (F centers) and at 725 nm (M centers) [89], while in KBr the respective absorption bands associated with F and M centers are more redshifted and peak at 625 nm and 930 nm, respectively [90]. In addition to these, ultraviolet absorption bands are observed as well, that are due to V centers associated mostly with hole traps by impurities in these materials. The process of color center formation in NaCl and KBr crystals is very fast, taking place on a microsecond time scale, as demonstrated by pump-probe measurements in intense femtosecond UV irradiation conditions [89, 90]. Rapid accumulation of color centers was justified by a drop of transmission at selected probe wavelengths, that eventually saturates after a few seconds at 1 kHz repetition rate [88].

Fig. 1.6 shows the evolution of SC spectrum in NaCl (a) and KBr (b) as a function of exposure time. First of all, in order to avoid the influence of color center formation on SC generation, the samples were continuously translated perpendicular to the pump beam direction during the measurement. Ultrabroadband, multi-octave SC spectra were recorded in both NaCl and KBr samples, pumped by 70 fs, 3.6 µm pulses with energies of 3.56 and 2.23 µJ, respectively, after accounting for Fresnel reflections from the input face of the samples. The input pulse energies correspond to the input powers of 51 MW and 32 MW, which equals to 1.7 P_{cr} and 2.0 P_{cr} in NaCl and KBr, respectively.

More specifically, the measured SC spectrum in NaCl covered the wavelength range from 700 nm to 5.4 µm (at the 10^{-4} intensity level) that corresponds to 2.9 optical octaves. A slightly narrower SC spectrum, in the 0.85–5.4 µm range, corresponding to 2.7 optical octaves was measured in KBr. Note the distinct spectral dips around 2.7 and 4.25 µm that are absorption signatures of atmospheric H_2O and CO_2, respectively. These spectra further serve as references for monitoring spectral modifications due to evolving color centers in these materials when SC is generated in a static setup.

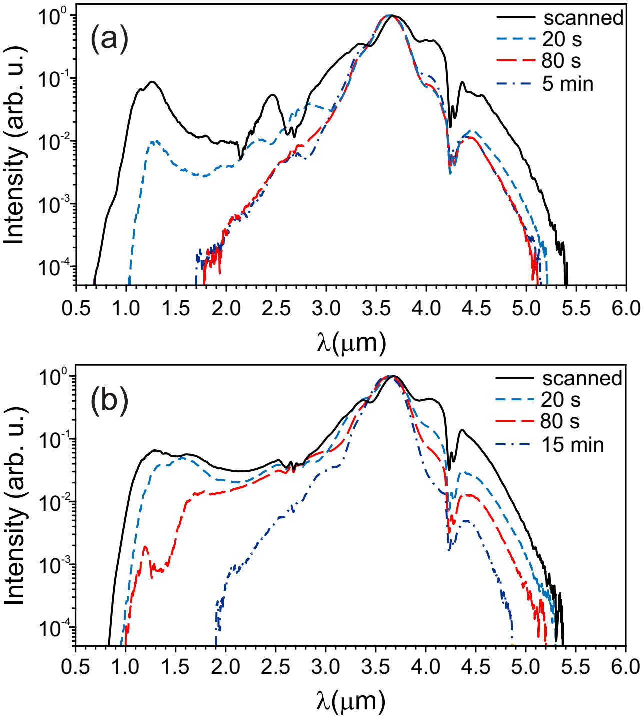

Figure 1.6: Evolutions of SC spectra in (a) NaCl and (b) KBr as functions of exposure time as pumped by 3.6 μm, 70 fs pulses.

Furthermore, in a static setup due to color center formation, the SC spectrum experiences a considerable shrinking along with a decrease of the spectral intensity on both sides of the carrier wavelength, and spectral shrinking is particularly pronounced at the short-wavelength side. Note that dramatic spectral changes emerge very quickly (within a few tens of seconds at 500 Hz repetition rate). Thereafter color center-induced spectral dynamics settle down after 80 s of exposure in NaCl, and the SC spectrum keeps its new shape with a markedly reduced width (1.8–5.1 µm, as defined at the 10^{-4} intensity level) for the rest of the measurement time. A similar color center-induced narrowing of the SC spectrum was observed in KBr, as illustrated in Fig. 1.6 (b). However, in the present case, the spectral dynamics are markedly slower: the shrinking of the SC spectrum finally settles only after 15 min of exposure time.

Changes of the SC spectra correlate very well with the decrease of energy transmittance, recorded for both material samples and shown in Fig. 1.7. Here the energy transmittance is normalized to the transmittance levels measured in the absence of color centers, i.e. by continuously translating the samples. In other words, the unity transmittance was set with an account for Fresnel reflection from the output face of the sample and energy losses that occur in the filamentation process that are contributed by multiphoton absorption and absorption of free electron plasma via inverse Bremsstrahlung effect. Therefore the illustrated energy losses are contributed solely by linear and nonlinear absorption of the color centers.

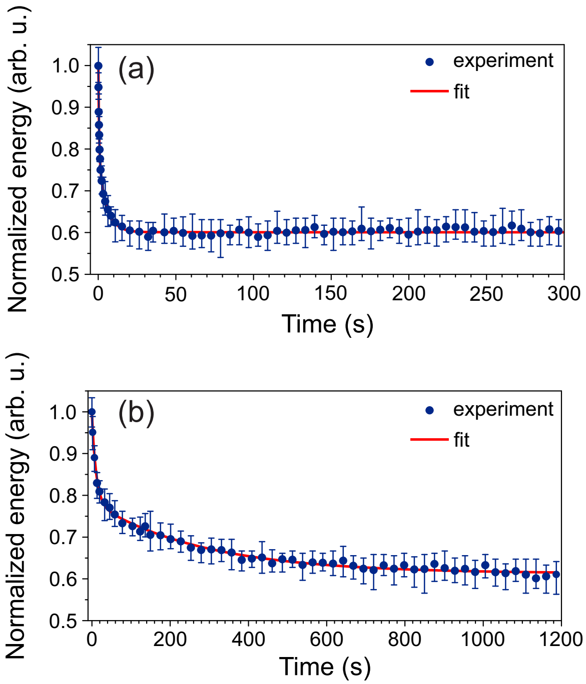

Figure 1.7: Measured energy transmittance of (a) NaCl and (b) KBr samples, pumped by 3.6 μm, 70 fs pulses, together with two-exponential fits (solid curves) in a static setup. The plots are normalized to the transmittance of the samples in the abscence of color centers. Each data point represents an average over 25 laser shots (the time interval of 50 ms) and for better data readability, only every third data point is displayed.

Notice that the energy transmittance decreases very rapidly and color centers take an immediate effect on the SC spectral width. NaCl shows a prompt drop of energy transmittance that is well fitted by two exponents with time constants of 0.53 s and 5.1 s, as shown in Fig. 1.7(a). The energy transmittance after 20 s settles down to 60% of the initial transmittance value, which thereafter remains constant for the rest of the measurement. The energy transmittance of KBr sample settles to an almost identical final value, however, the process is more extended in time (two-exponential decay with time constants of 10.6 s and 282 s), see Fig. 1.7 (b). An established two-exponential decay in both materials could be attributed to different speeds of formation of F (a faster exponent) and M (a slower exponent) centers.

Finally, residual color centers are easily seen by the naked eye, as illustrated in Fig. 1.8. Their specific colors: dark green in NaCl and blue in KBr, are due to F center absorption bands in the visible range. Note that color centers are formed only at the filament site, i.e., where intensity and nonlinear losses due to multiphoton and free electron absorption are the highest, enabling to trace precisely the filament path. The SC spectra in NaCl were simulated numerically using a model which solves a unidirectional nonparaxial propagation equation for the pulse envelope, see [4, 91] for details, taking relevant material parameters from Table 1 of the *Experimental Methods* chapter and input pulse parameters from the experiment. The effect of color centers was accounted for by using a phenomenological approach, which considers them as evenly distributed impurities with an energy bandgap of 2.7 eV that corresponds to the strongest absorption band centered at 460 nm due to F centers [89].

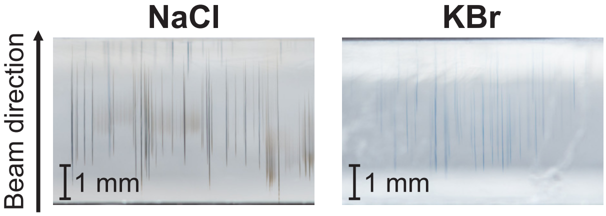

Figure 1.8: Photographs of (a) NaCl and (b) KBr samples with filament-induced color centers, which were produced by slightly varying the input pulse energies (around the specified values for NaCl and KBr) and exposure times (from a few tens of seconds to a few tens of minutes).

The numerically simulated SC spectra using different impurity densities, which could be directly associated with accumulation of color centers while increasing exposure time in the experiment, are presented in Fig. 1.9. The numerical results demonstrate a marked narrowing of SC spectrum as the density of the impurities increases. Of course, inclusion of color centers in the numerical model in that way, is a very simple approximation, since color center-induced modifications of relevant material properties, e.g., linear and nonlinear refractive indexes and dispersion were not considered. Nevertheless, even this simple numerical approach gives a fair agreement with experimentally recorded spectral dynamics. Therefore the following qualitative mechanism of how color centers act on the width of SC spectrum could be unveiled. Since the absorption band of color centers (F-centers, in the present case) does not overlap with SC spectrum, they do not absorb the SC radiation directly. This suggests that color centers absorb the input pulse energy via multiphoton absorption. The observed shrinking of SC spectrum is then explained by reduction of the effective material band gap through formation of color center absorption band, which results in a decrease of clamping intensity and thus an increase of the limiting filament diameter, which in turn yields a narrower SC spectrum [7]. Multiphoton absorption of color centers readily produces a larger number of free electrons, which are then accelerated via inverse Bremsstrahlung and avalanche, and thus participate in further production of color centers. This lasts until the process reaches a certain equilibrium between the production and annihilation of color centers.

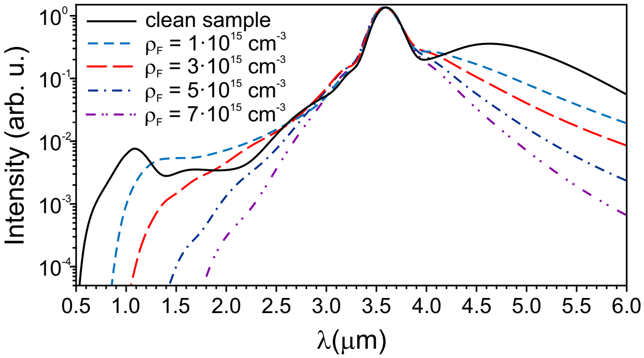

Figure 1.9: Numerically simulated SC spectra in NaCl with different impurity densities ρ_F that mimic the effect of color center absorption.

1.3. Supercontinuum generation in SBN crystal

This section is devoted to a short study of supercontinuum generation in strontium barium niobate (SBN) crystal of 5 mm thickness with 1.2, 2.0 and 2.4 μm femtosecond pump pulses and is based on a part of Article 4 publication. SBN is a ferroelectric negative uniaxial crystal with an energy bandgap of 3.4 eV and transparency in the 0.4-5.5 μm wavelength range. Also, as stated in the Table 1 of *Experimental Methods* chapter, the zero group velocity dispersion wavelength of this material is at 1.96 μm. Structurally SBN is a polydomain crystal and consists of birefringent needle-like randomly distributed ferroelectric domains whose widths vary between a few nanometers and a few micrometers and whose lengths are of a few hundreds of micrometers [92]. Therefore, due to relaxed phase matching conditions, SBN is an interesting nonlinear material that can be used for various nonlinear optical processes at multiple wavelengths, including second- and third-harmonic generation without the need of angle or temperature tuning [93].

Large SBN n_2 (52.4×10^{-16} $\mathrm{cm^2/W}$ at 1064 nm [54]), implies very low critical power for self-focusing. Indeed, the onset of filamentation was experimentally detected with pump pulse energies less than 100 nJ and sub-MW peak powers: 32 nJ (0.35 MW) at 1.2 μm, 54 nJ (0.53 MW) at 2.0 μm, and 74 nJ (0.56 MW) at 2.4 μm, as verified by the onset of spectral broadening and beam filamentation. Figure 1.10 compares the SC spectra in polydomain SBN generated in the ranges of its normal (1.2 μm), zero (2.0 μm), and anomalous GVD (2.4 μm). The pump pulse energies were set slightly above the threshold energies for filamentation, where blueshifted broadening of the spectra saturates and no refocusing of the filament is observed. Smooth, more than an octave-spanning SC spectra in the wavelength ranges of 0.8-1.81 μm, 1.04-2.5 μm, and 1.0-3.32 μm (defined at the 10^{-4} intensity level) were obtained using pump pulses of 1.2 μm, 2.0 μm, and 2.4 μm, respectively. Fig. 1.11 shows the dependence of SC blue-shift and material GVD on the pump wavelength. Longer pump wavelength constitutes a higher order of multiphoton absorption, lower material GVD and at the same time a larger SC blue-shift.

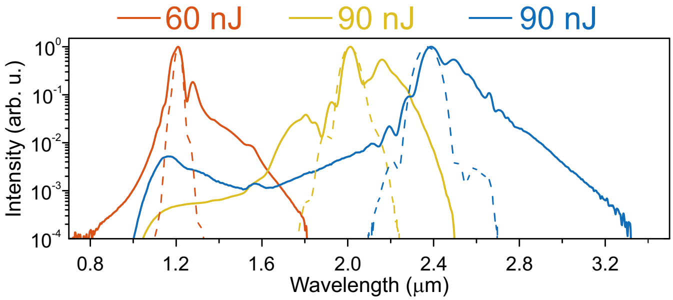

Figure 1.10: SC spectra generated in SBN using pump pulses of 1.2 μm (red curve), 2.0 μm (yellow curve) and 2.4 μm (blue curve). The energies of the pump pulses are indicated at the top. The input spectra are depicted by dashed curves.

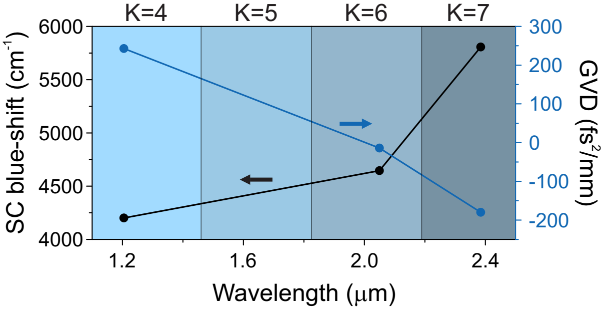

Figure 1.11: SC blue-shift and material GVD versus the wavelength of the incident pulses in SBN. Coloured sections and text above the graphs represent the order of multiphoton absorption.

Figure 1.12 shows filamentation and SC generation dynamics as a function of the input pulse energy in the cases of normal, zero, and anomalous GVD. The energy ranges for each input wavelength were chosen to preserve a single filament propagation regime and to avoid the occurrence of multiple filamentation. With the increase of pump energy, the filament undergoes refocusing which is indicated by a secondary boost of spectral broadening and the occurrence of interference pattern in the SC spectrum, very clearly visible with 1.2 μm and somewhat less pronounced with 2.0 μm and 2.4 μm pump pulses.

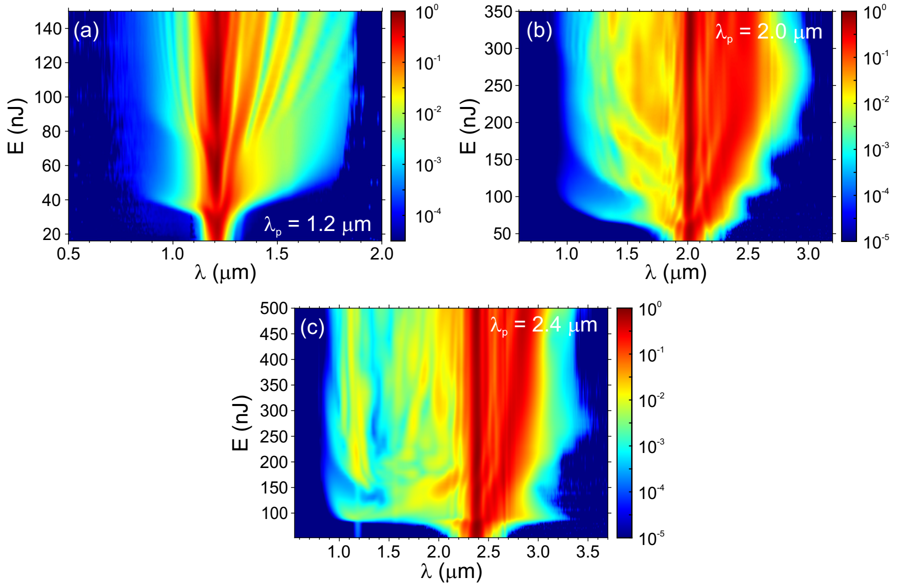

Figure 1.12: Spectral broadening dynamics as functions of the pump pulse energy in the cases of normal (1.2 μm), zero (2.0 μm) and anomalous (2.4 μm) GVD.

To summarize the observed spectral dynamics presented in Fig. 1.12, the spectral broadening versus the input pulse energy shows several interesting features, which are quite general from the point of view of underlying physics. First, an apparent shrinking of the SC spectra (especially well-pronounced on the short-wavelength side) is observed before the filament refocusing takes place in all investigated cases. This spectral shrinking is attributed to the defocusing and absorption of free electron plasma that push a large portion of the pulse energy out of the propagation axis after the first nonlinear focus (see [94] for details). Second, each refocusing cycle in the cases of zero (2.0 μm) and anomalous (2.4 μm) GVD is followed by the change of redshift. Such spectral behavior was also observed in various nonlinear media (CaF_2, LiF single crystals and fused silica; see Ref. [69]), and was attributed to the periodic breathing of the light bullet, i.e., the self-compressed pulse that emerges due to the interplay between self-phase modulation and anomalous GVD. The same consideration applies also to the case of zero GVD, where the pulse splitting takes place, and the spectrum of the trailing subpulse that is responsible for the redshift, falls into the range of anomalous GVD of the crystal.

Summary of the results

First of all, in this chapter we evaluated the nonlinear indexes of refraction of mixed thallous halides: thallium bromoiodide (KRS-5) and thallium chlorobromide (KRS-6) and demonstrated efficient SC generation in the mid-infrared spectral range by filamentation of 60 fs pulses with carrier wavelengths of 3.1 and 3.6 μm. Almost 2 octave spanning SC spectra, in the range of 1.5 to 5.5 μm (defined at the 5×10^{-4} intensity level), were produced in 6 mm-thick samples of KRS-5 and KRS-6, see Fig.1.13 for the summary of SC spectra obtained in the investigated materials in this Chapter. We demonstrated that filamentation and SC generation is achieved with remarkably low input pulse energies (few hundreds of nanojoules) owing to large values of n_2: $(105\pm19)\times10^{-16}$ cm^2/W for KRS-5 and $(54\pm10)\times10^{-16}$ cm^2/W for KRS-6, as evaluated from the measurements of the nonlinear energy transmission. Long-term spectral measurements revealed an excellent reproducibility of the SC spectrum in KRS-5, while the SC spectrum in KRS-6 showed a slight shrinking at the short-wavelength side due to filament-induced modification of the material, which takes place on the time scale of an hour and therefore could be easily avoided by the translation of the sample.

Secondly, we experimentally studied SC generation in alkali halide crystals NaCl and KBr pumped by femtosecond 3.6 μm, 60 fs laser pulses, in the absence and in the presence of color centers. Almost three octave spanning SC spectra were recorded in these materials in the absence of color centers (Fig.1.13), as the samples were continuously translated during the measurement. In contrast, in the static setup, color centers in both materials are produced in the matter of seconds, resulting in a considerable reduction of the SC spectral widths and energy transmittance. The narrowing of SC spectrum in NaCl was simulated numerically using a simple phenomenological model which considered color centers as impurities with an energy bandgap of 2.7 eV that corresponds to the F-center absorption band centered at 460 nm.

Finally, we have also demonstrated that polydomain SBN serves as a suitable nonlinear medium for SC generation in the infrared spectral range. More than an octave-spanning infrared SC spectra were produced with reasonably low pump energies (powers), in the ranges of normal (1.2 μm), zero (2.0 μm), and anomalous (2.4 μm) GVD of the crystal.

Therefore, the results suggest that narrow band gap dielectrics such as KRS-5, KRS-6 and SBN can serve as efficient nonlinear media for femtosec-

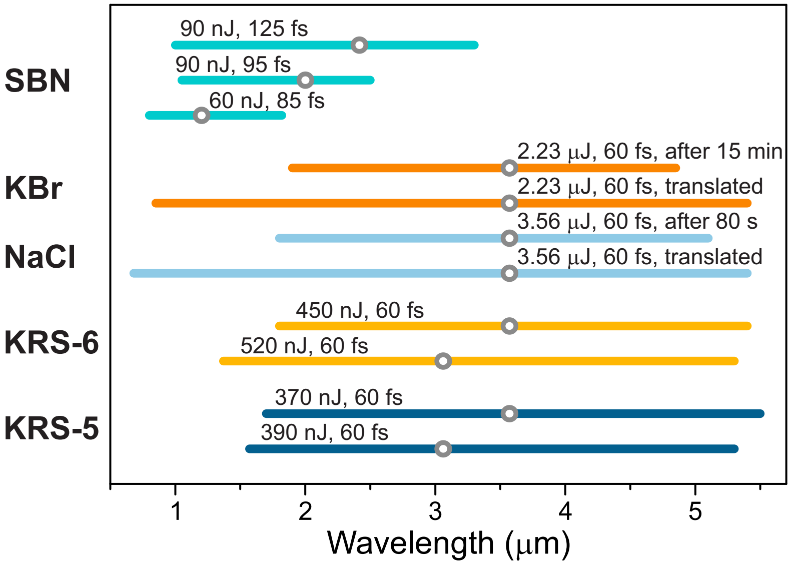

Figure 1.13: Summary of the supercontinuum spectra generated in single filament regime in the investigated dielectric materials: KRS-5, KRS-6, NaCl, KBr and SBN. Grey dots pinpoint the wavelength and the comments indicate the energy and duration of the pump pulses. Spectral width in the case KRS-5 and KRS-6 was defined at $5{\times}10^{-4}$ intensity level while all the other spectral widths were defined at 10^{-4} intensity level.

ond supercontinuum generation in the near- and mid-infrared spectral range. Alkali metal halide crystals, such as NaCl and KBr also have potential for ultrabroadband SC generation in this spectral region, although the samples should be translated in order to avoid the undesirable effects of color center formation.

2. Supercontinuum generation in semiconductor crystals

Motivation

Bulk semiconductor crystals emerge as very attractive nonlinear media for supercontinuum generation in the mid-infrared. As compared to solid-state dielectrics, semiconductors possess smaller bandgaps, but at the same time much larger cubic nonlinearities (see Table 2.1), considerable free-carrier absorption, etc., which eventually may suggest a different balance between the relevant governing effects for filamentation and spectral broadening. The feasibility of semiconductor materials to produce an appreciable spectral broadening and SC generation in the mid-infrared was experimentally demonstrated with picosecond laser pulses more than 30 years ago [95]. Since optical parametric amplification and frequency downconversion techniques have made femtosecond and even few optical cycle pulses in the mid-infrared routinely available, semiconductor crystals are currently receiving attention as interesting nonlinear materials for hosting filamentation phenomena. To date, femtosecond filamentation, spectral broadening, and eventually SC generation was studied in GaAs [32–34, 96], ZnS [35, 67], and ZnSe [35, 37, 97–99], unveiling filamentation scenarios that lead to pulse compression and multioctave SC generation, which provides a broad coverage of mid-infrared wavelengths. On the other hand, a number of widely-available bulk semiconductor crystals with attractive characteristics for SC generation in the infrared have not been thoroughly investigated.

Table 2.1: Main parameters of 6H-SiC and silicon: E_g is the energy bandgap, T is the transmission range, n_0 and n_2 are linear and nonlinear refractive indexes, respectively, λ_0 is the zero GVD wavelength, DT is the optical damage threshold for femtosecond pulses. The bandgap and transmission parameters together with damage thresholds for Si were taken from [24]. Linear refractive index values are given for 2 μm. 6H-SiC nonlinear refractive index value was estimated using the van Stryland analysis at 2 μm [54]. The references to other parameter values are given in the table.

Material	E_g (eV)	T (μm)	n_0	λ_0 (μm)	n_2 ($\times 10^{-16}$ cm^2/W)	DT (J/cm^2)
6H-SiC	2.6	0.5-4	2.5537(o); 2.5873(e) [59]	2.1	89	0.60 [100]
Si	1.12	1.1-6.5	3.4401 [58]	>23	270 [60]	0.55

Firstly, owing to cubic crystal symmetry and very large nonlinearity [60, 101], silicon is identified as one of the most important semiconductor materials in the rapidly emerging field of nonlinear photonics for applications in the mid-infrared spectral region [58, 102, 103]. More than octave-spanning femtosecond SC generation was reported in various geometries and modifications of highly nonlinear dispersion-engineered silicon waveguides, see, e.g., [104–106], and soliton compression was observed in silicon photonic crystals [107]. However, the investigations of nonlinear propagation of femtosecond laser pulses in bulk silicon have been limited to the studies of plasma generation, free-carrier dynamics, energy deposition, and material modification effects with near-infrared wavelengths, mostly in the regime of two-photon absorption [108–112].

Silicon carbide (SiC) is another semiconductor material with high potential for hosting nonlinear interactions in this spectral region. In nonlinear photonics, SiC, as compared to silicon, has a considerable advantage due to its more than twice larger bandgap and hence the reduced nonlinear absorption in the near and mid-infrared spectral range. SiC can be grown in over 200 polytypes with different optical parameters and crystalline structures. However, the three commonly used and widely available polytypes are 3C-, 4H-, and 6H-SiC, with the former one being cubic, and the latter two hexagonal, uniaxial crystals. More importantly, 4H-SiC and 6H-SiC possess relatively large second-order nonlinearities [113]. More recently, dispersion of third-order nonlinearities has been calculated for the three SiC polytypes unveiling a large nonlinear refractive index, comparable to that of silicon: the obtained values were within the range from 0.5 to 6.3 $\times 10^{-14}$ cm^2/W in the 0.5-5 μm spectral region [114]. Experiments exploiting large second and third order nonlinearities of SiC demonstrated spectral broadening [61] and optical parametric oscillation [115] in waveguide and microresonator geometries, respectively, and broadband difference frequency generation [59] and optical parametric amplification [116] in bulk.

This Chapter consists of two sections that are based on the supplied articles A5 and A6, respectively. The first section reports on filamentation and SC generation in a bulk undoped silicon sample with femtosecond laser pulses of four different wavelengths: 3.25, 3.6, 4.0, and 4.7 μm. The second section describes SC generation in 6H-SiC sample using femtosecond laser pulses of various wavelengths in the near- and mid-infrared (1.3-2.4 μm).

2.1. Femtosecond filamentation and supercontinuum generation in bulk silicon

This section covers the investigation of filamentation and SC generation in a bulk undoped silicon sample with femtosecond mid-infrared laser pulses. The experimental setup and measurement methods employed in this work together with the main silicon parameters are described in the *Experimental Methods* chapter.

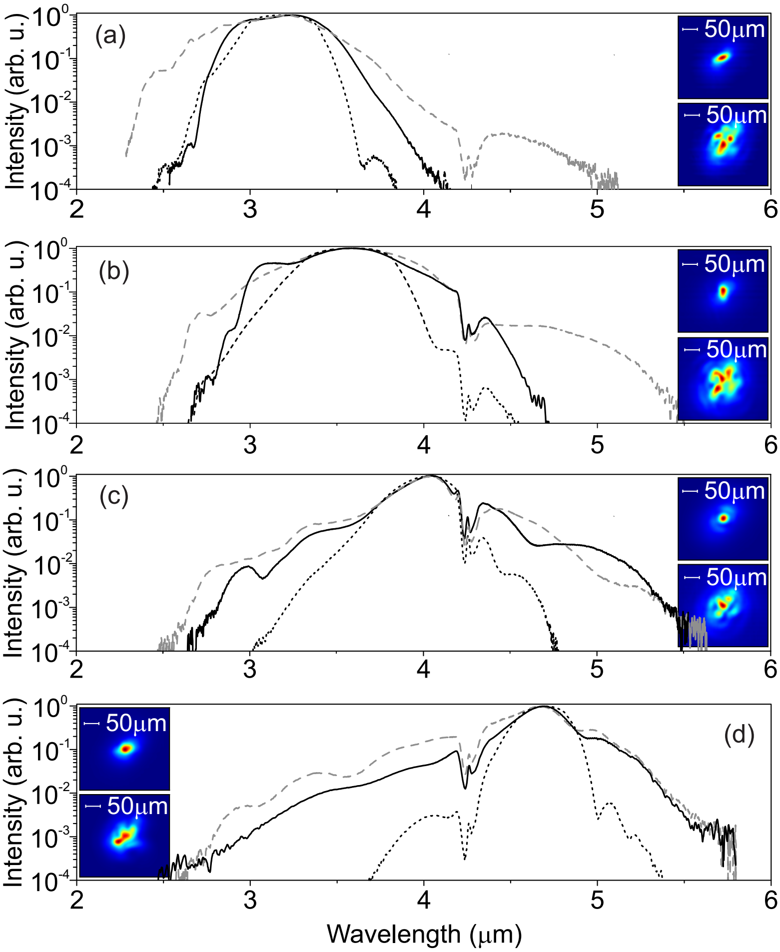

Figure 2.1: Supercontinuum spectra at the output of a 6.4 mm-thick silicon sample, measured in the regimes of single (black solid curve) and multiple (gray dashed curves) filamentation as pumped by (a) 3.25, (b) 3.6, (c) 4.0 and (d) 4.7 μm pulses. The input pulse spectra are depicted by dotted curves. Insets show the near-field fluence profiles of single (top insets on each panel) and multiple (bottom insets) filaments.

Figure 2.1 shows the SC spectra produced by filamentation of the pulses with carrier wavelengths of (a) 3.25, (b) 3.6, (c) 4.0, and (d) 4.7 µm. The black solid curves show the SC spectra recorded with the input pulse energies of 160, 170, 185, and 210 nJ, respectively, which were set to produce a stable blueshifted cutoff and a single filament at the sample output avoiding the onset of multifilamentation, as illustrated in the insets. The generation of broader SC spectra with increasing the input wavelength confirms the general trend of the increase of the spectral blueshift from the carrier wavelength with the higher order of multiphoton absorption (it increases from 3 to 5) [7]. The measured blueshifts of the SC spectra lie in the range of 2.5–2.7 µm and are almost constant regardless of the input pulse wavelength, confirming that the main factor that limits the SC cutoff on the short-wavelength side is the material GVD [10]. This also explains why the SC spectra generated with shorter wavelengths (3.25 and 3.6 µm) are mainly redshifted. The broadest SC spectrum covering the 2.5–5.8 µm wavelength range (at the 10^{-4} intensity level), whose width corresponds to 1.21 optical octaves, is produced with the input pulses at 4.7 µm. Also notice a distinct signature of atmospheric CO_2 absorption around 4.25 µm that is clearly visible in all SC spectra.

The general trends of the spectral broadening were maintained in the multiple filamentation regime. The gray dashed curves depict the SC spectra recorded with elevated input pulse energies (625 nJ at 3.25 µm, 900 nJ at 3.6 µm, 690 nJ at 4.0 µm, and 850 nJ at 4.7 µm). With the input wavelengths of 3.25 and 3.6 µm, slightly broader SC spectra with larger redshifts were generated, whereas the SC spectra produced by longer wavelengths were essentially of the same width, as produced by a single filament.

Figure 2.2 presents the spatiotemporal intensity distributions of the single filaments with carrier wavelengths of 3.6 and 4.7 µm, which were measured by varying the input pulse energy around the threshold values for filamentation (50 and 110 nJ, respectively). The intensity distributions were measured by applying spatiotemporal imaging, details of which can be found in the *Experimental Methods* chapter. Since the sample length was fixed, energy variation allowed to capture the spatiotemporal profiles of the wave packet virtually before and after the nonlinear focus. The left column of Fig. 2.2 shows how the incident spatially and temporally Gaussian-shaped pulse with a duration of 60 fs and a central wavelength of 3.6 µm [Fig. 2.2(a)] shrinks in the spatial dimension due to self-focusing, while approaching the nonlinear focus (the input pulse energy 45 nJ), as depicted in Fig. 2.2(b). At the same time, the pulse experiences broadening in time due to material GVD (the calculated dispersion length of 60 fs pulse at 3.6 µm is 3 mm), as well as due to four-photon absorption that acts mainly on the pulse top. Figure 2.2(c) presents the spatiotemporal intensity distribution of the wave packet after it passes the nonlinear focus (the input pulse energy 55 nJ), showing splitting of the pulse on the propagation axis ($r = 0$) that is accompanied by formation of a ring-like structure in the central part of the pulse, seen as elongated stripes parallel to the propagation axis if projected in the r-t plane. The recorded transformations are very much in line with spatiotemporal dynamics of femtosecond filaments in normally dispersive dielectric materials, see, e.g., [83].

Qualitatively very similar spatiotemporal transformations were captured with the input pulses with a duration of 106 fs and a central wavelength of 4.7 µm, whose spatiotemporal intensity distribution is shown in Fig. 2.2(d).

The input pulse energies of 100 and 130 nJ were used for recording the representative spatiotemporal intensity distributions of the wave packet before and after the nonlinear focus, respectively. In the present case, the dispersive broadening of the pulse before the nonlinear focus was much smaller due to longer input pulse duration and lower material dispersion (the calculated dispersion length of 106 fs pulse at 4.7 μm is 12 mm). On the other hand, the effects related to filament-induced plasma become more pronounced as the cross section for inverse Bremsstrahlung scales as λ^2 [117]. Before the nonlinear focus, the wave packet develops a faint conical tail, seen as the V-shaped structure in the r-t plane in Fig. 2.2(e) that is attributed to plasma absorption and defocusing of the trailing part of the pulse. The conical tail persists also after the nonlinear focus, where the pulse splitting occurs, as shown in Fig. 2.2(f). Notice that these features are only barely detectable in Figs. 2.2(b) and (c).

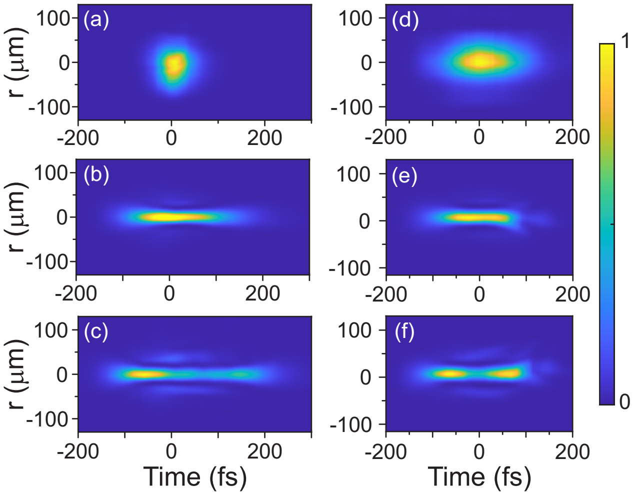

Figure 2.2: Spatiotemporal intensity distributions of the input (a, d) and output wave packets at 3.6 μm (left column) and 4.7 μm (right column), recorded with the input pulse energies slightly below ((b) 45 nJ, (e) 100 nJ) and slightly above ((c) 55 nJ, (f) 130 nJ) filamentation thresholds.

Figure 2.3 shows the central cross sections of the spatiotemporal intensity distributions of multiple filaments in the (a) x-t and (b) y-t planes. Here multiple filaments were produced by launching 60 fs, 3.6 μm pulses with an energy of 900 nJ. The images show that multiple filamentation yields a complex spatiotemporal profile, although some relevant details, such as pulse splitting in the individual filaments can be easily resolved. The interactions between the adjacent filaments result in an occurrence of skewed structures in the entire space–time domain. These complex spatiotemporal intensity patterns suggest that an extra spectral broadening that is measured in the regime of multiple filamentation (see Fig. 2.1) is achieved at the cost of loss of spatial and temporal coherence. As a final note, we should mention that no optical damage of the silicon sample was observed while performing the experiments at a 1 kHz repetition rate.

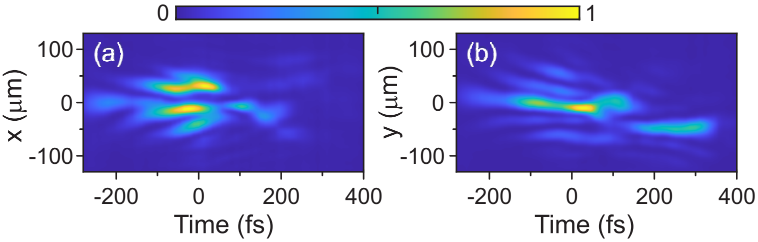

Figure 2.3: Central cross sections of the spatiotemporal intensity distributions of multiple filaments in the (a) x-t and (b) y-t planes, produced by self-focusing of 60 fs, 900 nJ input pulses at 3.6 μm.

2.2. Femtosecond infrared supercontinuum generation in 6H-SiC crystal

This section reports the study of supercontinuum generation in 6H-SiC crystal with femtosecond laser pulses tunable in 1.3-2.4 μm spectral region. We also measured the nonlinear energy transmission of the light filament in 6H-SiC sample which was then used to estimate the nonlinear refractive index of the material at 2 μm.

The experiments were performed using an optical parametric amplifier pumped by an amplified Ti:sapphire laser system. In the experiment either signal or idler wave from the OPA was used, providing the tuning range of the pump pulses from 1.2 to 2.4 μm. For a more in-depth description of the experimental setup and measurement techniques used in this study the reader is referred to the *Experimental Methods* chapter.

As seen from Table 2.1, 6H-SiC possesses a useful combination of linear and nonlinear optical properties: a reasonable transparency range, large nonlinear refractive index and high optical damage threshold, that could be readily exploited for observation of filamentation phenomena and SC generation in particular. First of all, considering the bandgap of 6H-SiC, three to five photon absorption is expected in the range of available pump wavelengths, thus satisfying the threshold condition ($K \geq 3$ where K is the order of multiphoton absorption) for SC generation [7]. Secondly, if compared to YAG - one of the most popular media for SC generation in the near to mid-IR range - the bandgap of 6H-SiC is a few times smaller, which as a general rule of thumb, indicates that its optical damage threshold is significantly lower (damage threshold of YAG is 3 J/cm^2 [118]). However, this is outweighed by the fact that the nonlinear index of refraction of 6H-SiC is expected to be around 15 times larger than that of YAG ($n_2 = 6.2 \times 10^{-16}$ cm^2/W [81] in the case of YAG), which suggests a much lower energy threshold for SC generation. Thirdly, the zero GVD wavelength of 6H-SiC is at 2.1 μm allowing the access to femtosecond filamentation in the anomalous GVD regime, characterized by simultaneous compression in space and time and light-bullet formation [119], which in turn yields generation of ultrabroadband, multioctave SC [64, 120].

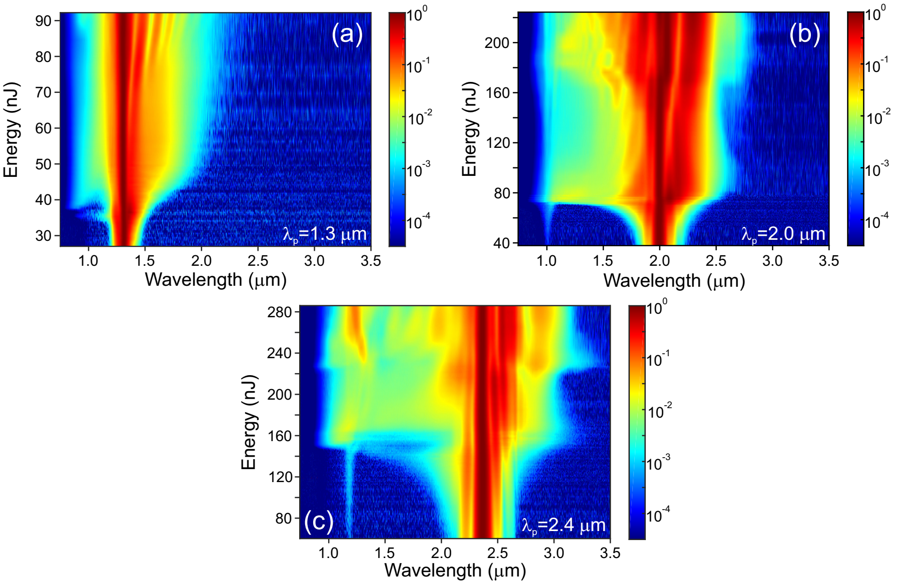

Figure 2.4: Measured dynamics of spectral broadening in 6H-SiC crystal recorded with (a) 88 fs, 1.3 μm, (b) 93 fs, 2 μm and (c) 125 fs, 2.4 μm pump pulses as functions of pulse energy. Logarithmic intensity scale is used in order to highlight fine spectral features.

Figure 2.4 shows the dynamics of spectral broadening in 6H-SiC versus the pump pulse energy measured using input pulses of three different wavelengths (1.3, 2.0 and 2.4 μm), falling into the normal, zero and anomalous GVD of the material. As can be seen from Fig. 2.4 (a), when pumped with 1.3 μm pulses, spectral broadening starts at around 40 nJ although the SC spectral extent is rather modest and is basically red-shifted, since spectral blue-shift is limited by the order of multiphoton absorption. Around 80 nJ spectral modulation occurs due to the light filament self-focusing for the second time.

In the case of 2.0 μm pump pulses, an explosive spectral broadening is observed above the threshold energy of 73 nJ, where a smooth SC spectrum spanning almost the entire near-IR spectral region and extending into the mid-infrared is produced. The low SC generation energy threshold is determined by the large nonlinear refractive index of 6H-SiC, see Table 2.1. A fairly constant width of the SC spectrum is maintained with further increase of the pump pulse energy, until a second burst of spectral broadening is observed at approximately 180 nJ, accompanied by spectral modulation that indicates the refocusing of the filament. Qualitatively similar SC dynamics can be observed with input pulses of 2.4 μm (Fig. 2.4 (c)).

With the input pulses of 2.0 and 2.4 μm, below the SC generation threshold, a faint but clearly distinguishable signal with a center wavelength around 1 μm is observed, which is attributed to phase-mismatched second harmonic generation. Since 6H-SiC is a positive uniaxial crystal, the pump pulse polarization was intentionally set to be ordinary to minimize second harmonic generation in order to avoid spectral "contamination". It should be noted that at the OPA output the signal (1.3 and 1.5 μm) and the idler (2.0 and 2.4 μm) waves are of orthogonal polarizations due to type-II phase matching in the OPA crystal. Therefore, the polarization of the idler wave was rotated by 90 degrees (by means of a periscope) to be identical to that of the signal wave.

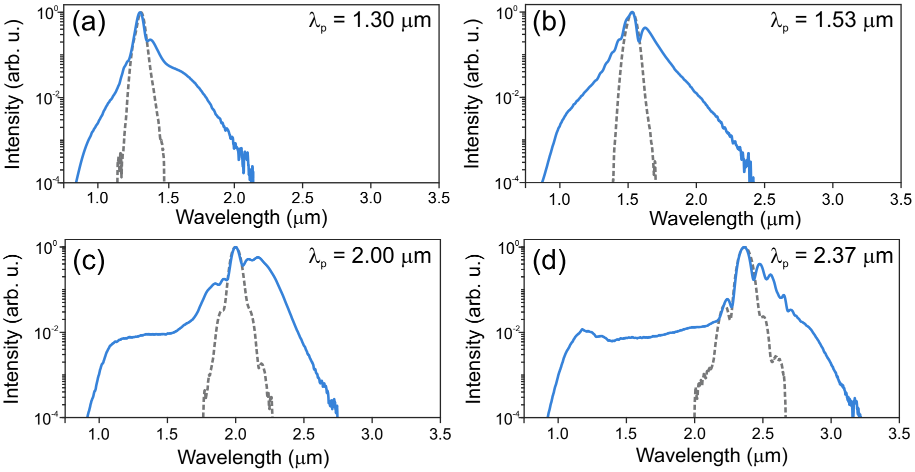

Figure 2.5: Supercontinuum spectra generated in 6H-SiC using pump pulses with energies of (a) 55 nJ, (b) 70 nJ, (c) 90 nJ, and (d) 180 nJ. The central wavelengths of the pump pulses are indicated within the figures. The input spectra are depicted by grey dashed curves.

Figure 2.5 presents the SC spectra measured with four different wavelengths: 1.3, 1.5, 2.0 and 2.4 μm, and using pump pulse energies of 55, 70, 90 and 180 nJ, respectively, at which the spectral broadening saturates without filament refocusing. Notice an apparent change of the width and the shape of SC spectra from the red-shifted to symmetric and eventually to the blue-shifted, when the pump wavelength is tuned from normal to anomalous GVD regions of the nonlinear material (zero GVD wavelength is 2.1 μm). More specifically, with 1.3 μm pump pulses, the measured SC spectrum exhibits a red-shift and covers the wavelength range from 0.85 to 2.13 μm, as evaluated at the 10^{-4} intensity level, see Fig. 2.5(a). A slightly broader and symmetric SC spectrum in the wavelength range of 0.87-2.40 μm was produced with 1.5 μm pump pulses, as shown in Fig. 2.5(b). The broadest SC spectra with strongly pronounced blue-shifts were measured in the regions of near-zero and anomalous GVD, with pump wavelenghts of 2.0 and 2.4 μm, as illustrated in Figs. 2.5(c) and 2.5(d), respectively. In the first case, the SC spectrum covers the 0.91-2.75 μm wavelength range, while in the latter case the SC spectrum extends from 0.92 to 3.21 μm and spans for 1.8 optical octaves. The shapes of all measured SC spectra are smooth and do not contain any significant dips or detached peaks. Also note the generally low energies of the pump pulses (varying from 55 to 180 nJ) required to achieve a fully evolved spectral broadening without the onset of filament refocusing. The apparent increase of the pump pulse energy with the wavelength follows fairly well the square wavelength dependence of the critical power for self-focusing.

Additional information on the expansion of the SC spectrum is presented in Figure 2.6, where the dependences of 6H-SiC GVD (a) and the measured SC blue-shift (b), defined at the 10^{-4} intensity level, on pump wavelength are plotted. The increase of the spectral blue shift with the increase of the pump wavelength could be attributed to a lower material GVD and a higher value of the clamped intensity, as the order of multiphoton absorption gradually increases from 3 at 1.3 μm to 5 at 2.4 μm [7].

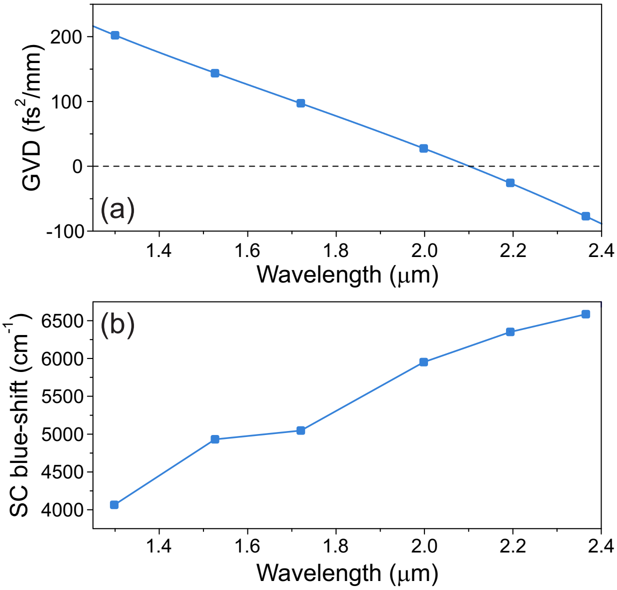

Figure 2.6: (a) GVD of 6H-SiC and (b) supercontinuum spectral blue-shift versus the pump wavelength.

Finally, in order to obtain an experimental nonlinear refractive index value, we have measured the energy transmission through 6H-SiC sample of 5 mm thickness. The nonlinear refractive index evaluation procedure is described in detail in the *Nonlinear Refractive Index Evaluation* section of the *Experimental*

Methods chapter. The normalized energy transmission curve measured using pump pulses at 2.0 μm, is depicted in Fig. 2.7(a). Figure 2.7(b), shows the calculated fractional losses, with a peak at 66 nJ. Therefore, the value of the nonlinear refractive index, $n_2 = (97 \pm 19) \times 10^{-16}$ cm^2/W, at 2.0 μm pump wavelength was found using the Marburger's law [3]. The peak power of the pump pulse was calculated using a Gaussian pump pulse duration of 93 fs FWHM (see Fig. 2.7 (c) autocorrelation trace) and beam size was measured by means of knife method showing a radius of 53 μm at 1/e^2 intensity level at the lens focus which coincided with the input face of the sample. The measured n_2 value agrees well with the expected one provided in Table 1 and the small discrepancy between the measured and calculated values could be attributed to the margin of error.

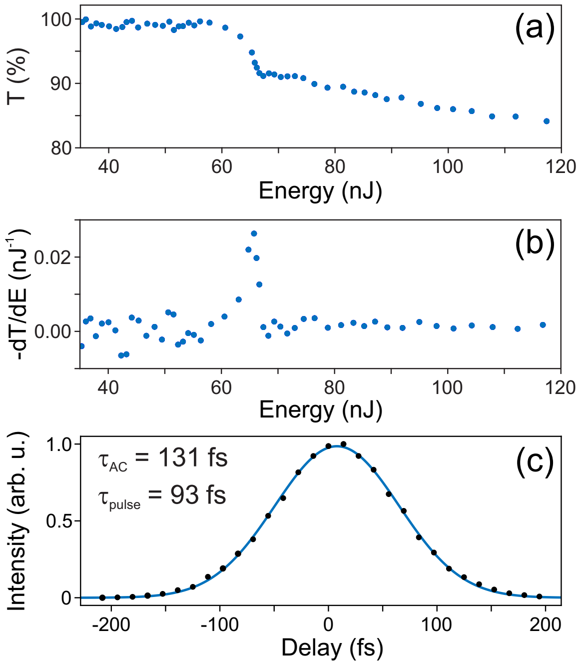

Figure 2.7: (a) Normalized energy transmission of a 5 mm-thick 6H-SiC sample versus the pump pulse energy. (b) Fractional losses, where the maximum indicates that the nonlinear focus is positioned exactly at the output face of the sample. (c) Measured intensity autocorrelation function of 2.0 μm pump pulses.

Summary of the results

First of all, in bulk silicon, octave-spanning SC spectra were produced with the input wavelengths of 4.0 and 4.7 µm, in the presence of four- and five-photon absorption, respectively. It was also shown that free-carrier absorption does not alter the spatiotemporal filamentation dynamics, supporting the general conclusion of [99] that nonlinear propagation of femtosecond pulses in silicon, as opposed to the longer ones, is less affected by free carriers.

Secondly, we have shown the generation of smooth, more than an octave-spanning supercontinuum spectra in 6H-SiC produced by femtosecond filamentation of input pulses with wavelengths falling into the normal, zero and anomalous GVD regions of the material. We also experimentally evaluated the nonlinear index of refraction of 6H-SiC at 2.0 μm by measuring the nonlinear energy transmission and applying Marburger's law. The obtained value ($n_2 = (97 \pm 19) \times 10^{-16}$ cm^2/W) coincides fairly well with the theoretically calculated one and is supported by the observed low energy thresholds for supercontinuum generation.

Finally, the study of supercontinuum generation in silicon and 6H-SiC crystals revealed the key physical effects and the basic features of femtosecond filamentation in semiconductors. Input pulse splitting into two sub-pulses was observed during femtosecond filamentation in the range of normal GVD in silicon. Also, the spectral measurements in both silicon and 6H-SiC samples revealed the limiting factors that determine the spectral extent of supercontinuum - the order of multiphoton absorption and material GVD. The influence of these two effects on supercontinuum spectral blue-shift is summarized in Fig. 2.8.

Overall, our results suggest that both crystalline silicon and 6H-SiC are attractive nonlinear materials that may readily serve for the generation of an octave-spanning SC in the near- and mid-infrared.

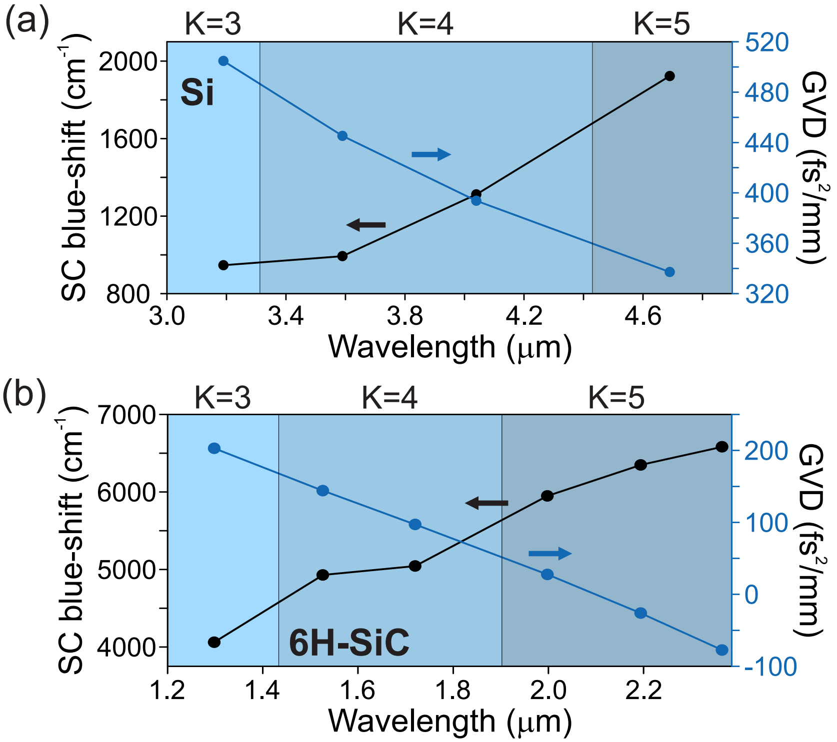

Figure 2.8: Supercontinuum blue-shift and material GVD versus the wavelength of the incident pulses in (a) Si, (b) 6H-SiC. Coloured sections and text above the graphs represent the order of multiphoton absorption.

CONCLUSIONS

1. Narrow band gap dielectric (KRS-5, KRS-6 and SBN) and semiconductor (silicon and 6H-SiC) crystals due to their broad infrared transmission window and high cubic nonlinearity are excellent materials for low threshold supercontinuum generation in the infrared producing spectral widths of more than an octave as pumped by femtosecond near- and mid-infrared pulses.

2. Wide band gap dielectric crystals NaCl and KBr provide multi-octave supercontinuum spectra (0.7-5.4 μm in NaCl and 0.85-5.4 μm in KBr, at the 10^{-4} intensity level) when pumped by mid-infrared femtosecond pulses. However, due to formation of color centers which absorb in the visible and ultraviolet, supercontinuum spectra shrink considerably and become qualitatively similar (1.8-5.1 μm in NaCl and 1.9-4.85 μm in KBr) to those generated in narrow band gap materials.

3. Energy transmission measurements through the investigated material samples reveal the onset of nonlinear losses and offer a simple method for nonlinear refractive index evaluation. This method was used to determine the nonlinear refractive index values of KRS-5 ($n_2 = (105 \pm 19) \times 10^{-16}\text{cm}^2/\text{W}$), KRS-6 ($n_2 = (54 \pm 10) \times 10^{-16}\text{cm}^2/\text{W}$) both measured at 3.1 μm and 6H-SiC measured at 2 μm ($n_2 = (97 \pm 19) \times 10^{-16}$ cm^2/W) which coincided well with the calculated ones.

4. Pulse splitting observed in the spatiotemporal intensity distributions during femtosecond filamentation in bulk silicon confirmed that the supercontinuum generation mechanism in normal group velocity dispersion regime is universal and that the influence of free carriers in undoped semiconductors during the propagation of intense femtosecond laser pulses is insignificant.

5. Measured supercontinuum spectra generated with various pump wavelengths in bulk silicon, 6H-SiC and SBN crystals show a stable cut-off wavelength and increasing blue-shift with increasing pump wavelength and indicate that the material group velocity dispersion and the order of multi-photon absorption are the main limiting factors of spectral broadening on the short-wavelength side both in narrow band gap dielectric and undoped semiconductor crystals.

SANTRAUKA LIETUVIŲ KALBA

Įvadas

Superkontinuumo generacija yra unikalus netiesinis reiškinys, stebimas skaidriose terpėse intensyvių ultratrumpųjų lazerinių impulsų sklidimo ir šviesos gijų formavimosi metu. Superkontinuumo generacijos reiškinys gali būti apibūdinamas kaip ekstremalus spektro išplitimas (pradinis impulsų spektras gali išplisti šimtus ar net tūkstančius kartų) [1], sąlygotas sudėtingos sąveikos tarp efektų kaip pluošto fokusavimasis, impulso fazės moduliavimasis, dispersija, netiesinė sugertis, laisvųjų elektronų plazmos formavimasis ir pan. Pirmą kartą superkontinuumo generacija žadinant femtosekundiniais impulsais buvo stebėta dar 1983 [2]. Bėgant metams supratimas apie superkontinuumo generaciją evoliucionavo kartu su gilesnėmis netiesinės optikos žiniomis bei tobulėjančiais femtosekundiniais lazeriais ir šiuo metu superkontinuumo generacija tapo itin universaliu, pigiu, patikimu, efektyviu bei paprastu būdu generuoti plačiajuostę femtosekundinę spinduliuotę optiniame diapazone.

Femtosekundinių šviesos gijų formavimąsi bei superkontinuumo generaciją skaidriose kietakūnėse terpėse lemia eilė fizikinių reiškinių. Daugelis jų yra susiję su medžiagos trečiosios eilės netiesiniu optiniu jautriu. Vienas tokių reiškinių - pluošto fokusavimasis, atsirandantis dėl optinio Kero efekto, kuris yra apibūdinamas medžiagos lūžio rodiklio priklausomybe nuo intensyvumo:

$$n = n_0 + n_2 I, \tag{2.1}$$

čia n_0 ir n_2 atitinkamai yra tiesinis ir netiesinis lūžio rodiklis, o I yra spinduliuotės intensyvumas. Netiesinis lūžio rodiklis yra susijęs su medžiagos trečiosios eilės netiesiniu optiniu jautriu:

$$n_2 = \frac{3}{4n_0^2 c\epsilon_0}\chi^{(3)}(\omega;\omega,\omega,-\omega), \tag{2.2}$$

čia c yra šviesos greitis vakuume, ϵ_0 yra vakuumo dielektrinė skvarba, o $\chi^{(3)}(\omega;\omega,\omega,-\omega)$ yra trečiosios eilės netiesinis optinis jautris.

Kaip matyti, netiesinis lūžio rodiklis yra tiesiogiai proporcingas trečiosios eilės netiesiniam optiniam jautriui. Dėl šios priežasties intensyvus Gauso pluoštas, sklindantis teigiamu netiesiniu lūžio rodikliu pasižyminčia terpe, pradės fokusuotis - intensyvi centrinė pluošto dalis patirs didesnį lūžio rodiklį nei mažiau intensyvi pluošto periferija. Kitaip tariant, medžiaga, kuria sklinda pluoštas, veiks kaip glaudžiamasis lęšis. Jeigu netiesinis lūžio rodiklis bus neigiamas, medžiaga veiks kaip sklaidomasis lęšis ir pluoštas bus defokusuojamas.

Pluošto fokusavimosi slenkstis yra apibūdinamas kritine fokusavimosi galia P_{cr} - tokia galia, kurią pasiekus pluošto fokusavimasis pilnai kompensuoja difrakcinę lazerio pluošto skėstį. Gauso pluoštui kritinės fokusavimosi galios išraiška yra tokia:

$$P_{cr} = \frac{3,77\lambda^2}{8\pi n_0 n_2}, \tag{2.3}$$

čia λ yra spinduliuotės bangos ilgis. Jei pluošto galia yra didesnė už P_{cr}, jis susifokusuos už atstumo, kurį galima įvertinti naudojantis empirine Marburgerio formule [3]:

$$z_{sf} = \frac{0,367 z_R}{\sqrt{[(P/P_{cr})^{1/2} - 0,852]^2 - 0,0219}}, \tag{2.4}$$

čia $z_R = \pi n_0 w_0^2/\lambda$ yra Reilėjaus (difrakcinis) ilgis Gauso pluoštui, kurio pradinis spindulys yra lygus w_0, vertinant $1/e^2$ intensyvumo lygyje. Nors Marburgerio formulė yra empiriškai gauta nuolatinės veikos lazeriniams pluoštams, ji yra tinkama ir netiesinio židinio nustatymui naudojant femtosekundinius lazerinius impulsus [5].

Dar vienas netiesinio lūžio rodiklio nulemtas reiškinys yra impulso fazės moduliavimasis, kartais vadinamas laikiniu pluošto fokusavimosi analogu. Laike kintantis intensyvumas lemia medžiagos lūžio rodiklio laikinį kitimą, dėl kurio atsiranda netiesinis fazės pokytis:

$$\phi_{nl} = \frac{\omega_0}{c} n_2 I(t) z, \tag{2.5}$$

čia ω_0 yra nešlio dažnis, z - sklidimo atstumas, o $I(t)$ - laike kintantis intensyvumas. Netiesinis fazės pokytis kaupiasi didėjant sklidimo atstumui, o laike kintanti fazė lemia momentinio dažnio pokytį, todėl galima užrašyti:

$$\delta\omega(t,z) = \frac{\partial \phi_{nl}(t)}{\partial t} = \frac{\omega_0 z}{c} n_2 \frac{\partial I(t)}{\partial t}, \tag{2.6}$$

čia $\phi_{nl}(t)$ - laike kintanti netiesinė fazė. Matyti, jog fazės moduliacija sukelia ir impulso nešlio dažnio moduliaciją, vadinasi, impulso spektras yra papildomas naujais spektriniais komponentais, t.y. jis tampa platesnis. Gauso impulsui, kurio trukmė yra t_p, momentinio dažnio pokytis gali būti užrašytas taip:

$$\delta\omega(t,z) = -2\frac{\omega_0 tz}{ct_p^2} n_2 I_0 exp(-\frac{t^2}{t_p^2}), \tag{2.7}$$

čia I_0 yra smailinis intensyvumas. Jei medžiagos netiesinis lūžio rodiklis yra teigiamas, tuomet impulso priekinis frontas patirs neigiamą (Stokso), o galinis frontas - teigiamą (anti-Stokso) dažnio pokytį, vadinasi, impulso priekinis frontas pasipildys raudonaisiais, o galinis frontas - mėlynaisiais spektriniais komponentais. Jeigu $n_2 < 0$, bus stebimas atvirkščias efektas.

Šviesos gijų formavimasis gali būti įsivaizduojamas kaip dinamiška pusiausvyra tarp pluošto fokusavimosi ir defokusavimosi ciklų [5]. Teoriškai pirmuoju artėjimu Bangų paketo galiai viršijus kritinę fokusavimosi galią, jis turėtų sumažėti iki nykstamai mažų matmenų ir kolapsuoti, o intensyvumas turėtų artėti link begalybės. Kita vertus, realybėje, pasiekus tam tikrą intensyvumą, o tai atsitinka artėjant link netiesinio židinio, reiškiniai, kaip daugiafotonė sugertis, laisvųjų elektronų plazmos generacija bei plazmos sugertis, pradeda riboti minimalius pluošto pasiekiamus matmenis ir neleidžia jam kolapsuoti. Vykstant daugiafotonei sugerčiai, elektronai yra sužadinami į laidumo juostą taip formuodami laisvųjų elektronų plazmą, kuri pasižymi neigiamu netiesiniu lūžio rodikliu ir defokusuoja pluoštą. Šis reiškinys yra vadinamas intensyvumo ribojimu. Taigi, intensyviausia centrinė pluošto dalis patiria netiesinius nuostolius bei laisvųjų elektronų plazmos defokusavimą. Kita vertus, jeigu bangų paketo galia vis dar viršija kritinę fokusavimosi galią, pluoštas ima fokusuotis iš naujo ir ciklas kartojasi.

Erdvinė femtosekundinių šviesos gijų struktūra yra pakankamai sudėtinga: šviesos giją sudaro intensyvi centrinė smailė, apsupta koncentrinių žiedų formos mažo intensyvumo, didelės energijos periferijos. Vykstant netiesiniam sklidimui, su medžiaga sąveikauja tik centrinė šviesos gijos smailė, o energijos nuostoliai yra kompensuojami iš pluošto periferijos, kuri atlieka energijos rezervuaro funkciją. Tik apie 10% šviesos gijos energijos yra sutelkta centrinėje smailėje, kurią užblokavus, ji atsikuria iš pluošto periferijos. Kita vertus, jeigu yra užblokuojama periferija, centrinė smailė difraguoja ir išsisklaido. Šiuo požiūriu, šviesos gijos gali būti traktuojamos kaip kūginiai pluoštai [6].

Femtosekundinių šviesos gijų formavimasis bei netiesinis sklidimas yra glaudžiai susiję su superkontinuumo generacija. Eksperimentiškai pademonstruota, jog superkontinuumo generacijos slenkstinė galia yra šiek tiek didesnė už kritinę fokusavimosi galią. Superkontinuumo generacijos metu stebimas spektro plitimas priklauso nuo keleto fizikinių parametrų. Vienas iš jų yra daugiafotonės sugerties eilė:

$$K = \langle U_g/\hbar\omega_0 \rangle + 1, \tag{2.8}$$

čia U_g yra terpės draustinės juostos tarpas, o $\hbar\omega_0$ yra į terpę krintančių fotonų energija. Kuo didesnė yra daugiafotonės sugerties eilė, tuo didesnis intensyvumas gali būti pasiektas netiesiniame židinyje prieš pradedant reikštis intensyvumo ribojimui ir tuo platesnis yra superkontinuumo spektras [7,8]. Dėl šios priežasties plačiausi superkontinuumo spektrai yra generuojami plataus draustinės juostos tarpo dielektrikuose. Tačiau jeigu daugiafotonės sugerties eilė yra mažesnė negu 3, superkontinuumo generacija nevyksta. Dar vienas įdomus pastebėjimas sieja medžiagos draustinės juostos tarpą bei netiesinį lūžio rodiklį: kuo didesnis draustinės juostos tarpas, tuo mažesnis netiesinis lūžio rodiklis [9]. Galiausiai, remiantis skaitinio modeliavimo rezultatais parodyta, jog medžiagos dispersija irgi yra svarbi charakteristika, nulemianti superkontinuumo formą bei plotį. Medžiagos dispersijos įtaką superkontinuumo generacijai galima įvertinti remiantis efektyvaus tribangio maišymosi modeliu. Tokiu atveju superkontinuumo generacija yra traktuojama kaip naujų dažnių generacija, atsiradusi dėl pradinio optinio lauko sklaidos per netiesinę poliarizaciją [10, 11]. Paprasčiau tariant, mažesnė medžiagos dispersija užtikrina fazinio sinchronizmo sąlygų tenkinimą platesniam dažnių diapazonui.

Laikinė bei spektrinė superkontinuumo generacijos dinamika taip pat priklauso ir nuo medžiagos grupinių greičių dispersijos (GGD), kuri gali būti išreikšta taip:

$$GGD = k_0^{''} = \partial^2 k/\partial\omega^2|_{\omega_0}, \tag{2.9}$$

čia $k = \omega_0 n_0/c$ yra bangos skaičius, ω_0 - nešlio dažnis. Jeigu medžiagos grupinių greičių dispersija yra teigiama (arba normalioji), raudonieji spektriniai komponentai medžiaga sklinda greičiau už mėlynuosius. Jeigu GGD yra neigiama (arba anomalioji), vyksta atvirščias efektas. Kokybiškai yra išskiriami trys superkontinuumo generacijos režimai, priklausomai nuo medžiagos GGD koeficiento žadinančiųjų impulsų centriniam bangos ilgiui: normaliosios, nulinės bei anomaliosios GGD.

Normaliosios GGD atveju, superkontinuumo generacijos dinamika yra lemiama impulsų laikinio skilimo. Dėl fazės moduliavimosi nauji raudonieji spektriniai komponentai atsiranda impulso priekyje, o mėlynieji - gale. Teigiama medžiagos GGD dar labiau atskiria raudonuosius bei mėlynuosius komponentus, kol galiausiai netiesiniame židinyje impulsas skyla į du subimpulsus su skirtingais nešlio dažniais. Dėl šios priežasties, laikinėje pradinio impulso atskaitos sistemoje, susiformavę sub-impulsai juda priešingomis kryptimis. Impulso skilimą lydi staigus spektrinis išplitimas, kurį lemia sub-impulsų frontų statėjimas. Sub-impulsų fronto statėjimą savo ruožtu sukelia skirtingi intensyvios sub-impulsų viršunių bei mažesnio intensyvumo frontų greičiai, kartu sąlygojantys didžiulį laikinį intensyvumo gradientą. Fronto statėjimo mastas abiems sub-impulsams yra skirtingas, o tai paaiškina asimetrinį superkontinuumo spektro plitimą. Esant tipinėms fokusavimo sąlygoms, ypač status frontas susiformuoja antrojo sub-impulso gale, kuris yra atsakingas už spektro plitimą į mėlynąją pusę. Spektro plitimas į raudonąją pusę yra mažiau išreikštas dėl mažesnio pirmojo sub-impulso priekinio fronto statėjimo. Toks superkontinuumo generacijos normaliojoje GGD srityje dinamikos paaiškinimas yra universalus ir įrodytas eksperimentiškai [12].

Žadinančiojo impulso centriniam bangos ilgiui esant anomaliojoje medžiagos GGD srityje yra stebimas visai kitoks superkontinuumo generacijos scenarijus. Šiuo atveju, impulso fokusavimasis, fazės moduliavimasis bei medžiagos anomalioji GGD veikia bangų paketą taip, jog jis pradeda trauktis tiek erdvėje, tiek ir laike - formuojasi šviesos kulka [13]. Dėl impulso fazės moduliavimosi priekinis impulso frontas yra papildomas raudonaisiais spektriniais komponentais, kurie dėl anomaliosios medžiagos GGD sklinda lėčiau už mėlynuosius spektrinius komponentus, atsirandančius galiniame impulso fronte. Vadinasi, tiek raudonieji, tiek mėlynieji komponentai juda link impulso centro ir vyksta impulso laikinė savispūda. Skaitinis modeliavimas patvirtino aprašytą spektrinę bei erdvėlaikinę dinamiką ir potencialią impulso savispūdą iki vieno optinio ciklo [14–16].

Galiausiai, jeigu žadinančiųjų impulsų centrinis bangos ilgis sutampa su nuline medžiagos GGD, superkontinuumo generacijos dinamika turi tiek normaliajai, tiek anomaliajai GGD sričiai būdingų bruožų. Superkontinuumo spektrai, gauti nulinės GGD režime, yra itin simetriški, o normaliosios GGD srities atveju spektrai yra asimetriniai su didesniu plitimu į mėlynają pusę. Laikinėje plotmėje superkontinuumo generacijos nulinės GGD režimo metu stebimas impulsų skilimas netiesiniame židinyje, t.y. laikinė bangų paketo dinamika primena normaliosios GGD atvejį. Buvo parodyta, jog net ir silpnai anomalios GGD nepakanka užtikrinti spektriškai išplitusio impulso savispūdai ir sustabdyti impulso skilimą [17].

Superkontinuumo generacija jau kurį laiką yra žinoma kaip kompaktiškas, universalus bei efektyvus būdas generuoti plataus spektro femtosekundinius impulsus regimojoje spektrinėje srityje. Kita vertus, sparčiai vystantis tokioms mokslo šakoms kaip OPCPA (angl. Optical Parametric Chirped Pulse Amplifier - faziškai moduliuotų impulsų optinis parametrinis stiprintuvas) kūrimas [18], virpesinė spektroskopija [19, 20], puslaidininkių optoelektronika [21], dažnio šukų technologijos [22], dujų detekcija [23] ir pan., yra pastebimas vis didėjantis artimosios bei viduriniosios infraraudonosios srities plačiajuostės koherentinės femtosekundinės spinduliuotės poreikis. Šį poreikį lengvai patenkinti gali superkontinuumo generacija infraraudonojoje spektrinėje srityje. Tačiau pačios populiariausios medžiagos, naudojamos superkontinuumo generacijai regimojoje srityje, tokios kaip safyras, YAG ar lydytas kvarcas yra netinkamos vidurinei infraraudonajai spektrinei sričiai dėl šioje srityje esančio sugerties krašto: lydytas kvarcas pradeda sugerti ties 3,5 μm, o safyras bei YAG - maždaug ties 5,2 μm. Taip pat žadinant superkontinuumą didesnio bangos ilgio impulsais, superkontinuumo spektras fluoridų kristaluose (pvz. BaF_2, CaF_2) praranda vientisumą, formuojasi atskiros spektrinės smailės [25,26]. Dėl šios priežasties superkontinuumo generacijai infraraudonojoje spektro srityje reikalingos kitokiomis optinėmis savybėmis pasižyminčios medžiagos.

Neseniai atlikti eksperimentiniai bei teoriniai tyrimai rodo, jog egzistuoja itin plati alternatyvių medžiagų, potencialiai tinkamų infraraudonojo superkontinuumo generacijai, įvairovė - tai siauro draustinės juostos tarpo dielektrikai. Reiktų pabrėžti, jog šioje disertacijoje siauros draustinės juostos dielektrikais laikomi tie, kurių draustinė juosta yra ne didesnė nei 4,5 eV. Jeigu draustinė juosta viršija 4,5 eV, tokie kristalai yra laikomi plačios draustinės juostos. Plataus superkontinuumo, besitęsiančio iki viduriniosios infraraudonosios spektrinės srities, generacija buvo pademonstruota fluoridų [27], telūritų [28, 29], lantanų [30] bei chalkogenidų [31] stikluose. Taip pat puslaidininkiniai kristalai, pasižymintys dideliu pralaidumu viduriniojoje infraraudonojoje srityje ir nemažomis netiesinio lūžio rodiklio vertėmis, yra potencialiai tinkamos medžiagos vidurinės infraraudonosios srities superkontinuumo generacijai. Kelias optines oktavas apimantis superkontinuumo spektras viduriniojoje infraraudonojoje srityje bei laikinė impulsų spūda iki kelių optinių ciklų buvo pademonstruota GaAs kristale. Sėkminga superkontinuumo generacija, apimanti nuo regimosios iki viduriniosios infraraudonosios spektrinės srities taip pat parodyta ir puslaidininkiuose ZnS bei ZnSe, kurie pasižymi polikristaline struktūra [32–34]. Kita vertus, iš daugelio medžiagų, pasižyminčių infraraudonojo superkontinuumo generacijai tinkamomis savybėmis, iki šiol nuosekliai ištirta yra tik nedidelė dalis.

Darbo tikslas

Šios disertacijos darbo tikslas yra femtosekundinių šviesos gijų formavimosi bei superkontinuumo generacijos tyrimas siauros draustinės juostos dielektriniuose bei puslaidininkiniuose kristaluose artimojoje bei viduriniojoje infraraudonojoje spektrinėje srityje.

Sprendžiami uždaviniai

- Superkontinuumo generacijos eksperimentams skirto femtosekundinio viduriniosios infraraudonosios spektrinės srities šviesos šaltinio, paremto skirtuminio dažnio generacija ir veikiančio 3-5 μm srityje, sukūrimas.

- Superkontinuumo generacijos eksperimentinis tyrimas siauros draustinės juostos dielektriniuose talio bromojodido (KRS-5), talio bromochlorido (KRS-6) ir stroncio bario niobato (SBN) bei puslaidininkiniuose silicio ir silicio karbido (6H-SiC) kristaluose, žadinimui naudojant femtosekundinius infraraudonuosius impulsus, kurių centrinis bangos ilgis yra 1,2-4,7 μm srityje.

- Femtosekundinių šviesos gijų formavimosi erdvėlaikinių savybių tyrimas silicio kristale.
- Spalvinių centrų formavimosi įtakos superkontinuumo generacijai tyrimas šarminių metalų halidų NaCl bei KBr kristaluose, žadinimui naudojant viduriniosios infraraudonosios spektrinės srities femtosekundinius impulsus.

Mokslinis darbo naujumas

- Sukurtas kompaktiškas femtosekundinių viduriniosios infraraudonosios spektrinės srities 60-130 fs trukmės bei iki 11 μJ energijos impulsų šaltinis, paremtas skirtuminio dažnio generacija, veikiantis 3-5 μm spektrinėje srityje, kuris buvo naudojamas superkontinuumo generacijos bei šviesos gijų formavimosi tyrimuose.
- Pasiūlytas paprastas būdas medžiagos netiesinio lūžio rodiklio įvertinimui, paremtas netiesinio energijos pralaidumo matavimu formuojantis šviesos gijoms. Remiantis šiuo būdu eksperimentiškai nustatytas KRS-5, KRS-6 bei 6H-SiC kristalų n_2.
- Parodyta, jog siauros draustinės juostos dielektrikai (KRS-5, KRS-6 ir SBN) bei nelegiruoti puslaidininkiniai kristalai (silicis ir 6H-SiC) yra tinkamos terpės efektyviai infraraudonosios srities superkontinuumo generacijai, kai žadinimui naudojami artimosios bei viduriniosios infraraudonosios spektrinės srities femtosekundiniai impulsai.
- Pademonstruota, jog žadinimui naudojant impulsus, kurių bangos ilgis patenka į normaliąją terpės grupinių greičių dispersijos sritį, superkontinuumo generacijos silicio kristale metu stebimas impulsų skilimas yra universalus reiškinys, vykstantis susidarant šviesos gijoms tiek nelegiruotuose puslaidininkiuose, tiek ir dielektrikuose.
- Pastebėta, jog kelių optinių oktavų pločio superkontinuumo spektrai, generuojami šarminių metalų halidų NaCl bei KBr kristaluose patiria greitą siaurėjimą dėl spalvinių centrų formavimosi, dėl kurių sugerties siaurėja efektyvus terpės draustinės energijos tarpas.

Ginamieji teiginiai

- Dėl didelio pralaidumo infraraudonojoje srityje bei didelio kubinio netiesiškumo, siauros draustinės juostos dielektriniuose (KRS-5, KRS-6 bei SBN) ir puslaidininkiniuose (silicio bei 6H-SiC) kristaluose gali būti generuojamas daugiau nei vienos optinės oktavos pločio infraraudonosios spektrinės srities superkontinuumas, kurio generacijos slenkstis yra labai žemas.

- Energijos pralaidumo matavimas gali būti panaudotas tiksliam netiesinio židinio susiformavimo ant galinio terpės paviršiaus nustatymui bei terpės netiesinio lūžio rodiklio įvertinimui remiantis Marburgerio formule.
- Spalvinių centrų formavimasis šarminių metalų haliduose NaCl ir KBr sukelia efektyvios draustinės juostos siaurėjimą, kas savo ruožtu siaurina superkontinuumo spektrą bei mažina energijos pralaidumą.
- Femtosekundinių šviesos gijų formavimosi nelegiruotoje puslaidininkinėje terpėje metu, kai žadinančiųjų impulsų bangos ilgis patenka į terpės normaliosios grupinių greičių dispersijos sritį, stebimas pradinio impulso skilimas į du sub-impulsus.
- Nelegiruotuose puslaidininkiniuose bei siauros draustinės juostos dielektriniuose kristaluose generuojamo superkontinuumo spektro nukirtimo bangos ilgis beveik nekinta, o mėlynasis poslinkis didėja augant žadinančiųjų impulsų centriniam bangos ilgiui, iš ko matyti, jog pagrindiniai fizikiniai faktoriai, nulemiantys superkontinuumo spektro plitimą į mėlynąją pusę šiose medžiagose, yra grupinių greičių dispersija bei daugiafotonės sugerties eilė.

Pirmiausia įvertinome talio bromojodido (KRS-5) bei talio chlorobromido (KRS-6) netiesinį lūžio rodiklį ir pademonstravome efektyvią superkontinuumo generaciją viduriniojoje infraraudonojoje spektrinėje srityje žadinant 60 fs trukmės impulsais, kurių centrinis bangos ilgis buvo 3,1 ir 3,6 μm. Beveik dviejų optinių oktavų pločio superkontinuumo spektras, apimantis 1,5-5,5 μm spektrinį ruožą (5×10^{-4} intensyvumo lygyje) buvo gautas 6 mm storio KRS-5 bei KRS-6 bandiniuose, kaip matyti iš 1 pav. pateiktos superkontinuumo spektrų, užregistruotų tirtose dielektrinėse medžiagose, suvestinės. Taip pat parodėme, jog šviesos gijų formavimosi ir superkontinuumo generacijos slenkstinės energijos šiose medžiagose yra itin mažos (keli šimtai nanodžaulių). Taip yra dėl didelių n_2 verčių: $n_2 = (105 \pm 19) \times 10^{-16}$ cm^2/W KRS-5 atveju bei $n_2 = (54 \pm 10) \times 10^{-16}$ cm^2/W KRS-6 atveju. Netiesinio lūžio rodiklio vertės buvo nustatytos pasinaudojant netiesinio energijos pralaidumo matavimais. Taip pat buvo atlikti ilgalaikiai spektro matavimai, kurie parodė itin aukštą superkontinuumo spektro atsikartojamumą KRS-5 kristale. KRS-6 kristale dėl šviesos gijos sukeltų medžiagos modifikacijų, superkontinuumo spektro mėlynasis kraštas laikui bėgant slinkosi į didesniųjų bangos ilgių pusę, tačiau nežymus spektro siaurėjimas buvo pastebėtas tik maždaug po valandos, vadinasi, jo galima paprastai išvengti transliuojant bandinį statmenai spinduliuotės sklidimo krypčiai.

Taip pat buvo atliktas eksperimentinis spalvinių centrų formavimosi įtakos superkontinuumo generacijai NaCl ir KBr kristaluose tyrimas žadinimui naudojant 60 fs trukmės 3,6 μm centrinio bangos ilgio impulsus. Beveik trijų optinių oktavų pločio superkontinuumo spektras buvo užregistruotas bandinius tolygiai transliuojant statmena spinduliuotės sklidimui kryptimi ir taip išvengiant spalvinių centrų formavimosi (1 pav.). Jeigu bandiniai nebuvo judinami, tuomet spalviniai centrai abiejose terpėse pradėjo formuotis per kelias dešimtis sekundžių ir ženkliai susiaurino generuojamo superkontinuumo spektrą bei sumažino energijos pralaidumą. Superkontinuumo spektro siaurėjimas dėl spalvinių centrų formavimosi NaCl kristale buvo pademonstruotas ir pasitelkiant skaitinį modeliavimą, kurio metu buvo taikomas paprastas fenomenologinis modelis, traktuojantis spalvinius centrus kaip priemaišas su 2,7 eV draustinės juostos tarpu, atitinkančiu F-centrų sugerties juostos centrą ties 460 nm.

Toliau buvo pademonstruota kad polidomeninis SBN kristalas yra tinkama netiesinė terpė superkontinuumo generacijai infraraudonojoje srityje. Daugiau nei vienos optinės oktavos pločio superkontinuumo spektrai buvo užregistruoti žadinant itin mažos energijos (dešimčių nanodžaulių) impulsais, kurių centriniai bangos ilgiai pateko į normaliąją (1,2 μm), nulinę (2,0 μm) bei anomaliąją (2,4 μm) SBN grupinių greičių dispersijos sritį.

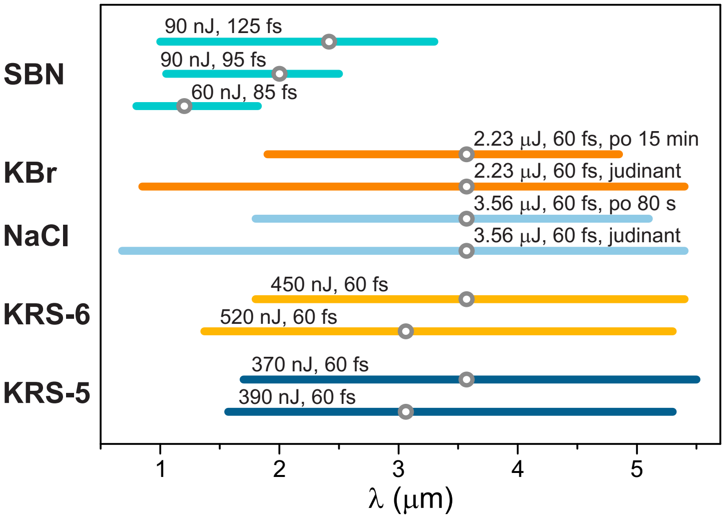

Pav. 1: Tirtose dielektrinėse medžiagose (KRS-5, KRS-6, NaCl, KBr ir SBN) užregistruotų vieno filamento režime gautų superkontinuumo spektrų suvestinė. Pilki tuščiaviduriai apskritimai nurodo žadinančiųjų impulsų bangos ilgį, o komentarai nurodo jų energiją bei trukmę. KRS-5 ir KRS-6 kristalų atveju spektro plotis įvertintas 5×10^{-4}, o kitais atvejais - 10^{-4} intensyvumo lygyje.

Gauti rezultatai leidžia teigti, jog siauro draustinės juostos tarpo dielektrikai, tokie kaip KRS-5, KRS-6 ir SBN gali būti naudojami kaip efektyvios netiesinės terpės superkontinuumo generacijai artimojoje bei viduriniojoje infraraudonojoje spektrinėje srityje. Šarminių metalų halidų kristalai, tokie kaip NaCl ir KBr taip pat yra potencialiai tinkami itin plataus superkontinuumo generacijai šiame spektriniame diapazone, tačiau siekiant išvengti nepageidaujamų spalvinių centrų formavimosi efektų, šie bandiniai superkontinuumo generacijos metu turėtų būti transliuojami statmenai spinduliuotės sklidimo krypčiai.

Toliau buvo vykdomi infraraudonojo superkontinummo generacijos bei šviesos gijų formavimosi tyrimai puslaidininkinėse terpėse. Vienos optinės oktavos pločio superkontinuumo spektras buvo gautas silicio kristale žadinant 4,0 ir 4,7 μm femtosekundiniais impulsais, esant atitinkamai ketvirtosios bei penktosios eilės daugiafotonei sugerčiai. Taip pat buvo parodyta, jog laisvųjų elektronų sugertis nedaro didelės įtakos erdvėlaikinėms šviesos gijų formavimosi savybėms, patvirtinant išvadą [99], jog netiesinis spinduliuotės sklidimas silicyje femtosekundinių impulsų atveju, yra mažiau paveikiamas laisvųjų krūvininkų lyginant su ilgesnės trukmės impulsais.

Dar buvo pademonstruota vientiso, daugiau negu vieną optinę oktavą apimančio superkontinuumo generacija 6H-SiC kristale žadinimui naudojant femtosekundinius impulsus, kurių centriniai bangos ilgiai patenka į normaliąją, nulinę bei anomaliąją terpės GGD sritį. Taip pat atlikus netiesinio energijos pralaidumo matavimus ties 2 μm ir pasinaudojus Marburgerio formule buvo įvertintas 6H-SiC netiesinis lūžio rodiklis. Gauta n_2 vertė ($n_2 = (97 \pm 19) \times 10^{-16}$cm^2/W) paklaidos ribose sutampa su teoriškai apskaičiuota verte ir dera su stebėtomis itin mažomis slenkstinės energijos vertėmis superkontinuumo generacijai.

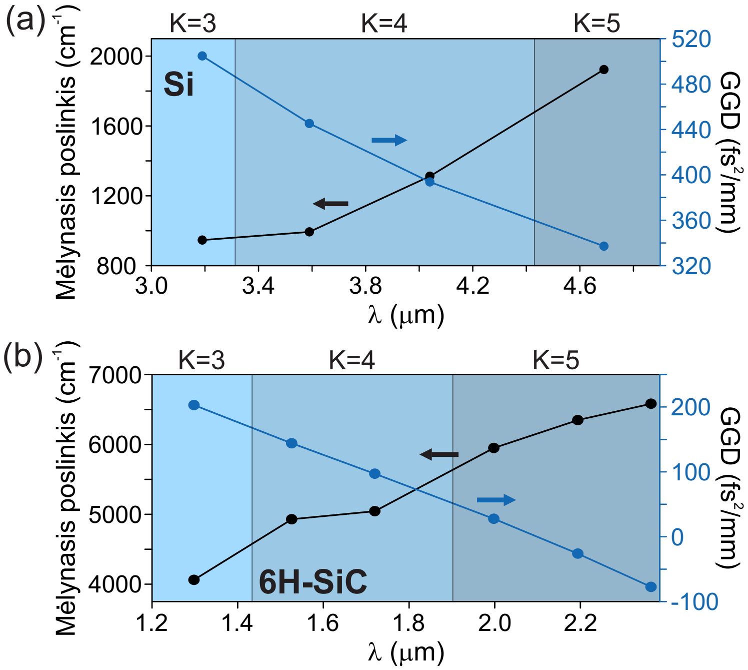

Pav. 2: Superkontinuumo spektro mėlynojo poslinkio ir terpės GGD priklausomybė nuo žadinančiosios spinduliuotės bangos ilgio (a) Si, (b) 6H-SiC atveju. Nuspalvintos zonos ir užrašai virš grafiko nurodo daugiafotonės sugerties eilę toje spektrinėje srityje.

Galiausiai, superkontinuumo generacijos tyrimai silicio bei 6H-SiC kristaluose atskleidė pagrindines šviesos gijų formavimosi nelegiruotuose puslaidininkiuose fizikines savybes. Silicio kristale, normaliosios GGD srityje vykstant šviesos gijų formavimuisi buvo stebimas pradinio impulso skilimas į du subimpulsus. Taip pat silicio bei 6H-SiC spektriniai matavimai atskleidė, jog pagrindiniai superkontinuumo plitimą į mėlynąją pusę nelegiruotuose puslaidininkiuose ribojantys faktoriai yra daugiafotonės sugerties eilė bei terpės grupinių greičių dispersija. Šių dviejų fizikinių efektų įtaka superkontinuumo spektro mėlynajam poslinkiui yra apibendrinta 2 pav.

Apibendrinant, tyrimų metu gauti rezultatai rodo, jog tiek Si, tiek 6H-SiC kristalai yra puikios netiesinės terpės, tinkamos optinės oktavos pločio superkontinuumo generacijai artimojoje bei viduriniojoje infraraudonojoje spektrinėje srityje.

Išvados

1. Siauro draustinės juostos tarpo dielektriniai (KRS-5, KRS-6 ir SBN) bei puslaidininkiniai (silicio ir 6H-SiC) kristalai, pasižymintys dideliu pralaidumu infraraudonojoje spektrinėje srityje bei dideliu kubiniu netiesiškumu, puikiai tinka infraraudonojo superkontinuumo generacijai. Šiose medžiagose žadinimui naudojant artimosios ir viduriniosios infraraudonosios spektrinės srities femtosekundinius impulsus yra generuojamas mažo energijos slenksčio superkontinuumas, kurio spektrinis plotis viršija vieną optinę oktavą.

2. Plačios draustinės juostos dielektriniuose kristaluose NaCl ir KBr žadinimui naudojant femtosekundinius viduriniosios infraraudonosios spektrinės srities impulsus galima kelių optinių oktavų pločio superkontinuumo generacija (0,7-5,4 μm NaCl atveju ir 0,85-5,4 μm KBr atveju, įvertinta 10^{-4} intensyvumo lygyje). Kita vertus, dėl spalvinių centrų, sugeriančių ultravioletinę bei regimąją šviesą, formavimosi, superkontinuumo spektrai pradeda siaurėti (siauresnis diapazonas apima 1,8-5,1 μm NaCl atveju ir 1,9-4,85 μm KBr atveju) ir tampa kokybiškai panašūs į generuojamus siauros draustinės juostos dielektrinėse terpėse.

3. Netiesinio pralaidumo matavimas susidarant šviesos gijai gali būti panaudotas terpės netiesinio lūžio rodiklio nustatymui. Remiantis šiuo metodu buvo įvertintas KRS-5 ($n_2 = (105 \pm 19) \times 10^{-16}$ cm^2/W), KRS-6 ($n_2 = (54 \pm 10) \times 10^{-16}$ cm^2/W) bei 6H-SiC ($n_2 = (97 \pm 19) \times 10^{-16}$ cm^2/W) kristalų netiesinis lūžio rodiklis, o gautos vertės gerai sutapo su apskaičiuotomis.

4. Impulso skilimas į du sub-impulsus, stebėtas erdvėlaikiniuose intensyvumo pasiskirstymuose susidarant šviesos gijoms silicio kristale, patvirtina superkontinuumo generacijos, žadinimo impulsų bangos ilgiams patenkant į terpės normaliosios grupinių greičių dispersijos sritį, mechanizmo universalumą ir faktą, jog laisvųjų krūvininkų įtaka didelio intensyvumo femtosekundinių impulsų sklidimui nelegiruotuose puslaidininkiuose nėra ženkli.

5. Išmatuoti superkontinuumo spektrai, generuoti žadinant įvairių infraraudonosios spektrinės srities bangos ilgių impulsais silicio, 6H-SiC bei SBN kristaluose, pasižymi beveik pastoviu nukirtimo bangos ilgiu ir tolydžiai didėjančiu mėlynuoju poslinkiu didinant žadinimo impulsų centrinį bangos ilgį, iš ko matyti, jog pagrindiniai fizikiniai faktoriai, nulemiantys superkontinuumo spektro plitimą į mėlynąją pusę tiek siauros draustinės juostos dielektrikuose, tiek nelegiruotuose puslaidininkiuose yra terpės grupinių greičių dispersija bei daugiafotonės sugerties eilė.

BIBLIOGRAPHY

[1] A. Dubietis, G. Tamošauskas, R. Šuminas, V.Jukna, A. Couairon, Ultrafast supercontinuum generation in bulk condensed media, Lith. J. Phys. **57**, 133–157 (2017).

[2] R. Fork, C. Shank, C. Hirlimann, R. Yen, W. Tomlinson, Femtosecond white-light continuum pulses, Opt. Lett. **8**(1), 1–3 (1983).

[3] J. H. Marburger, Self-focusing: theory, Progress in Quantum Electron. **4**, 35–110 (1975).

[4] A. Couairon, E. Brambilla, T. Corti, D. Majus, O. d. J. Ramírez-Góngora, M. Kolesik, Practitioner's guide to laser pulse propagation models and simulation, Eur. Phys. J. Spec. Top. **199**(1), 5–76 (2011).

[5] A. Couairon, A. Mysyrowicz, Femtosecond filamentation in transparent media, Phys. Rep. **441**(2-4), 47–189 (2007).

[6] A. Dubietis, E. Gaižauskas, G. Tamošauskas, P. Di Trapani, Light filaments without self-channeling, Phys. Rev. Lett. **92**(25), 253903 (2004).

[7] A. Brodeur, S. Chin, Band-gap dependence of the ultrafast white-light continuum, Phys. Rev. Lett. **80**(20), 4406 (1998).

[8] A. Brodeur, S. Chin, Ultrafast white-light continuum generation and self-focusing in transparent condensed media, J. Opt. Soc. Am. B **16**(4), 637–650 (1999).

[9] M. Sheik-Bahae, D. J. Hagan, E. W. Van Stryland, Dispersion and band-gap scaling of the electronic Kerr effect in solids associated with two-photon absorption, Phys. Rev. Lett. **65**(1), 96 (1990).

[10] M. Kolesik, G. Katona, J. V. Moloney, E. M. Wright, Physical factors limiting the spectral extent and band gap dependence of supercontinuum generation, Phys. Rev. Lett. **91**(4), 043905 (2003).

[11] M. Kolesik, G. Katona, J. Moloney, E. Wright, Theory and simulation of supercontinuum generation in transparent bulk media, Appl. Phys. B **77**(2), 185–195 (2003).

[12] A. L. Gaeta, Spatial and temporal dynamics of collapsing ultrashort laser pulses, Self-focusing: Past and Present 399–411 (2009).

[13] Y. Silberberg, Collapse of optical pulses, Opt. Lett. **15**(22), 1282–1284 (1990).

[14] L. Bergé, S. Skupin, Self-channeling of ultrashort laser pulses in materials with anomalous dispersion, Phys. Rev. E **71**(6), 065601 (2005).

[15] J. Liu, R. Li, Z. Xu, Few-cycle spatiotemporal soliton wave excited by filamentation of a femtosecond laser pulse in materials with anomalous dispersion, Phys. Rev. A **74**(4), 043801 (2006).

[16] S. V. Chekalin, V. O. Kompanets, E. O. Smetanina, V. P. Kandidov, Light bullets and supercontinuum spectrum during femtosecond pulse filamentation under conditions of anomalous group-velocity dispersion in fused silica, Quantum Electron. **43**(4), 326 (2013).

[17] I. Gražulevičiūtė, N. Garejev, D. Majus, V. Jukna, G. Tamošauskas, A. Dubietis, Filamentation and light bullet formation dynamics in solid-state dielectric media with weak, moderate and strong anomalous group velocity dispersion, J. Opt. **18**(2), 025502 (2015).

[18] P. Rigaud, A. Van de Walle, M. Hanna, N. Forget, F. Guichard, Y. Zaouter, K. Guesmi, F. Druon, P. Georges, Supercontinuum-seeded few-cycle mid-infrared OPCPA system, Opt. Express **24**(23), 26494–26502 (2016).

[19] U. Megerle, I. Pugliesi, C. Schriever, C. F. Sailer, E. Riedle, Sub-50 fs broadband absorption spectroscopy with tunable excitation: putting the analysis of ultrafast molecular dynamics on solid ground, Appl. Phys. B **96**(2-3), 215–231 (2009).

[20] G. Auböck, C. Consani, R. Monni, A. Cannizzo, F. Van Mourik, M. Chergui, Femtosecond pump/supercontinuum-probe setup with 20 kHz repetition rate, Rev. Sci. Instrum. **83**(9), 093105 (2012).

[21] A. Krier, *Mid-infrared semiconductor optoelectronics*, volume 118 (Springer, 2007).

[22] A. Schliesser, N. Picqué, T. W. Hänsch, Mid-infrared frequency combs, Nat. Photonics **6**(7), 440–449 (2012).

[23] M. Jahjah, W. Jiang, N. P. Sanchez, W. Ren, P. Patimisco, V. Spagnolo, S. C. Herndon, R. J. Griffin, F. K. Tittel, Atmospheric CH_4 and N_2O measurements near Greater Houston area landfills using a QCL-based QEPAS sensor system during DISCOVER-AQ 2013, Opt. Lett. **39**(4), 957–960 (2014).

[24] M. J. Weber, *Handbook of Opt. Mater.*, volume 19 (CRC press, 2002).

[25] A. Dormidonov, V. Kompanets, S. Chekalin, V. Kandidov, Giantically blue-shifted visible light in femtosecond mid-IR filament in fluorides, Opt. Express **23**(22), 29202–29210 (2015).

[26] A. Marcinkevičiūtė, N. Garejev, R. Šuminas, G. Tamošauskas, A. Dubietis, A compact, self-compression-based sub-3 optical cycle source in the 3-4 μm spectral range, J. Opt. **19**(10), 105505 (2017).

[27] M. Liao, W. Gao, T. Cheng, X. Xue, Z. Duan, D. Deng, H. Kawashima, T. Suzuki, Y. Ohishi, Five-octave-spanning supercontinuum generation in fluoride glass, Appl. Phys. Express **6**(3), 032503 (2013).

[28] M. Liao, W. Gao, T. Cheng, Z. Duan, X. Xue, H. Kawashima, T. Suzuki, Y. Ohishi, Ultrabroad supercontinuum generation through filamentation in tellurite glass, Las. Phys. Lett. **10**(3), 036002 (2013).

[29] P. Béjot, F. Billard, C. Peureux, T. Diard, J. Picot-Clémente, C. Strutynski, P. Mathey, O. Mouawad, O. Faucher, K. Nagasaka, et al., Filamentation-induced spectral broadening and pulse shortening of infrared pulses in Tellurite glass, Opt. Commun. **380**, 245–249 (2016).

[30] Y. Yang, M. Liao, X. Li, W. Bi, Y. Ohishi, T. Cheng, Y. Fang, G. Zhao, W. Gao, Filamentation and supercontinuum generation in lanthanum glass, J. Appl. Phys. **121**(2), 023107 (2017).

[31] Y. Yu, X. Gai, T. Wang, P. Ma, R. Wang, Z. Yang, D.-Y. Choi, S. Madden, B. Luther-Davies, Mid-infrared supercontinuum generation in chalcogenides, Opt. Mater. Express **3**(8), 1075–1086 (2013).

[32] A. Lanin, A. Voronin, E. Stepanov, A. Fedotov, A. Zheltikov, Frequency-tunable sub-two-cycle 60-MW-peak-power free-space waveforms in the mid-infrared, Opt. Lett. **39**(22), 6430–6433 (2014).

[33] S. Ashihara, Y. Kawahara, Spectral broadening of mid-infrared femtosecond pulses in GaAs, Opt. Lett. **34**(24), 3839–3841 (2009).

[34] A. Lanin, A. Voronin, E. Stepanov, A. Fedotov, A. Zheltikov, Multioctave, 3-18 μm sub-two-cycle supercontinua from self-compressing, self-focusing soliton transients in a solid, Opt. Lett. **40**(6), 974–977 (2015).

[35] R. Šuminas, A. Marcinkevičiūtė, G. Tamošauskas, A. Dubietis, Even and odd harmonics-enhanced supercontinuum generation in zinc-blende semiconductors, J. Opt. Soc. Am. B **36**(2), A22–A27 (2019).

[36] G. M. Archipovaite, S. Petit, J.-C. Delagnes, E. Cormier, 100 kHz Yb-fiber laser pumped 3 μm optical parametric amplifier for probing solid-state systems in the strong field regime, Opt. Lett. **42**(5), 891–894 (2017).

[37] R. Šuminas, G. Tamošauskas, G. Valiulis, V. Jukna, A. Couairon, A. Dubietis, Multi-octave spanning nonlinear interactions induced by femtosecond filamentation in polycrystalline ZnSe, Appl. Phys. Lett. **110**(24), 241106 (2017).

[38] M. Bradler, C. Homann, E. Riedle, Broadband difference frequency mixing between visible and near-infrared pulses for few-cycle pulse generation with stable carrier-envelope phase, Appl. Phys. B **113**(1), 19–25 (2013).

[39] H. Pires, M. Baudisch, D. Sanchez, M. Hemmer, J. Biegert, Ultrashort pulse generation in the mid-IR, Prog. Quantum. Electron. **43**, 1–30 (2015).

[40] S. Cussat-Blanc, A. Ivanov, D. Lupinski, E. Freysz, $KTiOPO_4$, $KTiOAsO_4$, and $KNbO_3$ crystals for mid-infrared femtosecond optical parametric amplifiers: analysis and comparison, Appl. Phys. B **70**(1), S247–S252 (2000).

[41] V. Petrov, F. Rotermund, F. Noack, Generation of high-power femtosecond light pulses at 1 kHz in the mid-infrared spectral range between 3 and 12 μm by second-order nonlinear processes in optical crystals, J. Opt. A: Pure and Applied Optics **3**(3), R1 (2001).

[42] J. A. Gruetzmacher, N. F. Scherer, Few-cycle mid-infrared pulse generation, characterization, and coherent propagation in optically dense media, Rev. Sci. Instrum. **73**(6), 2227–2236 (2002).

[43] C. Fecko, J. Loparo, A. Tokmakoff, Generation of 45 femtosecond pulses at 3 μm with a $KNbO_3$ optical parametric amplifier, Opt. Commun. **241**(4-6), 521–528 (2004).

[44] O. Isaienko, E. Borguet, Ultra-broadband sum-frequency vibrational spectrometer of aqueous interfaces based on a non-collinear optical parametric amplifier, Opt. Express **20**(1), 547–561 (2012).

[45] A. Boulesbaa, O. Isaienko, A. Tuladhar, E. Borguet, Generation of sub-30-fs microjoule mid-infrared pulses for ultrafast vibrational dynamics at solid/liquid interfaces, Opt. Lett. **38**(23), 5008–5011 (2013).

[46] M. Bradler, C. Homann, E. Riedle, Mid-IR femtosecond pulse generation on the microjoule level up to 5 μm at high repetition rates, Opt. Lett. **36**(21), 4212–4214 (2011).

[47] D. Brida, C. Manzoni, G. Cirmi, M. Marangoni, S. De Silvestri, G. Cerullo, Generation of broadband mid-infrared pulses from an optical parametric amplifier, Opt. Express **15**(23), 15035–15040 (2007).

[48] D. Brida, M. Marangoni, C. Manzoni, S. De Silvestri, G. Cerullo, Two-optical-cycle pulses in the mid-infrared from an optical parametric amplifier, Opt. Lett. **33**(24), 2901–2903 (2008).

[49] R. A. Kaindl, M. Wurm, K. Reimann, P. Hamm, A. M. Weiner, M. Woerner, Generation, shaping, and characterization of intense femtosecond pulses tunable from 3 to 20 μm, J. Opt. Soc. Am. B **17**(12), 2086–2094 (2000).

[50] J. Darginavičius, G. Tamošauskas, A. Piskarskas, G. Valiulis, A. Dubietis, Generation of tunable few optical-cycle pulses by visible-to-infrared frequency conversion, Appl. Phys. B **108**(1), 1–7 (2012).

[51] J. Darginavičius, N. Garejev, A. Dubietis, Generation of carrier-envelope phase-stable two optical-cycle pulses at 2 μm from a noncollinear beta-barium borate optical parametric amplifier, Opt. Lett. **37**(22), 4805–4807 (2012).

[52] Y. Yin, J. Li, X. Ren, Y. Wang, A. Chew, Z. Chang, High-energy two-cycle pulses at 3.2 μm by a broadband-pumped dual-chirped optical parametric amplification, Opt. Express **24**(22), 24989–24998 (2016).

[53] T. Woike, T. Granzow, U. Dörfler, C. Poetsch, M. Wöhlecke, R. Pankrath, Refractive indices of congruently melting $Sr_{0.61}Ba_{0.39}Nb_2O_6$, Phys. Status Solidi A **186**(1), R13–R15 (2001).

[54] M. Sheik-Bahae, D. C. Hutchings, D. J. Hagan, E. W. Van Stryland, Dispersion of bound electron nonlinear refraction in solids, IEEE J. Quantum Electron. **27**(6), 1296–1309 (1991).

[55] R. DeSalvo, A. A. Said, D. J. Hagan, E. W. Van Stryland, M. Sheik-Bahae, Infrared to ultraviolet measurements of two-photon absorption and n_2 in wide bandgap solids, IEEE J. Quantum Electron. **32**(8), 1324–1333 (1996).

[56] E. D. Palik, *Handbook of Optical Constants of Solids*, volume 3 (Academic press, 1998).

[57] A. Tropf, M. Thomas, W. Tropf, Optical properties of KRS-5, Proc. SPIE **3060**, 344–355 (1997).

[58] J. Leuthold, C. Koos, W. Freude, Nonlinear silicon photonics, Nat. Photonics **4**(8), 535–544 (2010).

[59] S. Wang, M. Zhan, G. Wang, H. Xuan, W. Zhang, C. Liu, C. Xu, Y. Liu, Z. Wei, X. Chen, 4H-SiC: a new nonlinear material for midinfrared lasers, Laser Photonics Rev. **7**(5), 831–838 (2013).

[60] X. Gai, Y. Yu, B. Kuyken, P. Ma, S. J. Madden, J. Van Campenhout, P. Verheyen, G. Roelkens, R. Baets, B. Luther-Davies, Nonlinear absorption and refraction in crystalline silicon in the mid-infrared, Laser Photonics Rev. **7**(6), 1054–1064 (2013).

[61] J. Cardenas, M. Yu, Y. Okawachi, C. B. Poitras, R. K. Lau, A. Dutt, A. L. Gaeta, M. Lipson, Optical nonlinearities in high-confinement silicon carbide waveguides, Opt. Lett. **40**(17), 4138–4141 (2015).

[62] G. Hettner, G. Leisegang, Dispersion of the mixed crystals TlBr-TlI (KRS-5) and TlCl-TlBr (KRS-6) in the infrared, Optik **3**, 305–314 (1948).

[63] K. Takahei, K. Kobayashi, Reflectivity spectra of TlCl-TlBr mixed crystals, J. Phys. Soc. Jpn. **43**(3), 891–898 (1977).

[64] F. Silva, D. Austin, A. Thai, M. Baudisch, M. Hemmer, D. Faccio, A. Couairon, J. Biegert, Multi-octave supercontinuum generation from mid-infrared filamentation in a bulk crystal, Nat. Commun. **3**(1), 807 (2012).

[65] J. Darginavičius, D. Majus, V. Jukna, N. Garejev, G. Valiulis, A. Couairon, A. Dubietis, Ultrabroadband supercontinuum and third-harmonic generation in bulk solids with two optical-cycle carrier-envelope phase-stable pulses at 2 μm, Opt. Express **21**(21), 25210–25220 (2013).

[66] J. A. Dharmadhikari, R. A. Deshpande, A. Nath, K. Dota, D. Mathur, A. K. Dharmadhikari, Effect of group velocity dispersion on supercontinuum generation and filamentation in transparent solids, Appl. Phys. B **117**(1), 471–479 (2014).

[67] H. Liang, P. Krogen, R. Grynko, O. Novak, C.-L. Chang, G. J. Stein, D. Weerawarne, B. Shim, F. X. Kärtner, K.-H. Hong, Three-octave-spanning supercontinuum generation and sub-two-cycle self-compression of mid-infrared filaments in dielectrics, Opt. Lett. **40**(6), 1069–1072 (2015).

[68] H. Fattahi, H. Wang, A. Alismail, G. Arisholm, V. Pervak, A. M. Azzeer, F. Krausz, Near-PHz-bandwidth, phase-stable continua generated from a Yb:YAG thin-disk amplifier, Opt. Express **24**(21), 24337–24346 (2016).

[69] N. Garejev, G. Tamošauskas, A. Dubietis, Comparative study of multi-octave supercontinuum generation in fused silica, YAG, and LiF in the range of anomalous group velocity dispersion, J. Opt. Soc. Am. B **34**(1), 88–94 (2017).

[70] R. Šuminas, G. Tamošauskas, G. Valiulis, A. Dubietis, Spatiotemporal light bullets and supercontinuum generation in β-BBO crystal with competing quadratic and cubic nonlinearities, Opt. Lett. **41**(9), 2097–2100 (2016).

[71] H. Wang, A. Alismail, G. Barbiero, M. Wendl, H. Fattahi, Cross-polarized, multi-octave supercontinuum generation, Opt. Lett. **42**(13), 2595–2598 (2017).

[72] S. Frolov, V. Trunov, V. Leshchenko, E. Pestryakov, Multi-octave supercontinuum generation with IR radiation filamentation in transparent solid-state media, Appl. Phys. B **122**(5), 124 (2016).

[73] Y. Yang, W. Bi, X. Li, M. Liao, W. Gao, Y. Ohishi, Y. Fang, Y. Li, Ultrabroadband supercontinuum generation through filamentation in a lead fluoride crystal, J. Opt. Soc. Am. B **36**(2), A1–A7 (2019).

[74] H. Minato, Y. Ishido, Development of an infrared absorption measurement method using the photothermal deflection effect of thallium bromide iodide (KRS-5): Measurement with a stepped-scan Fourier transform infrared spectrometer, Rev. Sci. Instrum. **72**(7), 2889–2892 (2001).

[75] H. Kim, A. Churilov, G. Ciampi, L. Cirignano, W. Higgins, S. Kim, P. O'Dougherty, F. Olschner, K. Shah, Continued development of thallium bromide and related compounds for gamma-ray spectrometers, Nucl. Instrum. Meth. A **629**(1), 192–196 (2011).

[76] J. T. Rayner, Evaluation of a solid KRS-5 grism for infrared astronomy, in *Proc. SPIE* (International Society for Optics and Photonics, 1998), volume 3354, 289–294.

[77] N. Bowles, M. Tecza, J. Barstow, J. Temple, P. Irwin, L. Fletcher, S. Calcutt, J. Hurley, M. Ferlet, D. Freeman, The long wave (11-16 μm) spectrograph for the EChO M3 Mission Candidate study, Exp. Astron. **40**(2-3), 801–811 (2015).

[78] S. Mantsevich, Thallium bromide iodide crystal acoustic anisotropy examination, Ultrasonics **75**, 91–97 (2017).

[79] V. B. Voloshinov, D. L. Porokhovnichenko, E. A. Dyakonov, Optimization of acousto-optic interaction geometry in KRS-5 crystal for far-infrared applications, Opt. Eng. **56**(8), 087102 (2017).

[80] M. Baudrier-Raybaut, R. Haidar, P. Kupecek, P. Lemasson, E. Rosencher, Random quasi-phase-matching in bulk polycrystalline isotropic nonlinear materials, Nature **432**(7015), 374–376 (2004).

[81] R. Adair, L. Chase, S. A. Payne, Nonlinear refractive index of optical crystals, Phys. Rev. B **39**(5), 3337 (1989).

[82] A. Dubietis, G. Tamosauskas, G. Fibich, B. Ilan, Multiple filamentation induced by input-beam ellipticity, Opt. Lett. **29**(10), 1126–1128 (2004).

[83] A. Jarnac, G. Tamosauskas, D. Majus, A. Houard, A. Mysyrowicz, A. Couairon, A. Dubietis, Whole life cycle of femtosecond ultraviolet filaments in water, Phys. Rev. A **89**(3), 033809 (2014).

[84] J. Kohl-Landgraf, J.-E. Nimsch, J. Wachtveitl, LiF, an underestimated supercontinuum source in femtosecond transient absorption spectroscopy, Opt. Express **21**(14), 17060–17065 (2013).

[85] A. V. Kuznetsov, V. O. Kompanets, A. E. Dormidonov, S. V. Chekalin, S. A. Shlenov, V. P. Kandidov, Periodic colour-centre structure formed under filamentation of mid-IR femtosecond laser radiation in a LiF crystal, Quantum Electron. **46**(4), 379 (2016).

[86] S. V. Chekalin, V. O. Kompanets, A. E. Dormidonov, V. P. Kandidov, Influence of induced colour centres on the frequency–angular spectrum of a light bullet of mid-IR radiation in lithium fluoride, Quantum Electron. **47**(3), 259 (2017).

[87] S. V. Chekalin, V. O. Kompanets, A. E. Dormidonov, V. P. Kandidov, Path length and spectrum of single-cycle mid-IR light bullets in transparent dielectrics, Quantum Electron. **48**(4), 372 (2018).

[88] S. Orlando, S. Langford, J. Dickinson, Generation of color centers in alkali halide single crystals using ultrafast laser pulses, J. Optoelecton. Adv. Mat. **12**, 707–710 (2010).

[89] J. Dickinson, S. Orlando, S. Avanesyan, S. Langford, Color center formation in soda lime glass and NaCl single crystals with femtosecond laser pulses, Appl. Phys. A **79**(4-6), 859–864 (2004).

[90] J. Dickinson, S. Langford, S. Avanesyan, S. Orlando, Color center formation in KCl and KBr single crystals with femtosecond laser pulses, Appl. Surf. Sci. **253**(19), 7874–7878 (2007).

[91] I. Dicaire, V. Jukna, C. Praz, C. Milián, L. Summerer, A. Couairon, Spaceborne laser filamentation for atmospheric remote sensing, Laser Photonics Rev. **10**(3), 481–493 (2016).

[92] K. Terabe, S. Takekawa, M. Nakamura, K. Kitamura, S. Higuchi, Y. Gotoh, A. Gruverman, Imaging and engineering the nanoscale-domain structure of a $Sr_{0.61}Ba_{0.39}Nb_2O_6$ crystal using a scanning force microscope, Appl. Phys. Lett. **81**(11), 2044–2046 (2002).

[93] P. Molina, M. d. l. O. Ramirez, L. E. Bausa, Strontium barium niobate as a multifunctional two-dimensional nonlinear “photonic glass”, Adv. Funct. Mater. **18**(5), 709–715 (2008).

[94] V. Jukna, N. Garejev, G. Tamošauskas, A. Dubietis, Role of external focusing geometry in supercontinuum generation in bulk solid-state media, J. Opt. Soc. Am. B **36**(2), A54–A60 (2019).

[95] P. Corkum, P. Ho, R. Alfano, J. Manassah, Generation of infrared supercontinuum covering 3-14 μm in dielectrics and semiconductors, Opt. Lett. **10**(12), 624–626 (1985).

[96] E. Stepanov, A. Lanin, A. Voronin, A. Fedotov, A. Zheltikov, Solid-state source of subcycle pulses in the midinfrared, Phys. Rev. Lett. **117**(4), 043901 (2016).

[97] M. Durand, A. Houard, K. Lim, A. Durécu, O. Vasseur, M. Richardson, Study of filamentation threshold in zinc selenide, Opt. Express **22**(5), 5852–5858 (2014).

[98] O. Mouawad, P. Béjot, F. Billard, P. Mathey, B. Kibler, F. Désévédavy, G. Gadret, J.-C. Jules, O. Faucher, F. Smektala, Filament-induced visible-to-mid-IR supercontinuum in a ZnSe crystal: Towards multi-octave supercontinuum absorption spectroscopy, Opt. Mater. **60**, 355–358 (2016).

[99] R. I. Grynko, G. C. Nagar, B. Shim, Wavelength-scaled laser filamentation in solids and plasma-assisted subcycle light-bullet generation in the long-wavelength infrared, Phys. Rev. A **98**(2), 023844 (2018).

[100] G. L. DesAutels, C. Brewer, M. Walker, S. Juhl, M. Finet, S. Ristich, M. Whitaker, P. Powers, Femtosecond laser damage threshold and nonlinear characterization in bulk transparent SiC materials, J. Opt. Soc. Am. B **25**(1), 60–66 (2008).

[101] T. Wang, N. Venkatram, J. Gosciniak, Y. Cui, G. Qian, W. Ji, D. T. Tan, Multi-photon absorption and third-order nonlinearity in silicon at mid-infrared wavelengths, Opt. Express **21**(26), 32192–32198 (2013).

[102] M. Borghi, C. Castellan, S. Signorini, A. Trenti, L. Pavesi, Nonlinear silicon photonics, J. Opt. **19**(9), 093002 (2017).

[103] Y. Zou, S. Chakravarty, C.-J. Chung, X. Xu, R. T. Chen, Mid-infrared silicon photonic waveguides and devices, Photonics Res. **6**(4), 254–276 (2018).

[104] R. K. Lau, M. R. Lamont, A. G. Griffith, Y. Okawachi, M. Lipson, A. L. Gaeta, Octave-spanning mid-infrared supercontinuum generation in silicon nanowaveguides, Opt. Lett. **39**(15), 4518–4521 (2014).

[105] B. Kuyken, T. Ideguchi, S. Holzner, M. Yan, T. W. Hänsch, J. Van Campenhout, P. Verheyen, S. Coen, F. Leo, R. Baets, et al., An octave-spanning mid-infrared frequency comb generated in a silicon nanophotonic wire waveguide, Nat. Commun. **6**(1), 6310 (2015).

[106] N. Singh, D. D. Hudson, Y. Yu, C. Grillet, S. D. Jackson, A. Casas-Bedoya, A. Read, P. Atanackovic, S. G. Duvall, S. Palomba, et al., Mid-infrared supercontinuum generation from 2 to 6 μm in a silicon nanowire, Optica **2**(9), 797–802 (2015).

[107] A. Blanco-Redondo, C. Husko, D. Eades, Y. Zhang, J. Li, T. Krauss, B. Eggleton, Observation of soliton compression in silicon photonic crystals, Nat. Commun. **5**(1), 3160 (2014).

[108] V. V. Kononenko, V. V. Konov, E. M. Dianov, Delocalization of femtosecond radiation in silicon, Opt. Lett. **37**(16), 3369–3371 (2012).

[109] A. Mouskeftaras, A. V. Rode, R. Clady, M. Sentis, O. Utéza, D. Grojo, Self-limited underdense microplasmas in bulk silicon induced by ultrashort laser pulses, Appl. Phys. Lett. **105**(19), 191103 (2014).

[110] E. Zavedeev, V. Kononenko, V. Konov, Delocalization of femtosecond laser radiation in crystalline Si in the mid-IR range, Laser Phys. **26**(1), 016101 (2015).

[111] A. Mouskeftaras, M. Chanal, M. Chambonneau, R. Clady, O. Utéza, D. Grojo, Direct measurement of ambipolar diffusion in bulk silicon by ultrafast infrared imaging of laser-induced microplasmas, Appl. Phys. Lett. **108**(4), 041107 (2016).

[112] M. Chanal, V. Y. Fedorov, M. Chambonneau, R. Clady, S. Tzortzakis, D. Grojo, Crossing the threshold of ultrafast laser writing in bulk silicon, Nat. Commun. **8**(1), 1–6 (2017).

[113] H. Sato, M. Abe, I. Shoji, J. Suda, T. Kondo, Accurate measurements of second-order nonlinear optical coefficients of 6H and 4H silicon carbide, J. Opt. Soc. Am. B **26**(10), 1892–1896 (2009).

[114] F. De Leonardis, R. A. Soref, V. M. Passaro, Dispersion of nonresonant third-order nonlinearities in Silicon Carbide, Sci. Rep. **7**, 40924 (2017).

[115] M. A. Guidry, K. Y. Yang, D. M. Lukin, A. Markosyan, J. Yang, M. M. Fejer, J. Vučković, Optical parametric oscillation in silicon carbide nanophotonics, Optica **7**, 1139–1142 (2020).

[116] H.-T. Fan, C.-H. Xu, Z.-H. Wang, G. Wang, C.-J. Liu, J.-K. Liang, X.-L. Chen, Z.-Y. Wei, Generation of broadband 17-μJ mid-infrared femtosecond pulses at 3.75 μm by silicon carbide crystal, Opt. Lett. **39**(21), 6249–6252 (2014).

[117] E. Yablonovitch, N. Bloembergen, Avalanche ionization and the limiting diameter of filaments induced by light pulses in transparent media, Phys. Rev. Lett. **29**(14), 907 (1972).

[118] S. Xu, J. Qiu, T. Jia, C. Li, H. Sun, Z. Xu, Femtosecond laser ablation of crystals SiO_2 and YAG, Opt. Commun. **274**(1), 163–166 (2007).

[119] M. Durand, A. Jarnac, A. Houard, Y. Liu, S. Grabielle, N. Forget, A. Durécu, A. Couairon, A. Mysyrowicz, Self-guided propagation of ultrashort laser pulses in the anomalous dispersion region of transparent solids: a new regime of filamentation, Phys. Rev. Lett. **110**(11), 115003 (2013).

[120] S. Chekalin, A. Dormidonov, V. Kompanets, E. Zaloznaya, V. Kandidov, Light bullet supercontinuum, J. Opt. Soc. Am. B **36**(2), A43–A53 (2019).

CURRICULUM VITAE

Name: Agnė

Surname: Šuminienė

Date of birth: 1992-02-19

Place of birth: Vilnius, Lithuania

E-mail: agne.suminiene@gmail.com

Education:

2003–2011	Vilnius Gabijos gymnasium
2011–2015	Vilnius University, Faculty of Physics *Bachelor degree, Cum Laude.*
2015–2017	Vilnius University, Faculty of Physics *Master degree, Magna Cum Laude.*
2017–2021	Vilnius University, Faculty of Physics, *Ph.D. studies.*

Work experience:

2012–2016	Laboratory assistant at Vilnius University
2018–2020	Junior researcher at Vilnius University
2020	Laser technician at Light Conversion
2021–present	Laser engineer at Light Conversion

TRUMPOS ŽINIOS APIE AUTORĘ

Vardas:	Agnė
Pavardė:	Šuminienė
Gimimo data:	1992-02-19
Gimimo vieta:	Vilnius, Lietuva
El. paštas:	agne.suminiene@gmail.com

Išsilavinimas:

2003–2011	Vilniaus Gabijos gimnazija
2011–2015	Vilniaus universitetas, Fizikos fakultetas *Bakalauro kvalifikacinis laipsnis, Cum Laude.*
2015–2017	Vilniaus universitetas, Fizikos fakultetas *Magistro kvalifikacinis laipsnis, Magna Cum Laude.*
2017–2021	Vilniaus universitetas, Fizikos fakultetas, *Doktorantūra.*

Profesinė veikla:

2012–2016	Laborantė, Vilniaus universitetas
2018–2020	Jaunesnioji mokslo darbuotoja, Vilniaus universitetas
2020	Lazerių technikė, Light Conversion
2021–dabar	Lazerių inžinierė, Light Conversion

ACKNOWLEDGEMENTS

> Mischief Managed.
>
> J.K. Rowling, Harry Potter and
> the Prisoner of Azkaban

Firstly, I would like to thank my academic supervisor prof. habil. dr. Audrius Dubietis for the invitation to join his research group and to do my doctoral thesis under his supervision. His experience and guidance were invaluable in the whole process of preparing this thesis.

Secondly, I am very grateful for all the help I received from assoc. prof. dr. Gintaras Tamošauskas and dr. Vytautas Jukna. Gintaras provided much help with the labwork, kept the laser sources and the measuring equipment alive and shared technical insight which aided in performing good quality experiments efficiently. In addition, Vytautas with his modelling skills and deep knowledge of the underlying physics of the studied processes was a huge help in understanding the experimental results and making sense of the measured data.

Thirdly, I would like to express my gratitude to my research group colleagues. I thank my husband dr. Rosvaldas Šuminas who worked together with me on most of my experiments. His strong sense of logic and reason together with tremendous problem-solving skills has helped me greatly in the lab and is helping me in life everyday. I am grateful to dr. Nail Garejev for all the code which made the measurements and data processing so much easier, for the template of this thesis which he kindly shared and also for the photographs he has taken of the studied samples and of me throughout the years working together.

Also, I want to thank my bachelor supervisor prof. habil. dr. Valdas Sirutkaitis for all the kindness and care he has provided through all the years I worked at Laser Research Center. In addition, I thank my former supervisor assoc. prof. dr. Rytis Butkus for all the different interesting projects that helped me expand my knowledge of nonlinear optics.

And last but not least, I am grateful to my friends and colleagues Ph. D. student Balys Momgaudis, master's student Jurgita Strakšytė, dr. Julius Vengelis and dr. Mikas Vengris for all the fun times we had during lunch and coffee breaks at Laser Research Center.

COPIES OF PUBLICATIONS

[A1] **A. Marcinkevičiūtė**, N. Garejev, R. Šuminas, G. Tamošauskas, A. Dubietis, A compact, self-compression-based sub-3 optical cycle source in the 3-4 μm spectral range, J. Opt. **19**, 105505 (2017).

[A2] **A. Marcinkevičiūtė**, G. Tamošauskas, A. Dubietis, Supercontinuum generation in mixed thallous halides KRS-5 and KRS-6, Opt. Mater. **78**, 339–344 (2018).

[A3] **A. Marcinkevičiūtė**, V. Jukna, R. Šuminas, N. Garejev, G. Tamošauskas, A. Dubietis, Supercontinuum generation in the absence and in the presence of color centers in NaCl and KBr, Results Phys. **14**, 102396 (2019).

[A4] R. Šuminas, N. Garejev, **A. Šuminienė**, V. Jukna, G. Tamošauskas, A. Dubietis, Femtosecond filamentation, supercontinuum generation, and determination of n_2 in polycrystalline SBN, J. Opt. Soc. Am. B **37**(4), 1530–1534 (2020).

[A5] **A. Marcinkevičiūtė**, V. Jukna, R. Šuminas, N. Garejev, G. Tamošauskas, A. Dubietis, Femtosecond filamentation and supercontinuum generation in bulk silicon, Opt. Lett. **44**(6), 1343–1346 (2019).

[A6] **A. Šuminienė**, V. Jukna, R. Šuminas, G. Tamošauskas, A. Dubietis, Femtosecond infrared supercontinuum generation in 6H-SiC, OSA Continuum **4**(3), 911–917 (2021).

A1

A COMPACT, SELF-COMPRESSION-BASED SUB-3 OPTICAL CYCLE SOURCE IN THE 3-4 μM SPECTRAL RANGE

A. Marcinkevičiūtė, N. Garejev, R. Šuminas, G. Tamošauskas, A. Dubietis

J. Opt. **19**, 105505 (2017)

Reprinted with permission from Journal of Optics

A compact, self-compression-based sub-3 optical cycle source in the $3-4$ μm spectral range

Agnė Marcinkevičiūtė, Nail Garejev, Rosvaldas Šuminas, Gintaras Tamošauskas, Audrius Dubietis

Department of Quantum Electronics, Vilnius University, Saulėtekio Avenue 10, LT-10223 Vilnius, Lithuania

Abstract.

We report on the experimental realization of a compact, Ti:sapphire laser-pumped mid-infrared light source, which delivers sub-3 optical cycle pulses in the $3-4$ μm spectral range. The light source employs difference frequency generation in KTA crystal by mixing the signal and idler waves from a commercial near-infrared optical parametric amplifier and subsequent optical parametric amplification in $LiIO_3$ crystal. The amplified sub-100 fs mid-infrared pulses are self-compressed down to sub-3 optical cycles by nonlinear propagation in few mm-thick YAG, CaF_2 and BaF_2 crystals featuring anomalous group velocity dispersion in that spectral range. The self-compression is performed without the onset of self-focusing effects, hence maintaining a homogenous beam profile with energy throughput efficiency of above 90%, yielding the self-compressed pulses with sub-30 μJ energy. Even larger self-compression factors (down to sub-2 optical cycles) were achieved in the filamentation regime, simultaneously producing an ultrabroadband supercontinuum, extending from the visible to the mid-infrared.

PACS numbers: 42.65.Jx, 42.65.Re, 42.65.Yj

Keywords: optical parametric amplification, difference frequency generation, pulse compression, supercontinuum generation Submitted to: *J. Opt.*

1. Introduction

Development of laser sources, which emit ultrashort pulses in the mid-infrared spectral range is dictated by the emerging applications in ultrafast vibrational spectroscopy, mid-infrared nonlinear optics and strong-field physics [1]. Generation of mid-infrared pulses with durations as short as few optical cycles is exclusively based on the optical parametric amplification, which supports large amplification bandwidths necessary to maintain short pulse widths, see e.g. [2].

Technically simple, low cost and easily implementable setups for generation of ultrashort mid-infrared pulses rely on using widely spread amplified femtosecond Ti:sapphire driving lasers. Several configurations that involve optical parametric amplification, difference frequency generation, or both, have been demonstrated so far. The first configuration is based on either collinear or noncollinear optical parametric amplification in bulk and periodically poled nonlinear crystals, extracting the idler wave, which lies in the mid-infrared spectral range. Here the fundamental laser wavelength (800 nm) serves as a pump, while the seed signal is provided by either supercontinuum generation in bulk dielectric media or using the idler pulses produced by the near-infrared optical parametric amplifier (OPA). To this end, optical parametric amplifiers based on nonlinear crystals which possess transparency and phase matching in the mid-infrared, such as potassium titanyl phosphate (KTP) and potassium titanyl arsenate (KTA) [3, 4], potassium niobate ($KNbO_3$) [3–8], lithium niobate ($LiNbO_3$) [4, 7–9], lithium iodate ($LiIO_3$) [10] and periodically poled stoichiometric lithium tantalate (PPSLT) [11] crystals were demonstrated to provide pulses with durations from sub-100 fs to few optical cycles in the $2-5$ μm wavelength range. The second configuration makes use of difference frequency generation (DFG) between the signal and idler pulses from the near-infrared optical parametric amplifier (e.g. that based on commonly used BBO crystal), see e.g. [12]. The third configuration employs DFG between broadband pulses from second harmonic pumped noncollinear optical parametric amplifier and the fundamental laser pulses, providing few optical cycle pulses with stable carrier envelope phase, which are subsequently amplified in a broadband OPA [13–15].

Nonlinear propagation of intense mid-infrared pulses in wide bandgap solid-state dielectric materials featuring anomalous group velocity dispersion (GVD) provides an efficient pulse self-compression mechanism, resulting from the interplay between the self-phase modulation and anomalous GVD, that could be readily employed to broaden the pulse spectrum beyond the OPA gain bandwidth and further shorten the pulse duration. The numerical simulations suggest that self-focusing and filamentation of femtosecond mid-infrared pulses in dielectrics may lead to pulse self-compression down to a single optical cycle [16]. Moreover, such filamentation regime leads to formation of self-compressed quasistationary spatiotemporal light bullets, as verified experimentally in various dielectric materials, such as fused silica [17–19], sapphire [20], CaF_2 and BaF_2 [21] and BBO [22], yielding the shortest self-compressed pulsewidths of just sub-two optical cycles for the input wavelengths around 2 μm.

However, fully evolved self-compressed light bullets contain just a relatively small fraction of the input pulse energy and exhibit dispersive broadening as they leave the nonlinear medium and propagate in the free space [20], and these features may appear undesirable for a range of practical applications. Therefore a more attractive realization of anomalous GVD-induced self-compression mechanism relies upon using a shorter nonlinear medium and a larger input beam, extracting the self-compressed pulse before the filamentation regime sets in [23]. Such self-compression mechanism appears universal and is demonstrated to work equally well with mid-infrared optical parametric chirped pulse amplification (OPCPA) systems providing tens-of-μJ pulses at high repetition rate [24] and multimilijoule pulses with multigagawatt peak power [25], by compressing the output pulses to sub-3 optical cycles in few mm-thick YAG crystal.

In this work, we demonstrate a simple and compact Ti:sapphire laser-pumped mid-infrared light source, which involves DFG between the signal and idler pulses from a commercial near infrared OPA, subsequent optical parametric amplification in $LiIO_3$ crystal and self-compression by the nonlinear propagation in dielectric crystals featuring anomalous GVD, and which delivers sub-3 optical cycle pulses with sub-30 μJ energy in the $3-4$ μm spectral range.

2. Results and discussion

The experimental scheme is depicted in figure 1(a). The entire setup is driven by regeneratively amplified Ti:sapphire system (Spitfire PRO, Newport-Spectra Physics), which delivers 100 fs pulses at 800 nm with an energy up to 3 mJ at a repetition rate of 1 kHz. A fraction of the laser energy (0.9 mJ) was used to pump a commercial BBO crystal-based OPA (Topas-C, Light Conversion Ltd.), which provided the near-infrared signal at 1.30 μm and idler at 2.08 μm pulses, with energies of 175 μJ and 115 μJ, and pulsewidths of 75 fs and 85 fs, respectively.

The difference frequency generation between the *o*-polarized signal and *e*-polarized idler pulses was performed in a 1 mm-thick KTA crystal, cut for type

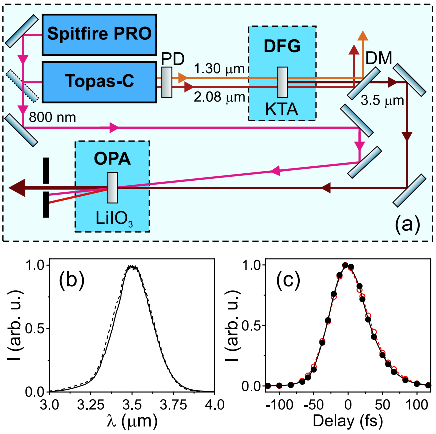

Figure 1. (a) Layout of the experimental setup. PD, predelay; DFG, difference frequency generator; DM, dichroic mirror; OPA, optical parametric amplifier. (b) Spectra and (c) cross-correlation functions of 60 fs pulse at 3.5 μm after DFG (dashed curve, open circles) and OPA (solid curve, full circles) stages.

II phase matching ($\theta = 43°$, $\phi = 0°$), which provides broad conversion bandwidth in the wavelength range of interest [26]. Proper timing between the input signal and idler pulses entering the DFG crystal was set by inserting a 1 mm-thick BBO crystal (PD), oriented out of phase matching, hence compensating their temporal walk-off originating in BBO OPA. The DFG stage delivered *o*-polarized 60 fs pulse with a central wavelength of 3.5 μm and with a FWHM spectral width of 280 nm and an energy of 11 μJ, as shown by dashed curves in figures 1(b) and (c). Here the spectra were measured using a home-built scanning prism spectrometer with PbSe detector, whereas the cross-correlation measurements were performed by the sum-frequency generation in a thin (20 μm thickness) BBO crystal using 30 fs, 720 nm reference pulse from a second harmonic-pumped noncollinear OPA (Topas-White, Light Conversion Ltd.). The difference frequency pulse was almost perfectly transform-limited, as verified by the zero-phase Fourier transform of the spectrum.

Thereafter the difference frequency pulse at 3.5 μm was amplified in LiIO$_3$ OPA, which was pumped by the *e*-polarized fundamental laser pulse at 800 nm. As an OPA we used 1 mm-thick LiIO$_3$ crystal cut for type I phase matching ($\theta = 21°$), which provides naturally broad amplification bandwidth due to intrinsically small group velocity mismatch between the *o*-polarized signal (at 3.5 μm) and *e*-polarized idler (at 1.04 μm) waves [10, 13]. The pump and injected signal beams were crossed at a very slight angle (0.7°), so as to easily separate the pump, amplified signal and idler beams without introducing additional optical elements. With the pump pulse energy of 0.7 mJ (the pump beam FWHM diameter of 1.6 mm, the estimated pump intensity was 200 GW/cm^2), the 3.5 μm pulse was amplified up to 35 μJ energy, simultaneously producing the idler pulse at 1.04 μm with an energy of 100 μJ, with the quantum efficiency of the OPA of 18%. Relatively low conversion efficiency of the OPA is due to relatively short crystal length, that was chosen to be shorter than the walk-off length between 800 nm and 3.5 μm pulses (the group velocity mismatch between these two is 54 fs/mm). On the other hand, the choice of the crystal length guaranteed that the OPA did not introduce any noticeable distortions as seen from a comparison of spectra and cross-correlation functions of the 3.5 μm pulse after DFG and OPA stages, presented in figures 1(b) and (c). No optical damage or degradation of the crystal was observed with the above parameters of the pump, as verified by stable and robust day-long operation of the OPA.

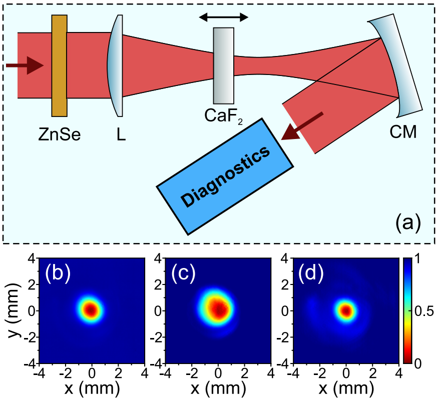

Figure 2. (a) Layout of the self-compression setup. L, focusing lens; CM, concave mirror. (b) The input beam profile before the focusing lens. The output beam profiles after the collimating mirror, in the cases of: (c) lossless self-compression ($z = -6.5$ mm), (d) filamentation ($z = -1$ mm).

The amplified 3.5 μm pulse was self-compressed by the nonlinear propagation in 4 mm-thick CaF$_2$ plate. In doing so, the OPA output beam of 1.3 mm FWHM diameter was focused by plano-convex BaF$_2$ lens (L) with a focal length of 100 mm onto CaF$_2$ plate, which was mounted on a translation stage and made movable along the beam propagation path, so allowing fine adjustment of the input beam diameter and intensity, as depicted in figure 2(a). 3 mm-thick anti-reflection coated ZnSe plate was placed before the focusing lens so as to approximately compensate for the group velocity dispersion introduced by BaF_2 lens of 3.5 mm thickness. The outgoing beam was then collimated by Ag-coated concave mirror (CM) with the curvature radius of 200 mm and directed to the measurement apparatus for characterization of the temporal and spatial profiles, spectrum and energy transmission. The temporal intensity profile of the self-compressed pulse was characterized by means of sum-frequency generation-based frequency-resolved optical gating (SFG-FROG), the beam profile was measured with the pyroelectric CCD camera (WinCamD, model FIR2-16-HR), and the transmitted energy was measured using the energy meter (Ophir) with a pyroelectric detector (PE9-SH).

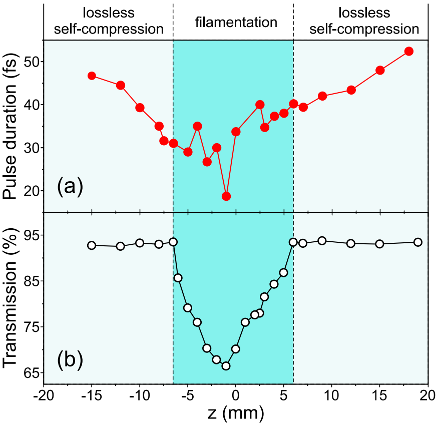

Figure 3. (a) Pulse duration and (b) energy transmission as functions of CaF_2 plate position z with respect to the geometric focus ($z = 0$ mm).

The energy of the pulse at the input face of CaF_2 plate was 29 μJ, as measured after beam steering mirrors (not shown), ZnSe plate and focusing lens. Figure 3 shows the retrieved pulsewidth and the transmission of CaF_2 plate as functions of the sample position z with respect to the geometric focus ($z = 0$ mm). Two distinct regimes of self-compression were uncovered, which were distinguished by the absence or presence of the nonlinear losses. A lossless self-compression regime (with energy throughput efficiency of 93.5% and the energy losses occurring just due to Fresnel reflections from the input and output faces of CaF_2 plate) was found for converging ($z < 0$) as well as for diverging ($z > 0$) input beams, when CaF_2 plate was located several mm on both sides from the geometric focus.

Figure 4 shows the measured and retrieved SFG-FROG traces, and compares the spectra and intensity profiles of the input and self-compressed pulses at $z = -6.5$ mm, just before the onset of beam filamentation. The duration of the self-compressed pulse of 31 fs is equivalent to 2.7 optical cycles and was retrieved within grid size of 128×128 pixels and a reconstruction error of 0.7%. Lossless self-compression yielded a homogenous Gaussian-shaped beam profile of the self-compressed pulse, as shown in figure 2(c), attesting essentially one-dimensional dynamics of the nonlinear propagation [27, 28], where self-compression of the pulse stems from the sole interplay between the self-phase modulation and anomalous GVD, without the onset of any other nonlinear effects, such as self-focusing, nonlinear absorption and generation of free electron plasma. The measured short-term (over 5 min interval) energy root-mean-square (rms) fluctuations of the self-compressed pulse were 1.7%. Very similar self-compression dynamics, although yielding slightly longer self-compressed pulse, was also measured for diverging input beam, as the CaF_2 plate was moved further out of the geometric focus.

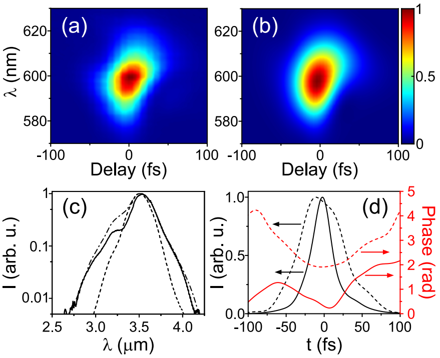

Figure 4. Lossless self-compression of 60 fs, 3.5 μm pulses down to 31 fs in 4 mm-thick CaF_2 plate located at $z = -6.5$ mm: (a) measured and (b) retrieved SFG-FROG traces, (c) spectrum and (d) retrieved intensity profile and phase of the self-compressed pulse. Dash-dotted curve in (c) shows the retrieved spectrum of the self-compressed pulse. Dashed curves in (c) and (d) show the spectrum, intensity profile and phase of the input pulse.

Approaching the geometric focus, the filamentation regime sets in, as indicated by rapidly decreasing transmission in figure 3(b), as due to the multiphoton absorption and absorption by the free electron plasma. As a result, the input Gaussian beam is reshaped into a filament with characteristic intensity distribution, consisting of an intense core and a ring-shaped periphery, as shown in figure 2(d), which develops due to the interplay between self-focusing and multiphoton absorption [29]. In the filamentation regime, the input pulse continues to self-compress; the maximum self-compression of the pulse down to 19 fs, that equates to 1.6 optical cycles was measured when CaF_2 plate was located 1 mm before the geometric focus, where energy transmission decreased down to 66%. As compared to the case of lossless self-compression, the self-compressed peak contained just 33% of the transmitted energy, while the rest of energy was located in well-pronounced sidelobes, which developed due to spatiotemporal reshaping of the entire wave packet. Large sidelobes and even conditional pulse splitting are the characteristic features of the self-compressed light bullet at the early stage of its formation (at short propagation lengths) in the conditions of large anomalous GVD [30].

The self-compression experiments were also performed using YAG and BaF_2 plates, which produced rather similar results, however yielding somewhat lower self-compression factors. Nevertheless, these materials were found more suitable for compressing the pulses at 3 and 4 μm, respectively, as will be shown below.

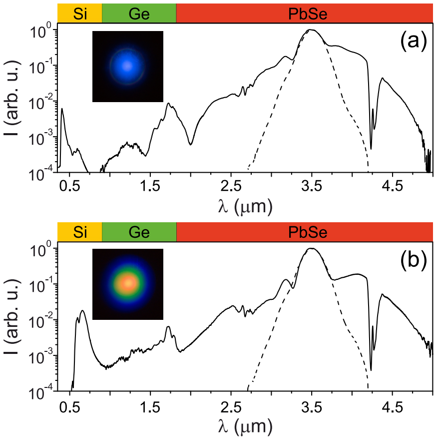

Figure 5. Axial supercontinuum spectra generated by filamentation of 3.5 μm pulses in (a) CaF_2 and (b) BaF_2, both of 4 mm thickness. Dashed curves show the input pulse spectrum. The ranges of spectrometer detectors (Si, Ge, PbSe) are indicated by color bars on the top. The insets show the visual appearances of the SC beams in the far field.

Filamentation in CaF_2 produced a broadband supercontinuum (SC) emission, with the broadest SC spectrum obtained at the point of maximum self-compression. The emergence of SC is indicated by the occurrence of a distinct blue spot in the far field, which is easily detected by visual means, while the entire SC spectrum extends up to 5 μm and is composed of two separate bands, as measured with a home-built scanning prism spectrometer with Si, Ge and PbSe detectors and illustrated in figure 5(a). A particularly strong SC signal is detected around the carrier wavelength in the $2-5$ μm range. In the visible range, SC spectrum features intense the so-called blue peak centered at 410 nm, with an ultraviolet cut-off at 385 nm, as estimated at the 10^{-4} intensity level. The characteristic feature of the SC spectrum in CaF_2 is the absence of the spectral components in between, in line with the observations reported in [31]. The SC spectrum also features a prominent peak centered at 1.75 μm that is the second harmonic generated in ZnSe, and a deep double dip around 4.25 μm as due to strong absorption band of atmospheric CO_2. A more spectrally homogenous SC, as shown in figure 5(b), was generated by replacing CaF_2 with BaF_2 plate of the same length and keeping the same position of the nonlinear medium with respect to the geometric focus. The SC spectrum in BaF_2 features a broad blue peak centered at 630 nm and provides a continuous spectral coverage from 510 nm in the visible to beyond 5 μm in the mid-infrared, which is the long-wave detection limit of our spectrometer.

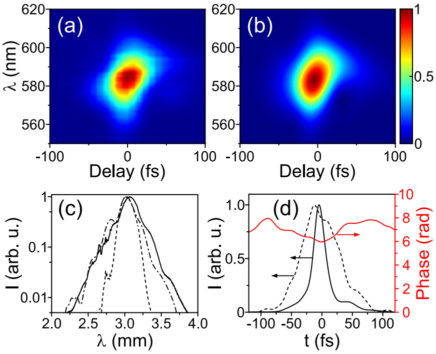

Figure 6. Lossless self-compression of 70 fs, 3 μm pulses down to 23 fs in 3 mm-thick YAG plate located at $z = -8$ mm: (a) measured and (b) retrieved SFG-FROG traces, (c) spectrum and (d) retrieved intensity profile and phase of the self-compressed pulse. Dash-dotted curve in (c) shows the retrieved spectrum of the self-compressed pulse. Dashed curves in (c) and (d) show the spectrum and intensity profile of the input pulse.

Finally, we verified the potential of wavelength tunability of the developed source and the possibility to perform lossless self-compression of the pulses at other wavelengths. 70 fs pulses with an energy of 31 μJ were obtained after DFG and OPA stages as the output wavelength was set at 3 μm. Threefold self-compression of these pulses down to 23 fs (2.3 optical cycles) was achieved in the lossless self-compression regime in 3 mm-thick YAG plate, whose input face was located 8 mm before the geometric focus ($z=-8$ mm). Figure 6 presents the measured and retrieved SFG-FROG traces, spectrum and retrieved temporal profile of the self-compressed pulse with the center wavelength of 3 μm. The superimposed dashed curves in figures 6(c) and (d) illustrate the spectrum and retrieved temporal profile of the input 70 fs pulse. Somewhat longer, 97 fs pulses with an energy of 14 μJ were generated as the DFG and OPA output wavelength was tuned to 4 μm. The best self-compression was achieved in 4 mm-thick BaF_2 plate located at $z=-3$ mm, yielding the compressed pulsewidth of 42 fs (not shown), which is equivalent to 3.2 optical cycles. In the latter case, a generally lower self-compression factor was in part attributed to CO_2 absorption, which considerably distorts the spectrum of the self-compressed pulse before it reaches the measurement setup.

3. Conclusions

In conclusion, we developed a simple and compact, Ti:sapphire laser-pumped mid-infrared source, which provides sub-3 optical cycle pulses with sub-30 μJ energy in the $3-4$ μm spectral range. The developed source employs difference frequency generation in KTA crystal between the signal and idler waves from a commercial near-infrared BBO OPA and subsequent parametric amplification in $LiIO_3$ crystal, which provides naturally broad amplification bandwidth. Thereafter the parametrically amplified pulses are self-compressed by the nonlinear propagation in wide bandgap dielectric media featuring anomalous GVD. In particular, we demonstrated lossless (with the energy throughput of above 90%) self-compression of sub-100 fs pulses down to sub-3 optical cycles in YAG, CaF_2 and BaF_2 plates of few mm thickness due to the interplay between the self-phase modulation and anomalous GVD and without the onset of self-focusing effects, as verified by the measurements of the output beam profile. Pulse self-compression down to sub-2 optical cycles was demonstrated at 3.5 μm in the filamentation regime in CaF_2, with the energy throughput of 66%. The developed source perfectly fits for diverse studies of ultrafast light-matter interactions in the mid-infrared spectral range in dielectric (e.g., as demonstrated by ultrabroadband supercontinuum generation in CaF_2 and BaF_2 in the present study), as well as in semiconductor media.

Acknowledgment

This research was funded by a grant No. APP-8/2016 from the Research Council of Lithuania.

References

[1] Biegert J, Bates P K and Chalus O 2012 New mid-infrared light sources *IEEE J. Sel. Top. Quantum Electron.* **18** 531–40

[2] Pires H, Baudisch M, Sanchez D, Hemmer M and Biegert J 2015 Ultrashort pulse generation in the mid-IR *Prog. Quantum Electron.* **43** 1–30

[3] Cussat-Blanc S, Ivanov A, Lupinski D and Freysz E 2000 $KTiOPO_4$,$KTiOAsO_4$, and $KNbO_3$ crystals for mid-infrared femtosecond optical parametric amplifiers: analysis and comparison *Appl. Phys. B* **70** S247–52

[4] Petrov V, Rotermund F and Noack F 2001 Generation of high-power femtosecond light pulses at 1 kHz in the mid-infrared spectral range between 3 and 12 μm by second-order nonlinear processes in optical crystals *J. Opt. A* **3** R1–19

[5] Gruetzmacher J A and Scherer N F 2002 Few-cycle mid-infrared pulse generation, characterization, and coherent propagation in optically dense media *Rev. Sci. Instrum.* **73** 2227–36

[6] Fecko C J, Loparo J J and Tokmakoff A 2004 Generation of 45 femtosecond pulses at 3 μm with a $KNbO_3$ optical parametric amplifier *Opt. Commun.* **241** 521–8

[7] Isaienko O and Borguet E 2011 Ultra-broadband sum-frequency vibrational spectrometer of aqueous interfaces based on a non-collinear optical parametric amplifier *Opt. Express* **20** 547–61

[8] Boulesbaa A, Isaienko O, Tuladhar A and Borguet E 2013 Generation of sub-30-fs microjoule mid-infrared pulses for ultrafast vibrational dynamics at solid/liquid interfaces *Opt. Lett.* **38** 5008–10

[9] Bradler M, Homann C and Riedle E 2011 Mid-IR femtosecond pulse generation on the microjoule level up to 5 μm at high repetition rates *Opt. Lett.* **36** 4212–4

[10] Brida D, Manzoni C, Cirmi G, Marangoni M, De Silvestri S and Cerullo G 2007 Generation of broadband mid-infrared pulses from an optical parametric amplifier *Opt. Express* **15** 15035–40

[11] Brida D, Marangoni M, Manzoni C, De Silvestri S and Cerullo G 2008 Two-optical-cycle pulses in the mid-infrared from an optical parametric amplifier *Opt. Lett.* **33** 2901–3

[12] Kaindl R A, Wurm M, Reimann K, Hamm P, Weiner A M and Woerner M 2000 Generation, shaping, and characterization of intense femtosecond pulses tunable from 3 to 20 μm *J. Opt. Soc. Am. B* **17** 2086–94

[13] Darginavičius J, Tamošauskas G, Piskarskas A, Valiulis G and Dubietis A 2012 Generation of tunable few optical-cycle pulses by visible-to-infrared frequency conversion *Appl. Phys. B* **108** 1–7

[14] Darginavičius J, Garejev N and Dubietis A 2012 Generation of carrier-envelope phase-stable two optical-cycle pulses at 2 μm from a noncollinear beta-barium borate optical parametric amplifier *Opt. Lett.* **37** 4805–7

[15] Bradler M, Homann C and Riedle E 2013 Broadband difference frequency mixing between visible and near-infrared pulses for few-cycle pulse generation with stable carrier-envelope phase *Appl. Phys. B* **113** 19–25

[16] Silva F, Austin D R, Thai A, Baudisch M, Hemmer M, Faccio D, Couairon A and Biegert J 2012 Multi-

octave supercontinuum generation from mid-infrared filamentation in a bulk crystal *Nat. Commun.* **3** 807

[17] Durand M, Jarnac A, Houard A, Liu Y, Grabielle S, Forget N, Durécu A, Couairon A and Mysyrowicz A 2013 Self-guided propagation of ultrashort laser pulses in the anomalous dispersion region of transparent solids: a new regime of filamentation *Phys. Rev. Lett.* **110** 115003

[18] Chekalin S V, Dokukina A E, Dormidonov A E, Kompanets V O, Smetanina E O and Kandidov V P 2015 Light bullets from a femtosecond filament *J. Phys. B* **48** 094008

[19] Gražulevičiūtė I, Šuminas R, Tamošauskas G, Couairon A and Dubietis A 2015 Carrier-envelope phase-stable spatiotemporal light bullets *Opt. Lett.* **40** 3719–22

[20] Majus D, Tamošauskas G, Gražulevičiūtė I, Garejev N, Lotti A, Couairon A, Faccio D and Dubietis A 2014 Nature of spatiotemporal light bullets in bulk Kerr media *Phys. Rev. Lett.* **112** 193901

[21] Liang H., Krogen P, Grynko R, Novak O, Chang C-L, Stein G J, Weerawarne D, Shim B, Kärtner F X and Hong K-H 2015 Three-octave-spanning supercontinuum generation and sub-two-cycle self-compression of mid-infrared filaments in dielectrics *Opt. Lett.* **40** 1069–72

[22] Šuminas R, Tamošauskas G, Valiulis G and Dubietis A 2016 Spatiotemporal light bullets and supercontinuum generation in β-BBO crystal with competing quadratic and cubic nonlinearities *Opt. Lett.* **41** 2097–100

[23] Hemmer M, Baudisch M, Thai A, Couairon A and Biegert J 2013 Self-compression to sub-3-cycle duration of mid-infrared optical pulses in dielectrics *Opt. Express* **21** 28095–102

[24] Baudisch M, Pires H, Ishizuki H, Taira T, Hemmer M and Biegert J 2015 Sub-4-optical-cycle, 340 MW peak power, high stability mid-IR source at 160 kHz *J. Opt.* **17** 094002

[25] Shumakova V, Malevich P, Ališauskas S, Voronin A, Zheltikov A M, Faccio D, Kartashov D, Baltuška A and Pugžlys A 2016 Multi-millijoule few-cycle mid-infrared pulses through nonlinear self-compression in bulk *Nat. Commun.* **7** 12877

[26] Yin Y, Li J, Ren X, Wang Y, Chew A and Chang Z 2016 High-energy two-cycle pulses at 3.2 μm by a broadband-pumped dual-chirped optical parametric amplification *Opt. Express* **24**, 24989-98

[27] Voronin A A and Zheltikov A M 2016 Asymptotically one-dimensional dynamics of high-peak-power ultrashort laser pulses *J. Opt.* **18** 115501

[28] Voronin A A and Zheltikov A M 2016 Pulse self-compression to single-cycle pulse widths a few decades above the self-focusing threshold *Phys. Rev. A* **94** 023824

[29] Dubietis A, Gaižauskas E, Tamošauskas G and Di Trapani P 2004 Light filaments without self-channeling *Phys. Rev. Lett.* **92** 253903

[30] Gražulevičiūtė I, Garejev N, Majus D, Jukna V, Tamošauskas G and Dubietis A 2016 Filamentation and light bullet formation dynamics in solid-state dielectric media with weak, moderate and strong anomalous group velocity dispersion *J. Opt.* **18** 025502

[31] Dormidonov A E, Kompanets V O, Chekalin S V and Kandidov V P 2015 Giantically blue-shifted visible light in femtosecond mid-IR filament in fluorides *Opt. Express* **23** 29202–10

A2

SUPERCONTINUUM GENERATION IN MIXED THALLOUS HALIDES KRS-5 AND KRS-6

A. Marcinkevičiūtė, G. Tamošauskas, A. Dubietis

Opt. Mater. **78**, 339–344 (2018)

Reprinted with permission from Optical Materials

Supercontinuum generation in mixed thallous halides KRS-5 and KRS-6

Agnė Marcinkevičiūtė, Gintaras Tamošauskas, Audrius Dubietis*

Laser Research Center, Vilnius University, Saulėtekio Avenue 10, LT-10223 Vilnius, Lithuania

---

Abstract

We experimentally study supercontinuum generation in mixed thallous halides: thallium bromoiodide (KRS-5) and thallium chlorobromide (KRS-6), as pumped with mid-infrared femtosecond pulses. Almost 2 octave-wide supercontinuum spectra spanning wavelengths from $\sim 1.5\ \mu$m to more than $5.5\ \mu$m were produced by self-focusing of 60 fs pulses with central wavelengths of $3.1\ \mu$m and $3.6\ \mu$m in KRS-5 and KRS-6 samples of 6 mm thickness, in the single and multiple filamentation regimes. Our measurements revealed remarkably low energy thresholds (few hundreds of nanojoules) for supercontinuum generation in these materials due to very large values of nonlinear indexes of refraction ($n_2 = 10.5 \times 10^{-15}$ cm^2/W for KRS-5 and $n_2 = 5.4 \times 10^{-15}$ cm^2/W for KRS-6), which were experimentally evaluated from the nonlinear propagation dynamics. A combination of high nonlinearity and wide infrared transparency range make KRS-5 and KRS-6 very attractive bulk materials for SC generation in the mid-infrared spectral range.

Keywords: Supercontinuum generation, Femtosecond filamentation, Mixed thallous halides, Nonlinear index of refraction

---

1. Introduction

Spectral superbroadening of intense femtosecond laser pulses in condensed bulk media constitutes a simple, compact and alignment-insensitive technique for production of broadband coherent radiation, termed supercontinuum (SC) [1]. The emerging applications in many fields of modern ultrafast

---

*Corresponding author, tel.: +370-5-2366075; e-mail: audrius.dubietis@ff.vu.lt

Preprint submitted to Optical Materials *January 15, 2018*

science demand achieving broadband radiation at various parts of the optical spectrum. The mid-infrared spectral range is of particular interest for spectroscopic studies in the so-called molecular fingerprint region, development of mid-infrared optical parametric chirped pulse amplifiers and pulse compression techniques.

A widely used approach for SC generation in this wavelength range relies on femtosecond filamentation at laser wavelengths falling into the region of anomalous group velocity dispersion of wide-bandgap dielectric crystals and glasses, yielding generation of multioctave SC with continuous spectral coverage from the ultraviolet to the mid-infrared [2–9]. However, the most widely used dielectric materials, such as fused silica, sapphire and YAG exhibit rather limited transparency in the mid-infrared: fused silica transmits the wavelengths up to 3.5 μm, whereas sapphire and YAG become strongly absorbing for wavelengths greater than 5.2 μm [10]. SC generation in fluoride crystals, which possess wider transparency, such as CaF_2 and BaF_2, also faces problems with the discontinuity of the SC spectra, as the pump wavelength is tuned further into the mid-infrared [11, 12].

Recent experimental studies suggested a number of alternative nonlinear materials, which have a great potential for SC generation in the mid-infrared. SC spectra with remarkable mid-infrared spectral coverage were produced in fluoride [13], tellurite [14, 15], lanthanum [16] and chalcogenide [17–19] glasses. Bulk semiconductor crystals also emerge as very attractive nonlinear media for SC generation in the mid-infrared, in part due to much larger cubic nonlinearities than in dielectrics and in part due to considerably extended infrared transparency windows. In that regard, SC generation was reported in gallium arsenide (GaAs) [20–22], zinc sulphide (ZnS) [5], and zinc selenide (ZnSe) [23, 24] crystals. Recent numerical simulations predicted that filamentation of femtosecond mid-infrared pulses in alkali metal halides, which possess extremely broad mid-infrared transmittance and whose zero GVD points are located deeply in the mid-infrared, are capable of producing multi-octave SC spectra with remarkable red shifts [25].

In this paper we experimentally study SC generation in mixed thallous halides: thallium bromoiodide (KRS-5) and thallium chlorobromide (KRS-6) as produced by self-focusing of 60 fs pulses with central wavelengths of 3.1 μm and 3.6 μm, in single and multiple filamentation regimes. Based on our experimental results, we identify KRS-5 and KRS-6 as excellent nonlinear materials, which have a great potential for SC generation in the mid-infrared spectral range.

2. Materials and experimental details

Mixed thallous halides: thallium bromoiodide, Tl(Br,I) (KRS-5) and thallium chlorobromide, Tl(Cl,Br) (KRS-6) are dielectric crystals of cubic symmetry, which possess relatively small energy bandgaps and very broad infrared transparency, which extends into far infrared, see Table 1. These materials exhibit a certain transparency in the visible spectral range: Fig. 1 shows the measured transmittance in the visible and near-infrared spectral ranges of 2 mm-thick KRS-5 and KRS-6 samples, indicating the short wave cut-off wavelengths of 550 nm and 400 nm for KRS-5 and KRS-6, respectively.

Table 1: Relevant linear and nonlinear parameters of mixed thallous halides. E_g is the energy bandgap from [26]; the transmission range is defined at 10% transmission level in 1 mm thick sample, data from [10]; n_0 is the linear refractive index at 3.1 μm; n_2^{exp} and n_2^{calc} are the measured and calculated nonlinear refractive indexes, respectively, as evaluated in the present study.

Material	U_g eV	Transmittance μm	n_0	n_2^{exp} $\times 10^{-15}$ cm^2/W	n_2^{calc} $\times 10^{-15}$ cm^2/W
KRS-5	2.5	0.58 – 42	2.386	10.5	9.8
KRS-6	3.25	0.42 – 27	2.194	5.4	3.9

KRS-5 and KRS-6 are well-known infrared window materials [27], which also find applications in the mid-infrared [28] and gamma-ray [29] spectroscopy, and astronomical instrumentation [30, 31]. KRS-5 was recently considered for use in acoustooptics [32, 33]. However, from the perspective of nonlinear optics, KRS-5 and KRS-6 appear exotic, and to the best of our knowledge, these crystals were never considered as nonlinear optical materials.

In the experiment we used KRS-5 and KRS-6 samples manufactured by Crystaltechno Ltd. (Russia), which are non-eutectic mixtures composed of 58 mol % thalium iodide (TlI) and of 60 % thallium chloride (TlCl), respectively. The experiments were performed with an amplified Ti:sapphire laser system (Spitfire-PRO, Newport-Spectra Physics) used to pump a commercial BBO crystal-based optical parametric amplifier (Topas-Prime, Light Conversion Ltd.), which provided 90 fs pulses tunable in the 1.1 – 2.5 μm range. The

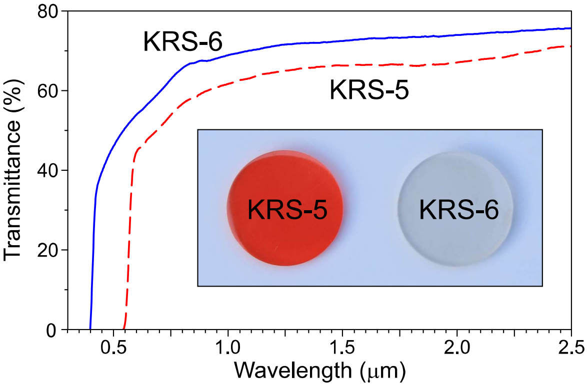

Figure 1: Measured transmittance of 2 mm-thick KRS-5 and KRS-6 samples in the visible and near infrared spectral ranges. The inset shows photos of these materials.

pulses in the $3 - 4$ μm range were produced by the difference frequency generation between the signal and idler outputs of the optical parametric amplifier in a 1 mm-thick KTA crystal and had a duration of 60 fs, see [12] for more details.

The chosen wavelengths fall into the range of normal group velocity dispersion (GVD) of KRS-5, which has a zero GVD wavelength at 6.6 μm, as calculated from the dispersion equation provided in [27]. It is expected that the input wavelengths fall into the range of normal GVD of KRS-6 as well, however, the exact value of its zero GVD point is not known with a reasonable precision, as there is a large mismatch between the GVD curves calculated from the dispersion equations for the infrared [34] and visible [35] wavelength ranges, which were derived for different molar compositions of TlCl.

The measurements of nonlinear transmission, which were used for evaluation of the nonlinear refractive indexes, were performed by focusing the input beam of 1.9 mm FWHM diameter with BaF_2 lens ($f = +50$ mm) onto the input face of 2 mm-thick samples of KRS-5 and KRS-6. The transmitted energy was measured using the energy meter (Ophir) with a pyroelectric detector (PE9-SH). In the SC generation experiments, looser focusing of the input beam (BaF_2 lens, $f = +100$ mm) and longer samples of KRS-5 and KRS-6 (both of 6 mm thickness) were used. The SC spectra were measured using a home-built scanning prism spectrometer with InAsSb detector, providing an effective detection range of $0.8-5.8$ μm. The filament profiles were measured by imaging the output face of the sample onto pyroelectric CCD camera (WinCamD, model FIR2-16-HR).

3. Evaluation of the nonlinear refractive indexes

Since the nonlinear optical properties of KRS-5 and KRS-6 are basically unknown, first we carried out an experiment in order to evaluate the nonlinear refractive indexes of these materials. The evaluation procedure is based on finding the self-focusing distance (the position of the nonlinear focus), which for a collimated input Gaussian beam is expressed by the empirical equation [36]:

$$z_{\rm sf} = \frac{0.367\ z_R}{\sqrt{[(P/P_{\rm cr})^{1/2} - 0.852]^2 - 0.0219}}, \tag{1}$$

where $z_R = \pi n_0 w_0^2/\lambda$ denotes the Rayleigh (diffraction) length of the input Gaussian beam of a radius w_0, and $P_{\rm cr}$ is the critical power for self focusing in the material:

$$P_{\rm cr} = \frac{3.77\lambda^2}{8\pi n_0 n_2}, \tag{2}$$

where n_0 and n_2 are the linear and nonlinear refractive indexes, respectively, and λ is the laser wavelength. Although Eq.(1) is generally derived in the case of continuous wave laser beams, it gives a fairly accurate approximation of the nonlinear focus of femtosecond laser pulses as well [37]. Having $z_{\rm sf}$, $P_{\rm cr}$ is then found from Eq.(1) and the value of n_2 is calculated from Eq.(2).

For that purpose we measured the nonlinear transmission of 2 mm-thick KRS-5 and KRS-6 samples at 3.1 μm versus the input pulse energy, as illustrated in Fig. 2(a). Taking into account the incident photon energy of 0.4 eV and the bandgap values listed in Table 1, the measured nonlinear losses are associated with 7 and 9 photon absorption in KRS-5 and KRS-6, respectively, and to some extent with the absorption of free electron plasma via inverse Bremsstrahlung effect [38].

The position of the nonlinear focus was derived from the calculated fractional losses (dT/dE), shown in Fig. 2(b). Since the nonlinear losses originate from an increase of the beam intensity due to self-focusing and filamentation,

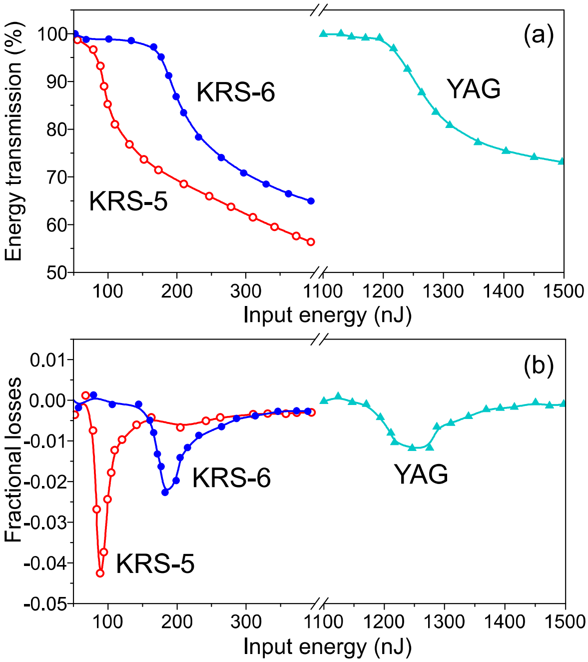

Figure 2: (a) Normalized energy transmission of 2 mm-thick KRS-5 and KRS-6 samples and 3 mm-thick YAG sample versus the energy of 60 fs, 3.1 μm input pulses. (b) Fractional losses, whose minima indicate that the position of the nonlinear focus is located at the output face of the sample.

the extremum of fractional losses provides a rather precise position of the nonlinear focus [39]. In the present case (for a fixed sample thickness), the minima of fractional losses provide the pulse energy and power (taking into account Fresnel reflection from the input face of the sample) for which the position of the nonlinear focus z_{sf} equals to the sample length (2 mm), or in other words, the nonlinear focus is located at the output face of the sample. Based on this assumption, the found n_2 values are 10.5×10^{-15} cm^2/W and 5.4×10^{-15} cm^2/W for KRS-5 and KRS-6, respectively. The measured n_2 values are fairly close to those calculated analytically ($n_2 = 9.8 \times 10^{-15}$ cm^2/W for KRS-5 and $n_2 = 3.9 \times 10^{-15}$ cm^2/W for KRS-6) using the formalism described in [40], with an updated dimensionless parameter $K' = 7.33 \times 10^{-9}$

from [41].

In order to further experimentally justify the validity of our approach for estimation of n_2, we measured the nonlinear transmission of 3 mm-thick YAG sample, whose nonlinear refractive index is known rather precisely ($n_2 = 6.2 \times 10^{-16}$ cm^2/W) for the laser wavelength of 1.06 μm [42]. The results for nonlinear transmission and fractional losses in YAG are added to Fig. 2 for a comparison; notice a significantly increased input pulse energy required to produce the nonlinear focus at the output face of 3 mm-thick YAG sample. Also notice generally smaller fraction of the absorbed energy, which is due to effectively 17-photon absorption, taking into account the bandgap of YAG of 6.5 eV. The above evaluation procedure yields n_2 value of 6.0×10^{-16} cm^2/W, which almost perfectly coincides with that specified in the literature, and bearing in mind the general dispersion law of n_2, which suggests a slight decrease of n_2 toward longer wavelengths.

4. Supercontinuum generation in KRS-5 and KRS-6

The estimated high values of n_2 in KRS-5 and KRS-6 suggest remarkably low critical powers for self-focusing in these materials: 0.58 MW in KRS-5 and 1.22 MW in KRS-6, respectively, assuming the laser wavelength of 3.1 μm, which are more than by an order of magnitude lower than in YAG (13.1 MW). Indeed, the threshold energies for filamentation and supercontinuum generation in 6 mm-thick KRS-5 and KRS-6 samples were found to be just few hundreds of nanojoules.

Figures 3(a)-3(d) show the SC spectra in KRS-5 as recorded with different input pulse energies, resulting in single and multiple filamentation regimes, as verified by the near-field intensity distributions of the output beams shown in the insets. The SC spectrum in KRS-5 as produced by the input pulses with an energy of 260 nJ, provides a continuous wavelength coverage from 1.57 to 5.0 μm (at the 5×10^{-4} intensity level) and exhibits a prominent double dip around 4.25 μm that is attributed to absorption of atmospheric CO$_2$, as illustrated in Fig. 3(a). The inset shows the intensity distribution measured at the output face of the sample, indicating a single filament with FWHM diameter of 27 μm, surrounded by a characteristic ring-shaped periphery. As the input pulse energy is increased to 390 nJ, the SC spectrum shows a stable short-wave cut-off at 1.57 μm due to the intensity clamping effect and exhibits a slight broadening to 5.3 μm on the long-wave side, while maintaining a single filament, as illustrated in Fig. 3(b). The SC spectra in the single filament regime demonstrate smooth spectral shapes, and yield reasonably high spectral energy density: $2-30$ pJ/nm in the $1.7-2.5$ μm range, $50-100$ pJ/nm in the $3.5-4.2$ μm range and > 200 pJ/nm around the pump wavelength.

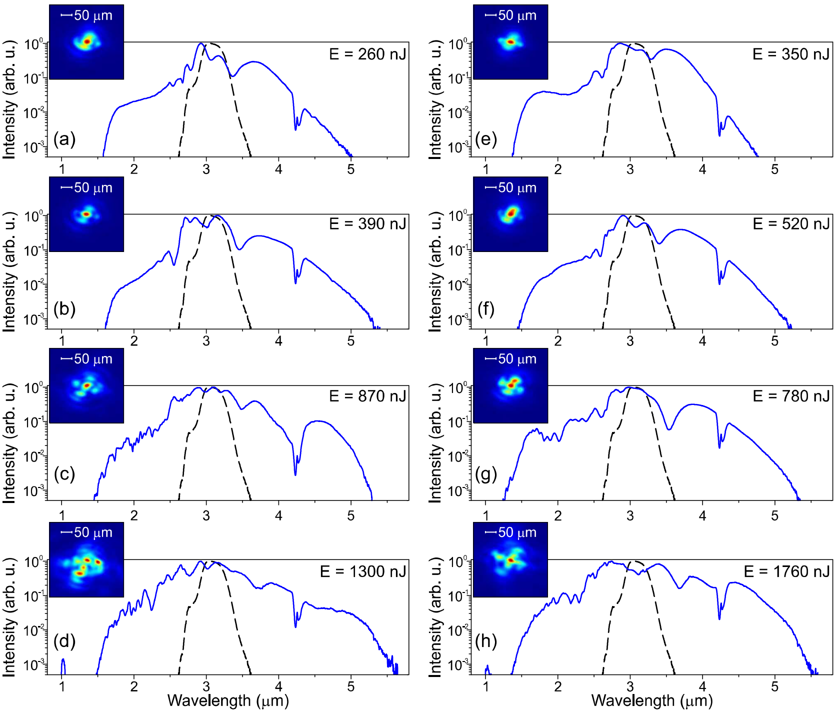

Figure 3: Supercontinuum spectra in 6 mm-thick KRS-5 (left panel) and in KRS-6 (right panel) samples as functions on the energy of the input 60 fs, 3.1 μm pulses. The input pulse energies are indicated in the plots and the input pulse spectra are depicted by dashed curves. Insets show filamentation patterns as measured at the output face of the sample.

A further increase of the input pulse energy leads to multiple filamentation. With the input pulse energy of 870 nJ, multiple filaments emerge in the form of a symmetric and well-reproducible pattern, as illustrated in the inset of Fig. 3(c). The occurrence of such multi-filamentation pattern is attributed to small ellipticity of the input beam [43]. The secondary filaments

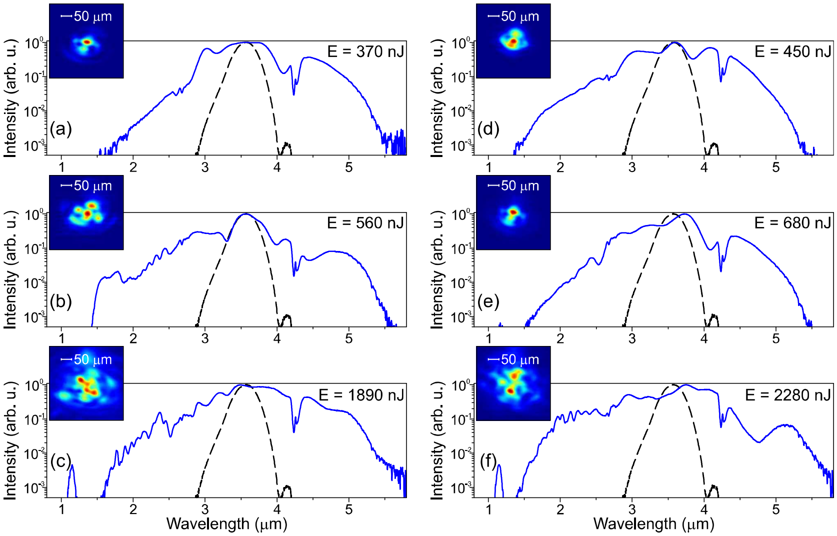

Figure 4: Supercontinuum spectra in 6 mm-thick KRS-5 (left panel) and in KRS-6 (right panel) samples as functions on the energy of the input 60 fs, 3.6 μm pulses. The input pulse energies are indicated in the plots and the input pulse spectra are depicted by dashed curves. Insets show filamentation patterns as measured at the output face of the sample.

evolve as a result of nucleation of annular rings surrounding the central filament and reside along the major and minor axes of an ellipse. Even higher input pulse energy (1.3 μJ) leads to random distribution of the individual filaments, as shown in the inset of Fig. 3(d). The regime of multiple filamentation produces slightly broader SC spectra spanning wavelengths from 1.5 to 5.6 μm. However, in this case, the SC spectra exhibit a significant intensity modulation, which is especially well-pronounced on the short-wave side. Spectral modulation originates from the filament refocusing [39] and in part due to beating between the SC spectra produced by individual filaments. Interestingly, with the input pulse energy of 1.3 μJ we capture also a detached narrow spectral peak centered at 1.03 μm, which is attributed to the third harmonic of the pump.

A very similar trend of the spectral broadening and transition from the single to multiple filamentation regimes versus the input pulse energy was recorded in KRS-6, as shown Figs. 3(e)-3(h). Due to lower n_2, the SC spectra in KRS-6 were generated with slightly higher input pulse energies. On the other hand, due to larger bandgap of KRS-6, the measured SC spectra exhibit slightly shorter cut-off wavelengths (1.37 μm) at the short-wave side, while the spectral broadening toward long-wave side remained essentially identical.

The experiments performed with the longer wavelength (3.6 μm) input pulses revealed very similar dynamics of the spectral broadening and filamentation versus the input pulse energy in both materials, as illustrated in Fig. 4. However, in the present case, in both samples a slightly larger spectral broadening on the long-wave side of the SC was recorded: up to 5.5 μm and slightly beyond 5.8 μm (which is the limit of our detection apparatus) in the regimes of single and multiple filamentation, respectively. Notice that in addition to prominent CO_2 absorption, smaller but clearly distinguishable dips around 2.7 μm as due to absorption of water vapor emerge in the SC spectra. Also notice a particularly intense third harmonic peaks at 1.2 μm in KRS-5 and KRS-6, which emerge in the multiple filamentation regime.

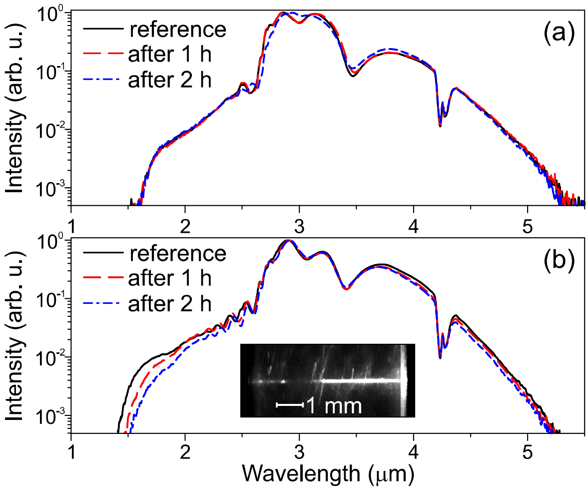

Figure 5: Long-term reproducibility of supercontinuum spectra in (a) KRS-5 and (b) KRS-6. The input pulse wavelength is 3.1 μm, the input pulse energies are 350 nJ and 500 nJ, respectively. Inset shows the side view of KRS-6 sample, as illuminated by He-Ne laser beam.

Finally, in order to test the suitability of KRS-5 and KRS-6 for SC generation under real experimental settings, we examined the long-term reproducibility of the SC spectra in these materials, which is of importance for the most of practical applications. Figure 5 compares the reference SC spectra with the SC spectra recorded after 1 hour and 2 hours of operation at 1 kHz repetition rate in KRS-5 and KRS-6 samples. The SC spectrum in KRS-5 shows an excellent long-term reproducibility: no apparent changes in either SC spectral shape or spectral intensity were detected over 2 hours of operation, as shown in Fig 5(a).

In contrast, the SC spectrum in KRS-6 exhibits a slight but noticeable shrinking on the short-wave side, which progresses with the exposure time, whereas the part of the SC spectrum on the long-wave side remains unchanged, as shown in Fig 5(b). The observed spectral changes in KRS-6 could be attributed to filament-induced material modification under multiple laser pulse exposure. The material modification was visualized by launching a He-Ne laser beam along the path of the filament, showing a clearly detectable scattering from the modified volume, as depicted in the inset of Fig. 5(b). On the other hand, the time scale of the spectral changes suggests that degradation of KRS-6, whatever is its origin, is relatively slow, so these detrimental effects could be easily avoided by the translation of the sample.

5. Conclusions

In conclusion, we evaluated the nonlinear indexes of refraction of mixed thallous halides: thallium bromoiodide (KRS-5) and thallium chlorobromide (KRS-6) and demonstrated efficient SC generation in these materials in the mid-infrared spectral range by self-focusing and filamentation of 60 fs pulses with carrier wavelengths of 3.1 and 3.6 μm. More specifically, almost 2 octave-spanning SC spectra, covering wavelength range from ~ 1.5 to ~ 5.5 μm, were produced in 6 mm-thick samples of KRS-5 and KRS-6. We demonstrated that filamentation and SC generation in these materials is achieved with remarkably low input pulse energies (few hundreds of nanojoules) owing to large nonlinear refractive indexes: $n_2 = 10.5 \times 10^{-15}$ cm^2/W for KRS-5 and $n_2 = 5.4 \times 10^{-15}$ cm^2/W for KRS-6, as evaluated from the measurements of the nonlinear transmission. Long-term spectral measurements revealed an excellent reproducibility of the SC spectrum in KRS-5, while the SC spectrum in KRS-6 showed slight shrinking at the short-wave side due to filament-induced modification of the material, which takes place on the time scale of an hour and therefore could be easily avoided by the translation of the sample. Summarizing our experimental findings, we conclude that mixed thallous halides KRS-5 and KRS-6 are very suitable nonlinear materials for femtosecond SC generation in the mid-infrared spectral range. Owing to large nonlinear index of refraction and broad infrared transparency of KRS-5 and KRS-6, we expect that using even longer pump wavelengths, femtosecond filamentation in the range of anomalous GVD of these materials might produce ultrabroadband and multioctave SC spectra extending into the far-infrared.

References

[1] A. Dubietis, G. Tamošauskas, R. Šuminas, V. Jukna, A. Couairon, Ultrafast supercontinuum generation in bulk condensed media, Lith. J. Phys. 57 (2017) 113–157.

[2] F. Silva, D. R. Austin, A. Thai, M. Baudisch, M. Hemmer, D. Faccio, A. Couairon, J. Biegert, Multi-octave supercontinuum generation from mid-infrared filamentation in a bulk crystal, Nat. Commun. 3 (2012) 807.

[3] J. Darginavičius, D. Majus, V. Jukna, N. Garejev, G. Valiulis, A. Couairon, A. Dubietis, Ultrabroadband supercontinuum and third-harmonic generation in bulk solids with two optical-cycle carrier-envelope phase-stable pulses at 2 μm, Opt. Express 21 (2013) 25210–25220.

[4] J. A. Dharmadhikari, R. A. Deshpande, A. Nath, K. Dota, D. Mathur, A. K. Dharmadhikari, Effect of group velocity dispersion on supercontinuum generation and filamentation in transparent solids, Appl. Phys. B 117 (2014) 471–479.

[5] H. Liang, P. Krogen, R. Grynko, O. Novak, C.-L. Chang, G. J. Stein, D. Weerawarne, B. Shim, F. X. Kärtner, K.-H. Hong, Three-octave-spanning supercontinuum generation and sub-two-cycle self-compression of mid-infrared filaments in dielectrics, Opt. Lett. 40 (2015) 1069-1072.

[6] H. Fattahi, H. Wang, A. Alismail, G. Arisholm, V. Pervak, A. M. Azzeer, F. Krausz, Near-PHz-bandwidth, phase-stable continua generated from a Yb:YAG thin-disk amplifier, Opt. Express 24 (2016) 24337–24346.

[7] N. Garejev, G. Tamošauskas, A. Dubietis, Comparative study of multi-octave supercontinuum generation in fused silica, YAG and LiF in the range of anomalous group velocity dispersion, J. Opt. Soc. Am. B 34 (2017) 88–94.

[8] R. Šuminas, G. Tamošauskas, G. Valiulis, A. Dubietis, Spatiotemporal light bullets and supercontinuum generation in β-BBO crystal with competing quadratic and cubic nonlinearities, Opt. Lett. 41 (2016) 2097–2100.

[9] H. Wang, A. Alismail, G. Barbiero, M. Wendl, H. Fattahi, Cross-polarized, multi-octave supercontinuum generation, Opt. Lett. 42 (2017) 2595–2598.

[10] M. J. Weber, Handbook of Optical Materials, CRC Press, 2003.

[11] A. E. Dormidonov, V. O. Kompanets, S. V. Chekalin, V. P. Kandidov, Giantically blue-shifted visible light in femtosecond mid-IR filament in fluorides, Opt. Express 23 (2015) 29202–29210.

[12] A. Marcinkevičiūtė, N. Garejev, R. Šuminas, G. Tamošauskas, A. Dubietis, A compact, self-compression-based sub-3 optical cycle source in the $3-4$ μm spectral range, J. Opt. 19 (2017) 105505.

[13] M. Liao, W. Gao, T. Cheng, X. Xue, Z. Duan, D. Deng, H. Kawashima, T. Suzuki, Y. Ohishi, Five-octave-spanning supercontinuum generation in fluoride glass, Appl. Phys. Express 6 (2013) 032503.

[14] M. Liao, W. Gao, T. Cheng, Z. Duan, X. Xue, H. Kawashima, T. Suzuki, Y. Ohishi, Ultrabroad supercontinuum generation through filamentation in tellurite glass, Laser Phys. Lett. 10 (2013) 036002.

[15] P. Béjot, F. Billard, C. Peureux, T. Diard, J. Picot-Clémente, C. Strutynski, P. Mathey, O. Mouawad, O. Faucher, K. Nagasaka, Y. Ohishi, F. Smektala, Filamentation-induced spectral broadening and pulse shortening of infrared pulses in Tellurite glass, Opt. Commun. 380 (2016) 245–249.

[16] Y. Yang, M. Liao, X. Li, W. Bi, Y. Ohishi, T. Cheng, Y. Fang, G. Zhao, W. Gao, Filamentation and supercontinuum generation in lanthanum glass, J. Appl. Phys. 121 (2017) 023107.

[17] Y. Yu, X. Gai, T. Wang, P. Ma, R. Wang, Z. Yang, D.-Y. Choi, S. Madden, B. Luther-Davies, Mid-infrared supercontinuum generation in chalcogenides, Opt. Mater. Express 3 (2013) 1075–1086.

[18] O. Mouawad, P. Béjot, F. Billard, P. Mathey, B. Kibler, F. Désévédavy, G. Gadret, J.-C. Jules, O. Faucher, F. Smektala, Mid-infrared filamentation-induced supercontinuum in As-S and an As-free Ge-S counterpart chalcogenide glasses, Appl. Phys. B 121 (2015) 433–438.

[19] A. M. Stingel, H. Vanselous, P. B. Petersen, Covering the vibrational spectrum with microjoule mid-infrared supercontinuum pulses in nonlinear optical applications, J. Opt. Soc. Am. B 34 (2017) 1163–1168.

[20] S. Ashihara, Y. Kawahara, Spectral broadening of mid-infrared femtosecond pulses in GaAs, Opt. Lett. 34 (2009) 3839–3841.

[21] A. A. Lanin, A. A. Voronin, E. A. Stepanov, A. B. Fedotov, A. M. Zheltikov, Frequency-tunable sub-two-cycle 60-MW-peak-power free-space waveforms in the mid-infrared, Opt. Lett. 39 (2014) 6430–6433.

[22] A. A. Lanin, A. A. Voronin, E. A. Stepanov, A. B. Fedotov, A. M. Zheltikov, Multioctave, $3-18$ μm sub-two-cycle supercontinua from self-compressing, self-focusing soliton transients in a solid, Opt. Lett. 40 (2015) 974–977.

[23] O. Mouawad, P. Béjot, F. Billard, P. Mathey, B. Kibler, F. Désévédavy, G. Gadret, J.-C. Jules, O. Faucher, F. Smektala, Filament-induced visible-to-mid-IR supercontinuum in a ZnSe crystal: Towards multi-octave supercontinuum absorption spectroscopy, Opt. Mater. 60 (2016) 355–358.

[24] R. Šuminas, G. Tamošauskas, G. Valiulis, V. Jukna, A. Couairon, A. Dubietis, Multi-octave spanning nonlinear interactions induced by femtosecond filamentation in polycrystalline ZnSe, Appl. Phys. Lett. 110 (2017) 241106.

[25] S. A. Frolov, V. I. Trunov, V. E. Leshchenko, E. V. Pestryakov, Multi-octave supercontinuum generation with IR radiation filamentation in transparent solid-state media, Appl. Phys. B 122 (2016) 124.

[26] E. D. Palik (ed.), Handbook of optical constants of solids, Academic Press, 1998.

[27] A. Z. Tropf, M. E. Thomas, W. J. Tropf, Optical properties of KRS-5, Proc. SPIE 3060 (1997) 344–355.

[28] H. Minato, Y. Ishido, Development of an infrared absorption measurement method using the photothermal deflection effect of thallium bromide iodide (KRS-5): Measurement with a stepped-scan Fourier transform infrared spectrometer, Rev. Sci. Instr. 72 (2001) 2889–2892.

[29] H. Kim, A. Churilov, G. Ciampi, L. Cirignano, W. Higgins, S.Kim, P.O'Dougherty, F. Olschner, K. Shah, Continued development of thallium bromide and related compounds for gamma-ray spectrometers, Nucl. Instr. Meth. Phys. Res. A 629 (2011) 192–196.

[30] J. T. Rayner, Evaluation of a solid KRS-5 grism for infrared astronomy, Proc. SPIE 3354 (1998) 289–294.

[31] N. E. Bowles, M. Tecza, J. K. Barstow, J. M. Temple, P. G. J. Irwin, L. N. Fletcher, S. Calcutt, J. Hurley, M. Ferlet, D. Freeman, The Long wave ($11 - 16$ μm) spectrograph for the EChO M3 Mission Candidate study, Exp. Astron. 40 (2015) 801–811.

[32] S. N. Mantsevich, Thallium bromide iodide crystal acoustic anisotropy examination, Ultrasonics 75 (2017) 91–97.

[33] V. B. Voloshinov, D. L. Porokhovnichenko, E. A. Dyakonov, Optimization of acousto-optic interaction geometry in KRS-5 crystal for far-infrared applications, Opt. Eng. 56 (2017) 087102.

[34] G. Hettner and G. Leisegang, Dispersion of mixed crystals TlBr-TlI (KRS 5) and TlCl-TlBr (KRS 6) in the infrared, Optik 3 (1948) 305–314.

[35] K. Takahei and K. Kobayashi, Reflectivity spectra of TlCl-TlBr mixed crystals, J. Phys. Soc. Jpn. 43 (1977) 891–898.

[36] J. H. Marburger, Self-focusing: Theory, Prog. Quantum Electron. 4 (1975) 35–110.

[37] A. Couairon, E. Brambilla, T. Corti, D. Majus, O. de J. Ramírez-Góngora, M. Kolesik, Practitioner‘s guide to laser pulse propagation models and simulation, Eur. Phys. J. Special Topics 199 (2011) 5–76.

[38] A. Couairon, A. Mysyrowicz, Femtoseconmd filamentation in transparent media, Phys. Rep. 441 (2007) 47–190.

[39] A. Jarnac, G. Tamošauskas, D. Majus, A. Houard, A. Mysyrowicz, A. Couairon, A. Dubietis, Whole life cycle of femtosecond ultraviolet filaments in water, Phys. Rev. A 89 (2014) 033809.

[40] M. Sheik-Bahae, D. C. Hutchings, D. J. Hagan, and E. W. Van Stryland, Dispersion of bound electronic nonlinear refraction in solids, IEEE J. Quantum Electron. 27 (1991) 1296–1309.

[41] R. DeSalvo, A. A. Said, D. J. Hagan, E. W. Van Stryland, and M. Sheik-Bahae, Infrared to ultraviolet measurements of two-photon absorption and n_2 in wide bandgap solids, IEEE J. Quantum Electron. 32 (1996) 1324–1333.

[42] R. Adair, L. L. Chase, S. A. Payne, Nonlinear refractive index of optical crystals, Phys. Rev. B 39 (1989) 3337–3350.

[43] A. Dubietis, G. Tamošauskas, G. Fibich, B. Ilan, Multiple filamentation induced by input-beam ellipticity, Opt. Lett. 29 (2004) 1126–1128.

A3

SUPERCONTINUUM GENERATION IN THE ABSENCE AND IN THE PRESENCE OF COLOR CENTERS IN NACL AND KBR

A. Marcinkevičiūtė, V. Jukna, R. Šuminas, N. Garejev,
G. Tamošauskas, A. Dubietis

Results Phys. **14**, 102396 (2019)

Reprinted with permission from Results in Physics

Supercontinuum generation in the absence and in the presence of color centers in NaCl and KBr

A. Marcinkevičiūtė, V. Jukna, R. Šuminas, N. Garejev, G. Tamošauskas, A. Dubietis*

Laser Research Center, Vilnius University, Saulėtekio Avenue 10, LT-10223 Vilnius, Lithuania

Abstract

We study supercontinuum generation with femtosecond mid-infrared laser pulses in NaCl and KBr crystals when pumped at the vicinity of their zero group velocity dispersion points. Almost three octave-spanning SC spectra (covering the $0.7 - 5.4$ μm and $0.85 - 5.4$ μm ranges in 5 mm-thick NaCl and KBr samples, respectively) were produced by filamentation of 70 fs, 3.6 μm input pulses in continuously translated samples. In the static setup, we show that rapid formation of persistent color centers (within a few seconds at 500 Hz repetition rate) inside these materials results in a marked decrease (by 40%) of the overall energy transmittance and in significant narrowing of SC spectra. We also demonstrate that the effect of color centers on the SC spectrum could be adequately simulated numerically using a simple phenomenological model which considers color centers as impurities with a certain energy bandgap.

1. Introduction

Supercontinuum (SC) generation through filamentation of femtosecond laser pulses in bulk solid-state media represents a simple, efficient and well-established technique for the production of coherent broadband radiation at various parts of the optical spectrum [1]. SC generation in the mid-infrared spectral range currently attracts a great deal of scientific and technological interest. This interest is inspired by the time-resolved spectroscopy in the molecular fingerprint region and in particular, by the applications in the emerging field of ultrafast mid-infrared nonlinear optics, offering an easy way for production of few optical cycle pulses, which could be further shaped and/or parametrically amplified up to very high peak powers, see e.g. [2, 3]. To date, the ultrabroad, multioctave SC spectra spanning the wavelengths from the UV to the MIR have been produced with mid-infrared pumping in a number of popular wide-bandgap dielectric

---

*Corresponding author
Email address: `audrius.dubietis@ff.vu.lt` (A. Dubietis)

Preprint submitted to Results in Physics *May 21, 2019*

materials: oxides, such as YAG, sapphire and fused silica, and alkali metal fluorides, such as CaF_2, BaF_2 and LiF [4, 5, 6, 7, 8, 9, 10].

Proper choice of the nonlinear medium is an important issue concerning the generation of broadband radiation within a desired wavelength range, as the physical factors that define the width of the SC spectrum are tightly linked to relevant optical parameters of the material. It is well established that the order of the multiphoton absorption (that is the ratio of the material bandgap and the incident photon energy) [11] and chromatic dispersion [12] define the attainable blue-shift of the SC spectrum in a given nonlinear material. On the other hand, an explicit numerical study of SC generation in various nonlinear materials with mid-infrared laser pulses suggested that the zero GVD wavelength may serve as a reasonably good indicator for attainable red-shift of the SC spectrum [13].

For what concerns the latter criterion, the zero GVD points of the above mentioned materials are located in the near infrared, at wavelengths generally shorter that 2 μm. Therefore, the materials whose zero GVD points are located in the MIR, e.g. soft glasses [14, 15, 16, 17], semiconductors [18, 19, 20, 21, 22, 23] and narrow bandgap dielectric crystals [24, 25] emerge as very efficient nonlinear media for SC generation in the mid-infrared. In further search of other suitable materials, the numerical simulations of filamentation and spectral broadening in alkali halide crystals identified them as attractive candidates. To this end, the simulations with pump pulses having carrier wavelengths slightly above their zero GVD points, predict that multioctave SC spectra with very large red shifts reaching into the far-infrared could be potentially achieved [13].

In this paper we report on filamentation and multioctave SC generation in sodium chloride (NaCl) and potassium bromide (KBr) crystals using 70 fs pulses with a carrier wavelength of 3.6 μm, which falls slightly above the zero GVD point of NaCl and slightly below that of KBr. We demonstrate that these alkali metal halide crystals produce multioctave SC in the infrared, however they are prone to color center formation, which markedly modifies the shape and the width of the SC spectra.

2. Materials and methods

The experimental setup is depicted in Fig. 1. The mid-infrared input pulses with a central wavelength of 3.6 μm and 70 fs duration at 500 Hz repetition rate were produced by the difference frequency generation (DFG) between the signal (1309 nm) and idler (2057 nm) outputs of the Ti:sapphire laser-pumped optical parametric amplifier OPA (Topas-Prime, Light Conversion Ltd.) in a 1 mm-thick KTA crystal. DFG was performed in a slightly non-collinear geometry (the external beam crossing angle 0.3°), to easily remove the residual signal and idler components. The mid-infrared beam was focused with a BaF_2 lens L ($f = +100$ mm) into the focal spot of 55 μm FWHM diameter located 2 mm inside the nonlinear medium. The input pulse energy was varied by adjusting the energy of the signal wave by means of a neutral metal-coated variable density filter VDF (NDL-25C-2, Thorlabs Inc.) and was set to produce a single filament at the output of the nonlinear medium. This was verified by monitoring the

Table 1: Relevant linear and nonlinear optical parameters of NaCl and KBr. U_g is the bandgap, n_0 and g are the linear refractive index and the GVD coefficient at 3.6 μm, respectively, λ_0 is the zero GVD wavelength calculated from the dispersion equations given in [26]. n_2 is the nonlinear refractive index; data from [27, 28].

Material	NaCl	KBr
Transmittance (μm)	0.17 – 18	0.2 – 30.6
U_g (eV)	9.0	7.6
n_0	1.523	1.536
n_2 ($\times 10^{-16}$ cm^2/W)	4.35	7.95
λ_0 (μm)	2.76	3.83
g (fs^2/mm)	-34	$+5$

near-field intensity profile of the output beam with a micro-bolometric camera MBC (WinCamD, FIR2-16-HR). The spectral measurements were performed using a home-built scanning prism spectrometer with Si and InAsSb detectors, providing an effective detection range of 0.2 – 5.8 μm. In these measurements, the output face of the nonlinear medium was imaged by means of Ag-coated parabolic mirrors (PM) onto the input slit of the spectrometer, so effectively coupling the axial portion of the SC radiation along with a fraction of conical emission. The energy measurements were performed with a pyroelectric detector (D).

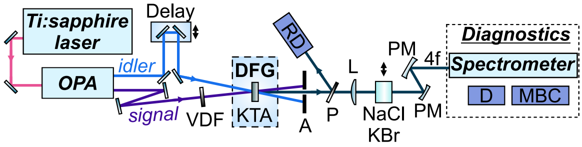

Figure 1: Schematic of the experimental setup. OPA: optical parametric amplifier, DFG: difference frequency generation, NaCl, KBr: crystal samples; arrows indicate the direction of translation, DM: dichroic mirror, PM: parabolic mirrors, VDF: variable density filter, L: focusing lens, MBC: micro-bolometric camera, A: iris aperture, P: thin YAG plate, RD: reference detector.

The nonlinear media used were uncoated NaCl and KBr samples of 5 mm thickness. The relevant optical parameters of these materials are presented in Table 1. NaCl and KBr are crystals with cubic symmetry and exhibit remarkable transparency ranges from the UV to the far-infrared and relatively large nonlinear indexes of refraction. The chosen pump wavelength of 3.6 μm falls close to their zero GVD points: in NaCl, GVD is slightly anomalous ($g = -34$ fs^2/mm), while in KBr, GVD is slightly normal ($g = +5$ fs^2/mm).

3. Results

Ultrabroadband, multi-octave SC spectra were recorded in NaCl and KBr samples of 5 mm thickness, pumped by 70 fs, 3.6 μm pulses having energies of

3.56 and 2.23 μJ, respectively, after accounting for a Fresnel reflection from the input faces of the samples, and illustrated in Fig. 2. These input pulse energies convert to the input powers of 51 MW and 32 MW, which correspond to 1.7 P_{cr} and 2.0 P_{cr} in NaCl and KBr, respectively, where $P_{\mathrm{cr}} = 3.77\lambda^2/8\pi n_0 n_2$ is the critical power for self-focusing calculated from the data provided in Table 1. During spectral scan, the samples were continuously translated (perpendicular to the pump beam direction) to avoid the influence of color center formation. More specifically, the measured SC spectrum in NaCl covered the wavelength range from 700 nm to 5.4 μm (at the 10^{-4} intensity level) that corresponds to 2.9 optical octaves. A slightly narrower SC spectrum, in the $0.85-5.4$ μm range, corresponding to 2.7 optical octaves was measured in KBr. Note distinct spectral dips around 2.7 and 4.25 μm that are absorption signatures of atmospheric H_2O and CO_2, respectively. Signatures of H_2O and CO_2 absorption could be removed in, e.g., nitrogen atmosphere, which also would be useful to extend the longevity of uncoated NaCl and KBr crystals, and especially their surfaces that degrade with time due to interaction with atmospheric humidity. These spectra further serve as references for monitoring spectral modifications due to evolving color centers in these materials when SC was generated in a static setup.

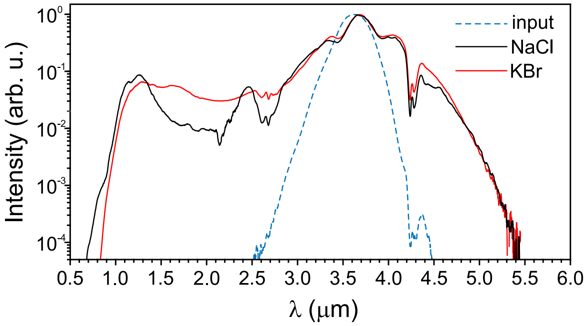

Figure 2: Supercontinuum spectra in NaCl (black curve) and KBr (red curve) produced by filamentation of 70 fs, 3.6 μm pulses and recorded while continuously translating the samples. The input pulse energies were 3.56 and 2.23 μJ, respectively. The input pulse spectrum is shown by a dashed curve.

Indeed, it is well known that most of alkali metal halide crystals are prone to formation of color centers that affect the SC spectrum to a certain degree, as experimentally demonstrated in LiF [8, 29, 30, 31, 32] and to some extent, in PbF_2 [25]. In alkali halides, color centers are products of self-trapped exciton decay, and the mechanism of their formation is known fairly well. After nonlinear ionization through multiphoton absorption that generates electrons and holes, the process starts from exciton creation, that is followed by self-trapping of the exciton and ends up with its decay, resulting in an occurrence of color centers [33]. The color centers are associated with electron trapping at a halide vacancy (F centers) and two F centers on adjacent sites (M centers, or the so-called F_2 centers) [34]. Color centers are responsible for the occurrence of broad absorption bands, whose peak wavelengths are located in the visible (F centers) and near infrared (M centers). More specifically, broad absorption bands in NaCl are centered at 460 nm (F centers) and at 725 nm (M centers) [35], while in KBr the respective absorption bands associated with F and M centers are more red-shifted and peak at 625 nm and 930 nm, respectively [36]. In addition to these, ultraviolet absorption bands are observed as well, that are due to V centers associated mostly with hole traps by impurities in these materials. The process of color center formation NaCl and KBr crystals is very fast, taking place on a μs time scale, as demonstrated in the conditions of intense femtosecond UV irradiation by pump-probe measurements [35, 36]. Rapid accumulation of color centers was justified by a drop of transmission at selected probe wavelengths, that eventually saturates after a few seconds at 1 kHz repetition rate [34].

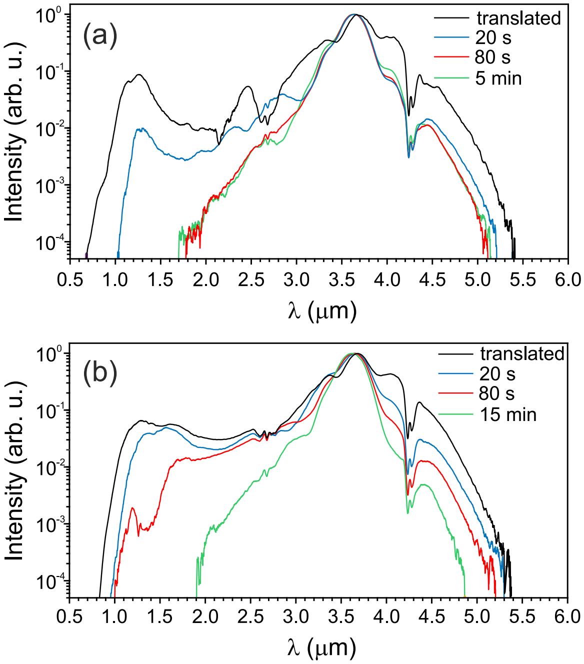

Figure 3: Evolutions of SC spectra in (a) NaCl, (b) KBr as functions of exposure time.

Figure 3(a) shows the evolution of SC spectrum in NaCl as a function of exposure time. Due to color center formation, the SC spectrum experiences a considerable shrinking along with a decrease of the spectral intensity on both sides of the carrier wavelength, and spectral shrinking is particularly pronounced at the short-wavelength side. Note that dramatic spectral changes emerge very quickly (within few tens of seconds at 500 Hz repetition rate). Thereafter color center-induced spectral dynamics settle down after 80 s of exposure, and the

SC spectrum keeps its new shape with a markedly reduced width ($1.8-5.1$ μm, as defined at the 10^{-4} intensity level) for the rest of the measurement time. A similar color center-induced narrowing of the SC spectrum was observed in KBr, as illustrated in Fig. 3(b). However, in the present case, the spectral dynamics are markedly slower: the shrinking of the SC spectrum finally settles just after 15 minutes of exposure time.

Changes of the SC spectra correlate very well with decrease of energy transmittances, recorded for both material samples and shown in Fig. 4. Here the energy transmittances are normalized to the transmittance levels which were measured in the absence of color centers, i.e. by continuously translating the samples. In other words, the unity transmittance was set with an account for Fresnel reflection from the output face of the sample and energy losses that occur in the filamentation process that are contributed by multiphoton absorption and absorption of free electron plasma via inverse Bremsstrahlung effect. Therefore the illustrated energy losses are contributed solely by linear and nonlinear absorption of the color centers. Notice that the energy transmittance decreases very rapidly and color centers take an immediate effect on the SC spectral width.

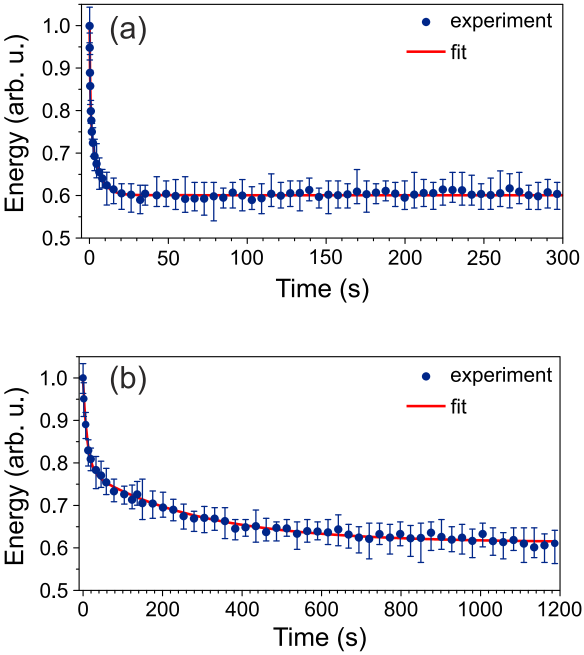

Figure 4: Measured energy transmittances (full circles) and their two-exponential fits (solid curves) for (a) NaCl and (b) KBr samples in a static setup. The plots are normalized to the sample transmittances in the absence of color centers.

NaCl shows a prompt drop of energy transmittance that is well fitted by two exponents with time constants of 0.53 s and 5.1 s, as shown in Fig. 4 (a). The energy transmittance after 20 seconds settles down to 60% of the initial transmittance value, which thereafter remains constant for rest of the measurement. The energy transmittance of KBr sample settles to an almost identical final value, however, the process is more extended in time (two-exponential decay with time constants of 10.6 s and 282 s), see Fig. 4(b). An established two-exponential decay in both materials could be attributed to different speeds of formation of F (a faster exponent) and M (a slower exponent) centers.

Finally, residual color centers are easily seen by a naked eye, as illustrated in Fig. 5. Their specific colors: moss-green in NaCl and ink-blue in KBr, are due to F center absorption bands in the visible range. Note that color centers are formed only at the filament site, i.e., where intensity and nonlinear losses due to multiphoton and free electron absorption are the highest, enablig to trace precisely the filament path.

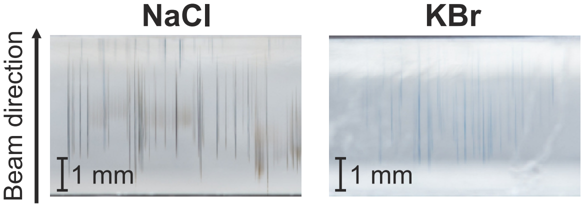

Figure 5: Photographs of (a) NaCl and (b) KBr samples with filament-induced color centers, which were produced by slightly varying the input pulse energies (around the specified values for NaCl and KBr) and exposure times (from a few tens of seconds to a few tens of minutes).

The SC spectra in NaCl were simulated numerically using a model which solves a unidirectional nonparaxial propagation equation for the pulse envelope, see [37] and [38] for details, taking relevant material parameters from Table 1 and input pulse parameters from the experiment. The effect of color centers was accounted for using a phenomenological approach, which considers them as evenly distributed impurities with an energy bandgap of 2.7 eV that corresponds to the strongest absorption band centered at 460 nm due to F centers [35]. The numerically simulated SC spectra using different impurity concentrations, which could be directly associated with accumulation of color centers while increasing exposure time in the experiment, are presented in Fig. 6.

The numerical results demonstrate a marked narrowing of SC spectrum as the density of the impurities increases. Of course, inclusion of color centers in the numerical model in that way, is a very simple approximation, since color center-induced modifications of relevant material properties, e.g., linear and nonlinear refractive indexes and dispersion were not considered. Nevertheless, even this simple numerical approach gives a fair agreement with experimentally recorded spectral dynamics. Therefore the following qualitative mechanism how color centers act on the width of SC spectrum could be unveiled. Since the

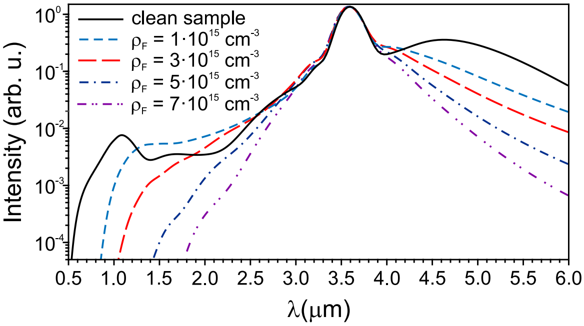

Figure 6: Numerically simulated SC spectra in NaCl with different impurity densities ρ_F that mimic the effect of color center absorption.

absorption band of color centers (F-centers, in the present case) does not overlap with SC spectrum, they do not absorb the SC radiation directly. This suggests that color centers absorb the input pulse energy via multiphoton absorption. The observed shrinking of SC spectrum is then explained by reduction of the effective material bandgap through formation of color center absorption band, which results in a decrease of clamping intensity and thus an increase of the limiting filament diameter, which in turn yield a narrower SC spectrum [11]. Multiphoton absorption of color centers readily produces a larger number of free electrons, which are then accelerated via inverse Bremsstrahlung and avalanche, and thus participate in further production of color centers. This lasts until the process reaches a certain equilibrium between the production and annihilation of color centers.

4. Conclusions

In conclusion, we experimentally studied SC generation in NaCl and KBr samples pumped by femtosecond mid-infrared laser pulses, in the absence and in the presence of color centers. Almost three octave-spanning SC spectra were recorded in these materials in the absence of color centers, as the samples were continuously translated during the measurement. In contrast, in the static setup, color centers in both materials are produced very quickly, resulting in a considerable reduction of the SC spectral widths and energy transmittances. The narrowing of SC spectrum in NaCl was simulated numerically using a simple phenomenological model of color centers, which considers them as impurities with an energy bandgap of 2.7 eV that corresponds to the F-center absorption band centered at 460 nm.

These results suggest that alkali metal halide crystals, such as NaCl and KBr may serve as potentially attractive nonlinear materials for multi-octave SC generation in the mid-infrared, however, a special care has to be taken to reduce the effect of color centers, which evolve on a very fast time scale (the estimated energy decay rates were few seconds at 500 Hz repetition rate). In particular, these effects should be taken into account considering the nonlinear propagation of very high power laser pulses with carrier wavelengths in the mid-infrared, where e.g., NaCl is considered as an attractive material for self-compression due to suitable nonlinear and dispersive properties [39].

Acknowledgment

The authors acknowledge financial support from the European Regional Development Fund (ERDF), Grant No. 1.2.2-LMT-K-718-02-0017.

References

[1] Dubietis A, Tamošauskas G, Šuminas R, Jukna V, Couairon A. Ultrafast supercontinuum generation in bulk condensed media. Lith J Phys 2017;57:113–57.

[2] Pires H, Baudisch M, Sanchez D, Hemmer M, Biegert J. Ultrashort pulse generation in the mid-IR. Prog Quantum Electron 2015;43:1–30.

[3] Krogen P, Suchowski H, Liang H, Flemens N, Hong KH, Kärtner FX, Moses J. Generation and multi-octave shaping of mid-infrared intense single-cycle pulses. Nat Photon 2017;11:222–6.

[4] Silva F, Austin DR, Thai A, Baudisch M, Hemmer M, Faccio D, Couairon A, Biegert J. Multi-octave supercontinuum generation from mid-infrared filamentation in a bulk crystal. Nature Commun 2012;3:807.

[5] Darginavičius J, Majus D, Jukna V, Garejev N, Valiulis G, Couairon A, Dubietis A. Ultrabroadband supercontinuum and third-harmonic generation in bulk solids with two optical-cycle carrier-envelope phase-stable pulses at 2 μm. Opt Express 2013;21:25210–20.

[6] Dharmadhikari JA, Deshpande RA, Nath A, Dota K, Mathur D, Dharmadhikari AK. Effect of group velocity dispersion on supercontinuum generation and filamentation in transparent solids. Appl Phys B 2014;117:471–9.

[7] Liang H, Krogen P, Grynko R, Novak O, Chang CL, Stein GJ, Weerawarne D, Shim B, Kärtner FX, Hong KH. Three-octave-spanning supercontinuum generation and sub-two-cycle self-compression of mid-infrared filaments in dielectrics. Opt Lett 2015;40:1069–72.

[8] Garejev N, Tamošauskas G, Dubietis A. Comparative study of multioctave supercontinuum generation in fused silica, YAG, and LiF in the range of anomalous group velocity dispersion. J Opt Soc Am B 2017;34:88–94.

[9] Marcinkevičiūtė A, Garejev N, Šuminas R, Tamošauskas G, Dubietis A. A compact, self-compression-based sub-3 optical cycle source in the $3-4$ μm spectral range. J Opt 2017;19:105505.

[10] Chekalin SV, Dormidonov AE, Kompanets VO, Zaloznaya ED, Kandidov VP. Light bullet supercontinuum. J Opt Soc Am B 2019;36:A43–53.

[11] Brodeur A, Chin SL. Band-gap dependence of the ultrafast white-light continuum. Phys Rev Lett 1998;80:4406–9.

[12] Kolesik M, Katona G, Moloney JV, Wright EM. Physical factors limiting the spectral extent and band gap dependence of supercontinuum generation. Phys Rev Lett 2003;91:043905.

[13] Frolov SA, Trunov VI, Leshchenko VE, Pestryakov EV. Multi-octave supercontinuum generation with IR radiation filamentation in transparent solid-state media. Appl Phys B 2016;122:124.

[14] Liao M, Gao W, Cheng T, Duan Z, Xue X, Kawashima H, Suzuki T, Ohishi Y. Ultrabroad supercontinuum generation through filamentation in tellurite glass. Laser Phys Lett 2013;10:036002.

[15] Yu Y, Gai X, Wang T, Ma P, Wang R, Yang Z, Choi DY, Madden S, Luther-Davies B. Mid-infrared supercontinuum generation in chalcogenides. Opt Mater Express 2013;3:1075–86.

[16] Mouawad O, Béjot P, Billard F, Mathey P, Kibler B, Désévédavy F, Gadret G, Jules JC, Faucher O, Smektala F. Mid-infrared filamentation-induced supercontinuum in As-S and an As-free Ge-S counterpart chalcogenide glasses. Appl Phys B 2015;121:433–8.

[17] Stingel AM, Vanselous H, Petersen PB. Covering the vibrational spectrum with microjoule mid-infrared supercontinuum pulses in nonlinear optical applications. J Opt Soc Am B 2017;34:1163–8.

[18] Lanin AA, Voronin AA, Stepanov EA, Fedotov AB, Zheltikov AM. Multioctave, $3-18$ μm sub-two-cycle supercontinua from self-compressing, self-focusing soliton transients in a solid. Opt Lett 2015;40:974–7.

[19] Mouawad O, Béjot P, Billard F, Mathey P, Kibler B, Désévédavy F, Gadret G, Jules JC, Faucher O, Smektala F. Filament-induced visible-to-mid-IR supercontinuum in a ZnSe crystal: Towards multi-octave supercontinuum absorption spectroscopy. Opt Mater 2016;60:355–8.

[20] Šuminas R, Tamošauskas G, Valiulis G, Jukna V, Couairon A, Dubietis A. Multi-octave spanning nonlinear interactions induced by femtosecond filamentation in polycrystalline ZnSe. Appl Phys Lett 2017;110:241106.

[21] Šuminas R, Marcinkevičiūtė A, Tamošauskas G, Dubietis A. Even and odd harmonics-enhanced supercontinuum generation in polyscrystalline zinc-blende semiconductors. J Opt Soc Am B 2019;36:A22–7.

[22] Werner K, Hastings MG, Schweinsberg A, Wilmer BL, Austin D, Wolfe CM, Kolesik M, Ensley TR, Vanderhoef L, Valenzuela A, Chowdhury E. Ultrafast mid-infrared high harmonic and supercontinuum generation with n_2 characterization in zinc selenide. Opt Express 2019;27:2867–85.

[23] Marcinkevičiūtė A, Jukna V, Šuminas R, Garejev N, Tamošauskas G, Dubietis A. Femtosecond filamentation and supercontinuum generation in bulk silicon. Opt Lett 2019;44:1343–6.

[24] Marcinkevičiūtė A, Tamošauskas G, Dubietis A. Supercontinuum generation in mixed thallous halides KRS-5 and KRS-6. Opt Mater 2018;78:339–44.

[25] Yang Y, Bi W, Li X, Liao M, Gao W, Ohishi Y, Fang Y, Li Y. Ultrabroadband supercontinuum generation through filamentation in lead fluoride crystal. J Opt Soc Am B 2019;36:A1–7.

[26] Weber MJ. Handbook of optical materials. CRC Press, London, 2003.

[27] Adair RL, Chase LL, Payne SA. Nonlinear refractive index of optical crystals. Phys Rev B 1989;39:3337–50.

[28] Sheik-Bahae M, Hutchings DC, Hagan DJ, Van Stryland EW. Dispersion of bound electronic nonlinear refraction in solids. IEEE J Quantum Electron 1991;27:1296–309.

[29] Kohl-Landgraf J, Nimsch JE, Wachtveitl J. LiF, an underestimated supercontinuum source in femtosecond transient absorption spectroscopy. Opt Express 2013; 21:17060–5.

[30] Kuznetsov AV, Kompanets VO, Dormidonov AE, Chekalin SV, Shlenov SA, Kandidov VP. Periodic colour-centre structure formed under filamentation of mid-IR femtosecond laser radiation in a LiF crystal. Quantum Electron 2016;46:379–86.

[31] Chekalin SV, Kompanets VO, Dormidonov AE, Kandidov VP. Influence of induced colour centres on the frequency-angular spectrum of a light bullet of mid-IR radiation in lithium fluoride. Quantum Electron 2017; 47:259–65.

[32] Chekalin SV, Kompanets VO, Dormidonov AE, Kandidov VP. Path length and spectrum of single-cycle mid-IR light bullets in transparent dielectrics. Quantum Electron 2018;48:372–7.

[33] Mao SS, Quéré F, Guizard S, Mao X, Russo RE, Petite G, Martin P. Dynamics of femtosecond laser interactions with dielectrics. Appl. Phys. A 2004;79:1695–709.

[34] Orlando S, Langford SC, Dickinson JT. Generation of color centers in alkali halide single crystals using ultrafast laser pulses. J Optoelecton Adv Mat 2010;12:707–10.

[35] Dickinson JT, Orlando S, Avanesyan SM, Langford SC. Color center formation in soda lime glass and NaCl single crystals with femtosecond laser pulses. Appl Phys A 2004;79:859–64.

[36] Dickinson JT, Langford SC, Avanesyan SM, Orlando S. Color center formation in KCl and KBr single crystals with femtosecond laser pulses. Appl Surf Sci 2007;253:7874–8.

[37] Couairon A, Brambilla E, Corti T, Majus D, de J. Ramírez-Góngora O, Kolesik M. Practitioner‘s guide to laser pulse propagation models and simulation. Eur Phys J Special Topics 2011;199:5–76.

[38] Dicaire I, Jukna V, Praz C, Milian C, Summerer L, Couairon A. Spaceborne laser filamentation for atmospheric remote sensing. Laser Photon Rev 2016;10:481–93.

[39] Bravy BG, Gordienko VM, Platonenko VT. Self-compression of terawatt level picosecond 10 μm laser pulses in NaCl. Laser Phys Lett 2014;11: 065401.

A4

FEMTOSECOND FILAMENTATION, SUPERCONTINUUM GENERATION, AND DETERMINATION OF N_2 IN POLYCRYSTALLINE SBN

R. Šuminas, N. Garejev, **A. Šuminienė**, V. Jukna,
G. Tamošauskas, A. Dubietis

J. Opt. Soc. Am. B **37**(4), 1530–1534 (2020)

Reprinted with permission from Journal of Optical Society of America B

Femtosecond filamentation, supercontinuum generation and determination of n_2 in polycrystalline SBN

ROSVALDAS ŠUMINAS, NAIL GAREJEV, AGNĖ ŠUMINIENĖ, VYTAUTAS JUKNA, GINTARAS TAMOŠAUSKAS AND AUDRIUS DUBIETIS*

Laser Research Center, Vilnius University, Saulėtekio Avenue 10, LT-10223 Vilnius, Lithuania
**audrius.dubietis@ff.vu.lt*

Abstract: We demonstrate that polycrystalline strontium barium niobate (SBN) serves as an excellent nonlinear material for supercontinuum generation in the near- and mid-infrared, as pumped by femtosecond pulses in the regions of its normal, zero and anomalous group velocity dispersion. We also show that broadband, octave-spanning planar second harmonic emission generated via random quasi phase matching usefully serves to precisely monitor focusing/refocusing cycles of a filament and to determine position of the nonlinear focus in particular, which was used to estimate the nonlinear index of refraction of the material applying the Marburger‘s law. The measured n_2 values are remarkably large: $44 \pm 7 \times 10^{-16}$ cm^2/W at 1.2 μm, $81 \pm 23 \times 10^{-16}$ cm^2/W at 2.0 μm and $100 \pm 15 \times 10^{-16}$ cm^2/W at 2.4 μm, and thus imply very low energy (below 100 nJ) and power (below 1 MW) thresholds for filamentation and SC generation in the infrared spectral range.

1. Introduction

Random quasi phase matching in disordered materials with second-order nonlinearity opens interesting perspectives in broadband frequency conversion of ultrashort light pulses [1]. A possibility to phase match virtually any wavelength that falls into the transparency range of these materials is provided by a natural disorder of orientations and grain-size distribution of individual crystallites [2]. To this end, polycrystalline zinc-blende semiconductors, such as ZnSe and ZnS, which are optically isotropic but possess second-order nonlinearity due to $\bar{4}3m$ symmetry, emerge as very attractive nonlinear materials. The frequency conversion processes in these materials become particularly efficient in the femtosecond filamentation regime due to high achieved intensity and localization of the pump, yielding ultrabroadband, multiple octave-spanning supercontinuum, whose short-wavelength side is remarkably extended by overlapping harmonics spectra, right down to the transparency edge [3–9].

Polycrystalline strontium barium niobate (SBN) is another interesting nonlinear material that can be used for various nonlinear optical processes at multiple wavelengths, including second and third harmonic generation without the need of angle or temperature tuning [10]. SBN is ferroelectric negative uniaxial crystal with an energy bandgap of 3.4 eV. The crystal is transparent in the 0.45 – 5.5 μm wavelength range [11] and has zero group velocity dispersion wavelength at 1.96 μm [12]. In contrast to polycrystalline zinc-blende semiconductors, polycrystalline SBN consists of birefringent needle-like randomly distributed ferroelectric domains whose widths vary between a few nanometers and a few micrometers and whose lengths are of a few hundreds of micrometers [13]. Broadband second and third harmonic generation in polycrystalline SBN was widely studied regarding harmonic spatial patterns, speckle structure, statistics and polarization properties [14–24]. Eventually, these studies resulted in practical applications, demonstrating adjustment-insensitive techniques for characterization of ultrashort light pulses [25–27]. However, the nonlinear effects related to the third-order nonlinearity in SBN have not been explicitly addressed so far.

In this Paper we study filamentation and supercontinuum generation in polycrystalline SBN with femtosecond near and mid-infrared laser pulses, whose carrier wavelengths fall into the ranges of normal, zero and anomalous group velocity dispersion (GVD) of the crystal. We show that planar second harmonic generation usefully serves to visualize and monitor precisely filamentation dynamics, allowing to accurately establish the position of nonlinear focus and to determine the nonlinear index of refraction using Marburger‘s law.

2. Material properties and experimental setup

The experiment was performed using near-infrared femtosecond pulses from a commercial optical parametric amplifier (Topas-C, Light Conversion), which was pumped by an amplified Ti:sapphire laser system (Spitfire-PRO, Newport-Spectra Physics) at a 500 Hz repetition rate. The experimental setup is schematically depicted in Fig. 1(a). The beam was focused using a $f = +100$ mm BaF_2 lens (L) into the front face of undoped unpoled polycrystalline SBN:61 ($Sr_{0.61}Ba_{0.39}Nb_2O_6$) sample with dimensions of $5 \times 5 \times 5$ mm.

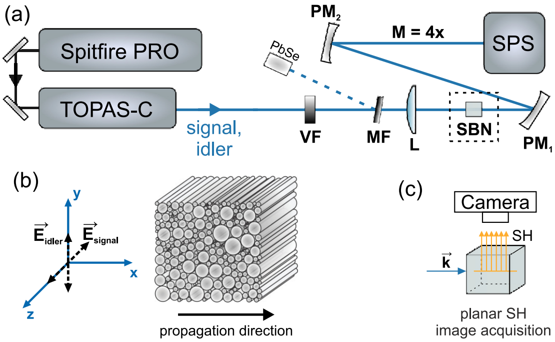

Fig. 1. (a) Experimental setup, see text for details. (b) Orientation of the crystal, its principal axes and pump polarization with respect to propagation direction. (c) Acquisition of planar SH images.

The input pulse energy was adjusted using a variable neutral density filter (VF) and measured with a calibrated PbSe photodetector using a reflection from a metallic filter (MF). The output spectra were recorded with a 4f system consisting of a pair of silver-coated parabolic mirrors PM_1 and PM_2, which were used to image the output face of the crystal onto the entrance slit of a home built scanning prism spectrometer (SPS) with Ge and InAsSb photodetectors, which allowed to perform spectral measurements in the 0.6 – 5.8 μm wavelength region.

In our study we used three different incident wavelengths of 1.2 μm, 2.0 μm and 2.4 μm, which fall into the normal, zero and anomalous GVD regions of the material, respectively. The focal spot sizes of the input beams and corresponding pulse durations were slightly different for the three chosen wavelengths and are listed in Table 1, which also presents the respective refraction indices and GVD coefficients of the crystal. The crystal orientation with respect to the propagation direction of the beam is depicted in Fig. 1(b). In this configuration, the input pulse with a wavelength of 1.2 μm (the signal wave of the optical parametric amplifier) had an extraordinary polarization, while the input pulses with wavelengths of 2.0 μm and 2.4 μm (the idler waves) had ordinary polarizations. Such crystal orientation ensured that second harmonic (SH) is emitted in the direction perpendicular to the incident beam [17]. Images of planar SH

Table 1. Summary of relevant input beam/pulse and material parameters. λ_p is the pump wavelength, τ is the pulse width, w_0 is the $1/e^2$ radius of the focal spot at the crystal input, n is the refractive index (note different polarizations), g is the GVD coefficient.

λ_p (μm)	1.2	2.0	2.4
polarization	e	o	o
τ (fs)	85	95	125
w_0 (μm)	36	54	53
n_0	2.216	2.211	2.198
g (fs^2/mm)	+243	-14	-180

radiation were taken using a Nikon D7200 DSLR camera mounted above the polished top side of SBN crystal, as schematically illustrated in Fig. 1(c).

3. Results and discussion

Large nonlinear index of refraction of SBN crystal, $n_2 = 52.4\times10^{-16}$ cm^2/W at 1064 nm [28], implies very low (0.14 MW) critical power for self-focusing at that wavelength; $P_{\rm cr} = 3.77\lambda^2/8\pi n_0 n_2$. Indeed, the onset of filamentation was experimentally detected with pump pulse energies less than 100 nJ and sub-MW peak powers: 32 nJ (0.35 MW) at 1.2 μm, 54 nJ (0.53 MW) at 2.0 μm and 74 nJ (0.56 MW) at 2.4 μm, as verified by the onset of spectral broadening and beam filamentation; the latter was visualized by the emergence of intense spot in the planar SH emission from the filament site.

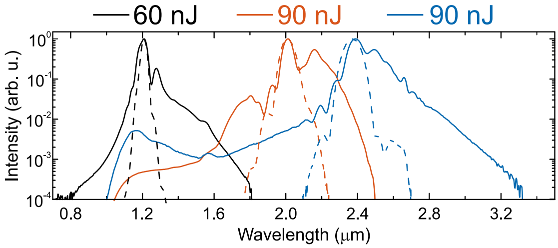

Fig. 2. Supercontinuum spectra generated in SBN using pump pulses with carrier wavelengths of 1.2 μm (black curve), 2.0 μm (red curve) and 2.4 μm (blue curve). The energies of the pump pulses are indicated on the top. The input spectra are depicted by dashed curves.

Figure 2 compares the SC spectra in polycrystalline SBN generated in the ranges of its normal, zero and anomalous GVD. The pump pulse energies were set slightly above the threshold energies for filamentation, where blue-shifted broadenings of the spectra saturate and no refocusing of the filament is observed. Smooth, more than an octave-spanning SC spectra in the wavelength ranges of 0.8 – 1.81 μm, 1.04 – 2.5 μm and 1.0 – 3.32 μm (defined at the 10^{-4} intensity level) were obtained using pump pulses with carrier wavelengths of 1.2 μm, 2.0 μm and 2.4 μm, respectively. These results affirm the general consideration that nonlinear polycrystalline materials as well as single crystals with a narrow energy bandgap, such as silicon and mixed thallous halides, usefully serve for the generation of infrared SC, see e.g. [29] for a review and [30–32] for more recent results.

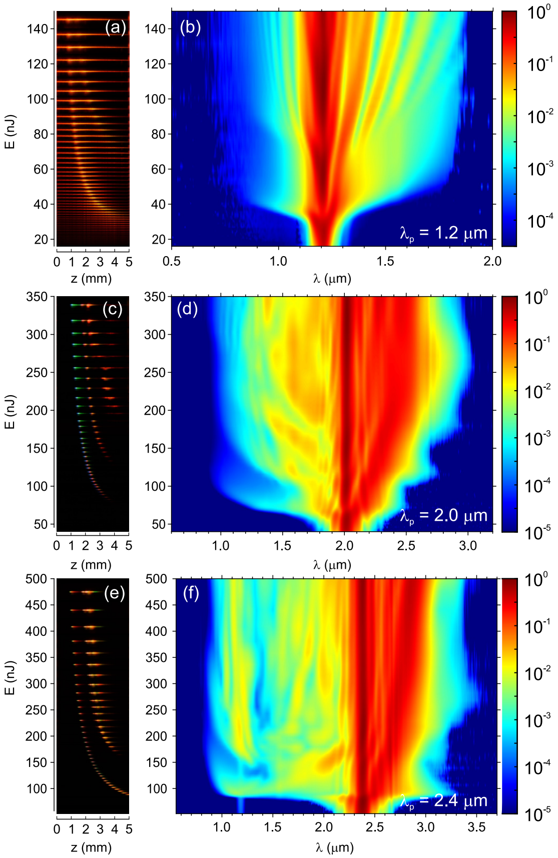

Fig. 3. (a,c,e) Composite images of SH traces and (b,d,f) related dynamics of spectral broadening as functions of the pump pulse energy in the cases of normal (1.2 μm), zero (2.0 μm) and anomalous (2.4 μm) GVD.

Figure 3 shows filamentation and SC generation dynamics in more detail by collation of the images of SH traces and related spectral evolutions as functions of the input pulse energy in the cases of normal, zero and anomalous GVD. The energy ranges for each input wavelength were chosen to preserve a single filament propagation regime and to avoid the occurrence of multiple filamentation. Planar SH generation in pollycrystaline SBN is a well known phenomenon occurring due to the random distribution of the needle-like domains, which provides a continuous set of reciprocal grating vectors that satisfy the phase matching conditions for a wide range of spectral components [10, 17]. The series of SH images depicted in Figs. 3(a), 3(c) and 3(e) reveal that such broadband SH emission closely follows the intensity distribution along the light filament and can be readily used to monitor filamentation dynamics similarly to a more common method of filament visualization based on filament-induced luminescence observed in various single crystals, see e.g. [33–35].

It is very clear that the occurrence of intense planar SH emission manifests the onset of filamentation, which is also justified by an explosive broadening of the spectrum. The most intense part of the SH trace maps the position of the nonlinear focus, which first appears at the end of the sample and thereafter shifts toward its input face as the energy of the pump pulse increases. The intensity variation along the SH trace also nicely captures filament refocusing at elevated pump pulse energy, which is indicated by the emergence of a secondary intensity peak in the SH trace which correlates with a secondary boost of spectral broadening and the occurrence of interference pattern in the SC spectrum, very clearly visible with 1.2 μm and somewhat less pronounced with 2.0 μm and 2.4 μm pump pulses.

To summarize the observed spectral dynamics presented in Fig. 3, the spectral broadening versus the input pulse energy shows several interesting features, which are quite general from the point of view of underlying physics. First, an apparent shrinking of the SC spectra (especially well-pronounced on the short wavelength side) is observed before the filament refocusing takes place in all investigated cases. This spectral shrinking is attributed to the defocusing and absorption of free electron plasma that push a large portion of the pulse energy out of the propagation axis after the first nonlinear focus, see [35] for details. Second, each refocusing cycle in the cases of zero (2.0 μm) and anomalous (2.4 μm) GVD precedes the constant red shift. Such spectral behavior was also observed in various nonlinear media (CaF_2 and LiF single crystals and fused silica, see [36]), and was attributed to the periodic breathing of the light bullet, i.e. the self-compressed pulse that emerges due to the interplay between self-phase modulation and anomalous GVD. The same consideration applies also to the case of zero GVD, where the pulse splitting takes place, and the spectrum of the trailing sub-pulse that is responsible for the red shift, falls into the range of anomalous GVD of the crystal.

Notice that no SH emission in the direction of filament propagation is detected, except in the case of 2.4 μm pumping, see Fig. 3(f), where a very weak SH emission centered at 1.2 μm is observed before the spectral broadening starts. Almost identical SC spectra and spectral dynamics versus the pump pulse energy (not shown here) were recorded with ordinarily polarized pump pulse at 1.2 μm and extraordinarily polarized pump pulses at 2.0 μm and 2.4 μm, i.e. when the crystal was rotated by 90° in the plane perpendicular to the beam propagation direction, setting needle-like domains vertically; please refer to Fig. 1(b).

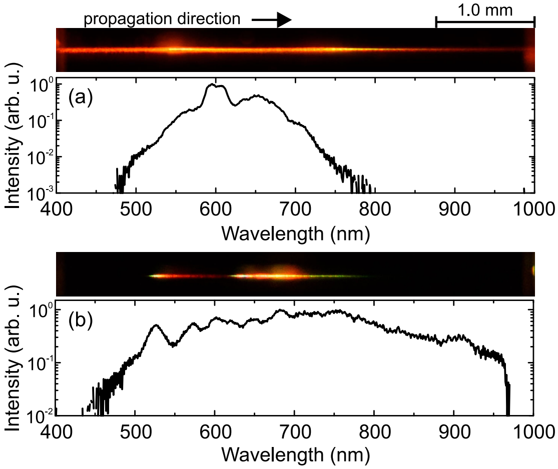

Fig. 4. Photographs of representative SH traces and SH spectra recorded with a fiber spectrometer using (a) 1.2 μm, 85 nJ and (b) 2.4 μm, 408 nJ pump pulses.

The SH traces produced by filamentation of the pulses with central wavelengths of 1.2 μm, 2.0 μm and 2.4 μm appear in different colors. Figure 4 compares the spectra of planar SH emissions produced by filamentation of 1.2 μm and 2.4 μm pulses and measured with a fiber spectrometer (Ocean Optics QE65000). Figure 4(a) shows the recorded SH spectrum produced with the pump wavelength of 1.2 μm. The SH spectrum spans the wavelength range from 480 to 800 nm and represents an almost exact replica of the entire SC spectrum with the peak spectral intensity at 600 nm, which is the second harmonic of the pump. With the pump wavelength of 2.4 μm, the SH spectrum covers the wavelength range from 460 nm to 970 nm, which is the long-wave detection limit of the spectrometer, see Fig. 4(b), attesting that such broadband SH emission is produced by frequency doubling of the blue-shifted part of the SC spectrum. An interesting variation of color along the SH trace indicates the propagation distances at which the particular spectral components of the SC have the highest intensities. This feature is particularly well pronounced in the case of 2.0 μm pumping, see Fig. 2(c). These spectral measurements demonstrate extremely wide, an octave-spanning conversion bandwidth of SH generation provided by random quasi phase matching.

Series of SH emission traces shown in Figs. 3(a), 3(c) and 3(e) were further exploited in order to determine the nonlinear refractive index of the material. In doing so, each SH trace was converted into greyscale and integrated along the height of the image. The position of the first intensity maximum (that appears closest to the input face of the crystal) was considered to be the nonlinear focal point. Thereafter the retrieved datasets of positions of the nonlinear foci versus the pump energy (power) for each pump wavelength were fitted using Marburger‘s empirical formula for the position of nonlinear focus [37]:

$$z_{\mathrm{sf}} = \frac{0.367\, z_R}{\sqrt{[(P/P_{\mathrm{cr}})^{1/2} - 0.852]^2 - 0.0219}}, \tag{1}$$

where $z_R = \pi n_0 w_0^2/\lambda$ is the Rayleigh (diffraction) length of the input Gaussian beam with a radius w_0, P is the power of the pump and P_{cr} is the critical power for self-focusing.

The results for the pump wavelengths of 1.2 μm, 2.0 μm and 2.4 μm are summarized in Fig. 5, which shows the retrieved positions of experimental nonlinear foci versus the pump pulse energy and power and the respective best fits using Eq.(1). The fitting procedure was performed taking the radii of input beams and pulse durations from Table 1. However, the best fits were obtained using the radii of the input beams as additional free parameters, yielding $1/e^2$ beam radii of 26 μm, 43 μm and 44 μm for the input beams with carrier wavelengths of 1.2 μm, 2.0 μm and 2.4 μm, respectively. These systematically smaller beam sizes may be attributed to a slightly elliptical shapes of the input beams and unknown amounts of the chirp of the input pulses, which both could slightly alter the position of the nonlinear focus [38]. The best fits yielded the following values of nonlinear refractive indexes: $44 \pm 7 \times 10^{-16}$ cm^2/W at 1.2 μm, $81 \pm 23 \times 10^{-16}$ cm^2/W at 2.0 μm and $100 \pm 15 \times 10^{-16}$ cm^2/W at 2.4 μm.

The obtained n_2 value at 1.2 μm compares favorably with the previously reported value of 52.4×10^{-16} cm^2/W at 1064 nm [28], however, much larger n_2 values obtained at 2.0 μm and 2.4 μm look quite surprising. Indeed, these large values appear in stark contrast with what can be expected from a general dispersion law of n_2, suggesting the maximum n_2 value around the edge of two photon absorption (~ 730 nm for SBN) and gradual decrease of n_2 toward longer wavelengths [28]. This result can not be explained by the contribution of the cascaded nonlinearity due to phase-mismatched SH generation, as the wavevector mismatch for any type of possible three-wave interaction, see [18], for the wavelengths of interest is always positive, so suggesting that the contribution of the cascaded nonlinearity to effective n_2 is negative. On the other hand, these large n_2 values are confirmed by very low beam powers for filamentation and SC generation thresholds determined experimentally for pump wavelengths of 2.0 μm and 2.4 μm.

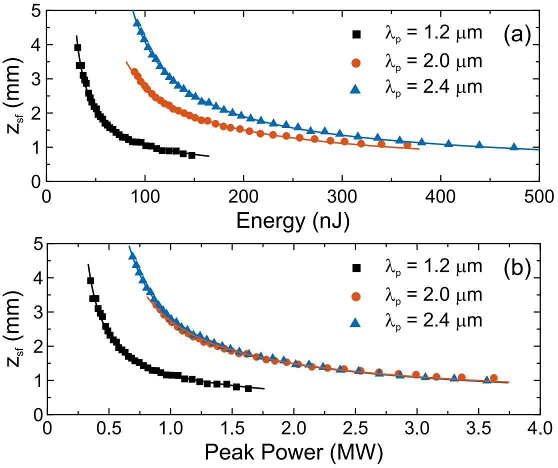

Fig. 5. (a) The positions of the nonlinear foci versus the pump pulse energy (dots) and the best fits using Marburger's formula (curves) for the pump wavelengths of 1.2 μm (black), 2.0 μm (red) and 2.4 μm (blue). (b) the same data represented in terms of a peak power and used for estimation of n_2.

4. Conclusions

In conclusion, we demonstrated that SBN crystal serves as an efficient nonlinear medium for SC generation in the infrared spectral range. More than an octave-spanning infrared SC spectra were produced with reasonably low pump energies (powers), in the ranges of normal, zero and anomalous GVD of the crystal. We also show that random quasi phase matching in polycrystalline SBN provides an extremely broad, octave-spanning bandwidth for planar SH generation. Moreover, we demonstrate that broadband planar SH emission precisely maps the intensity distribution along the filament of light, and so could be used to visualize the entire self-focusing and filamentation dynamics. This feature was exploited for determination of the nonlinear index of refraction of SBN at 1.2 μm, 2.0 μm and 2.4 μm.

Funding

This project has received funding from European Regional Development Fund (project No 1.2.2-LMT-K-718-02-0017) under grant agreement with the Research Council of Lithuania (LMTLT).

Disclosures

The authors declare no conflicts of interest.

References

1. M. Baudrier-Raybaut, R. Haidar, P. Kupecek, P. Lemasson, and E. Rosencher, "Random quasi-phase-matching in bulk polycrystalline isotropic nonlinear materials," Nature **432**, 374–376 (2004).
2. T. Kawamori, Q. Ru, and K. L. Vodopyanov, "Comprehensive model for randomly phase-matched frequency conversion in zinc-blende polycrystals and experimental results for ZnSe," Phys. Rev. Appl. **11**, 054015 (2019).
3. O. Mouawad, P. Béjot, F. Billard, P. Mathey, B. Kibler, F. Désévédavy, G. Gadret, J.-C. Jules, O. Faucher, and F. Smektala, "Filament-induced visible-to-mid-ir supercontinuum in a ZnSe crystal: Towards multi-octave supercontinuum absorption spectroscopy," Opt. Mater. **60**, 355–358 (2016).

4. R. Šuminas, G. Tamošauskas, G. Valiulis, V. Jukna, A. Couairon, and A. Dubietis, "Multi-octave spanning nonlinear interactions induced by femtosecond filamentation in polycrystalline ZnSe," Appl. Phys. Lett. **110**, 241106 (2017).
5. G. M. Archipovaite, S. Petit, J.-C. Delagnes, and E. Cormier, "100 khz Yb-fiber laser pumped 3 μm optical parametric amplifier for probing solid-state systems in the strong field regime," Opt. Lett. **42**, 891–894 (2017).
6. R. Šuminas, A. Marcinkevičiūtė, G. Tamošauskas, and A. Dubietis, "Even and odd harmonics-enhanced supercontinuum generation in zinc-blende semiconductors," J. Opt. Soc. Am. B **36**, A22–A27 (2019).
7. K. Werner, M. G. Hastings, A. Schweinsberg, B. L. Wilmer, D. Austin, C. M. Wolfe, M. Kolesik, T. R. Ensley, L. Vanderhoef, A. Valenzuela, and E. Chowdhury, "Ultrafast mid-infrared high harmonic and supercontinuum generation with n_2 characterization in zinc selenide," Opt. Express **27**, 2867–2885 (2019).
8. C. B. Marble, S. P. OâĂŹConnor, D. T. Nodurft, A. W. Wharmby, and V. V. Yakovlev, "Eye safety implications of high harmonic generation in zinc selenide," Opt. Express **27**, 2828–2836 (2019).
9. S. Vasilyev, I. Moskalev, V. Smolski, J. Peppers, M. Mirov, A. Muraviev, K. Vodopyanov, S. Mirov, and V. Gapontsev, "Multi-octave visible to long-wave IR femtosecond continuum generated in Cr:ZnS-GaSe tandem," Opt. Express **27**, 16405–16413 (2019).
10. P. Molina, M. de la O. Ramirez, and L. E. Bausa, "Strontium barium niobate as a multifunctional two-dimensional nonlinear "photonic glass"," Adv. Funct. Mater. **18**, 709–715 (2008).
11. M. J. Weber, *Handbook of optical materials* (London: CRC press, 2003).
12. T. Woike, T. Granzow, U. Dörfler, C. Poetsch, M. Wöhlecke, and R. Pankrath, "Refractive indices of congruently melting $Sr_{0.61}Ba_{0.39}Nb_2O_6$," Phys. Status Solidi A **186**, R13–R15 (2001).
13. K. Terabe, S. Takekawa, M. Nakamura, K. Kitamura, S. Higuchi, Y. Gotoh, and A. Gruverman, "Imaging and engineering the nanoscale-domain structure of a $Sr_{0.61}Ba_{0.39}Nb_2O_6$ crystal using a scanning force microscope," Appl. Phys. Lett. **81**, 2044–2046 (2002).
14. E. Y. Morozov, A. A. Kaminskii, A. S. Chirkin, and D. B. Yusupov, "Second optical harmonic generation in nonlinear crystals with a disordered domain structure," JETP Lett. **73**, 647–650 (2001).
15. A. R. Tunyagi, M. Ulex, and K. Betzler, "Noncollinear optical frequency doubling in strontium barium niobate," Phys. Rev. Let. **90**, 243901 (2003).
16. V. Roppo, W. Wang, K. Kalinowski, Y. Kong, C. Cojocaru, J. Trull, R. Vilaseca, M. Scalora, W. Krolikowski, and Y. Kivshar, "The role of ferroelectric domain structure in second harmonic generation in random quadratic media," Opt. Express **18**, 4012–4022 (2010).
17. R. Fischer, S. Saltiel, D. Neshev, W. Krolikowski, and Y. S. Kivshar, "Broadband femtosecond frequency doubling in random media," Appl. Phys. Lett. **89**, 191105 (2006).
18. L. Mateos, P. Molina, J. F. Galisteo-López, C. López, L. E. Bausá, and M. O. Ramírez, "Ultrabroadband generation of multiple concurrent nonlinear coherent interactions in random quadratic media," Appl. Phys. Lett. **103**, 101101 (2013).
19. W. Wang, V. Roppo, K. Kalinowski, Y. Kong, D. Neshev, C. Cojocaru, J. Trull, R. Vilaseca, K. Staliunas, W. Krolikowski, S. M. Saltiel, and Y. Kivshar, "Third-harmonic generation via broadband cascading in disordered quadratic nonlinear media," Opt. Express **17**, 20117–20123 (2009).
20. W. Wang, K. Kalinowski, V. Roppo, Y. Sheng, K. Koynov, Y. Kong, C. Cojocaru, J. Trull, R. Vilaseca, and W. Krolikowski, "Second-and third-harmonic parametric scattering in disordered quadratic media," J. Phys. B **43**, 215404 (2010).
21. F. J. Rodríguez, C. Yao, J. L. Domínguez-Juárez, J. Bravo-Abad, and J. Martorell, "Observation of speckle pattern formation in transparent nonlinear random media," Opt. Lett. **36**, 1347–1349 (2011).
22. C. Yao, F. J. Rodriguez, and J. Martorell, "Controlling the diffused nonlinear light generated in random materials," Opt. Lett. **37**, 1676–1678 (2012).
23. C. Hermann-Avigliano, I. Salinas, D. Rivas, B. Real, A. Mančić, C. Mejía-Cortés, A. Maluckov, and R. A. Vicencio, "Spatial rogue waves in photorefractive SBN crystals," Opt. Lett. **44**, 2807–2810 (2019).
24. M. Ayoub, M. Paßlick, J. Imbrock, and C. Denz, "Controlling the effective second-order susceptibility in random quadratic media," Opt. Express **23**, 33980–33991 (2015).
25. J. Trull, S. Saltiel, V. Roppo, C. Cojocaru, D. Dumay, W. Krolikowski, D. Neshev, R. Vilaseca, K. Staliunas, and Y. S. Kivshar, "Characterization of femtosecond pulses via transverse second-harmonic generation in random nonlinear media," Appl. Phys. B **95**, 609–615 (2009).
26. J. Trull, I. Sola, B. Wang, A. Parra, W. Krolikowski, Y. Sheng, R. Vilaseca, and C. Cojocaru, "Ultrashort pulse chirp measurement via transverse second-harmonic generation in strontium barium niobate crystal," Appl. Phys. Lett. **106**, 221108 (2015).
27. B. Wang, C. Cojocaru, W. Krolikowski, Y. Sheng, and J. Trull, "Transverse single-shot cross-correlation scheme for laser pulse temporal measurement via planar second harmonic generation," Opt. Express **24**, 22210–22218 (2016).
28. M. Sheik-Bahae, D. C. Hutchings, D. J. Hagan, and E. W. Van Stryland, "Dispersion of bound electron nonlinear refraction in solids," IEEE J. Quantum Electron. **27**, 1296–1309 (1991).
29. A. Dubietis, G. Tamošauskas, R. Šuminas, V. Jukna, and A. Couairon, "Ultrafast supercontinuum generation in bulk condensed media," Lith. J. Phys. **57**, 113–157 (2017).
30. A. Marcinkevičiūtė, V. Jukna, R. Šuminas, N. Garejev, G. Tamošauskas, and A. Dubietis, "Femtosecond filamentation and supercontinuum generation in bulk silicon," Opt. Lett. **44**, 1343–1346 (2019).
31. A. Marcinkevičiūtė, G. Tamošauskas, and A. Dubietis, "Supercontinuum generation in mixed thallous halides KRS-5

and KRS-6," Opt. Mater. **78**, 339–344 (2018).

32. K. Liu, H. Liang, S. Qu, W. Li, X. Zou, Y. Zhang, and Q. J. Wang, "High-energy mid-infrared intrapulse difference-frequency generation with 5.3% conversion efficiency driven at 3 μm," Opt. Express **27**, 37706–37713 (2019).
33. A. Dharmadhikari, J. Dharmadhikari, and D. Mathur, "Visualization of focusing–refocusing cycles during filamentation in BaF_2," Appl. Phys. B **94**, 259–263 (2009).
34. D. Kudarauskas, G. Tamošauskas, M. Vengris, and A. Dubietis, "Filament-induced luminescence and supercontinuum generation in undoped, Yb-doped, and Nd-doped YAG crystals," Appl. Phys. Lett. **112**, 041103 (2018).
35. V. Jukna, N. Garejev, G. Tamošauskas, and A. Dubietis, "Role of external focusing geometry in supercontinuum generation in bulk solid-state media," J. Opt. Soc. Am. B **36**, A54–A60 (2019).
36. N. Garejev, G. Tamošauskas, and A. Dubietis, "Comparative study of multioctave supercontinuum generation in fused silica, YAG, and LiF in the range of anomalous group velocity dispersion," J. Opt. Soc. Am. B **34**, 88–94 (2017).
37. J. Marburger, "Self-focusing: theory," Prog. Quantum Electron. **4**, 35–110 (1975).
38. A. Couairon, E. Brambilla, T. Corti, D. Majus, O. de. J. Ramírez-Góngora, and M. Kolesik, "PractitionerâĂŹs guide to laser pulse propagation models and simulation," Eur. Phys. J. Spec. Top. **199**, 5–76 (2011).

A5

FEMTOSECOND FILAMENTATION AND SUPERCONTINUUM GENERATION IN BULK SILICON

A. Marcinkevičiūtė, V. Jukna, R. Šuminas, N. Garejev,
G. Tamošauskas, A. Dubietis

Opt. Lett. **44**(6), 1343–1346 (2019)

Femtosecond filamentation and supercontinuum generation in bulk silicon

A. Marcinkevičiūtė , V. Jukna , R. Šuminas , N. Garejev , G. Tamošauskas , and A. Dubietis*

Laser Research Center, Vilnius University, Saulėtekio Avenue 10, LT-10223 Vilnius, Lithuania
*Corresponding author: audrius.dubietis@ff.vu.lt

Compiled February 7, 2019

We experimentally study filamentation and supercontinuum generation in bulk silicon crystal using femtosecond mid-infrared pulses with carrier wavelengths in the range of $3.25 - 4.7$ μm, in the presence of three, four and five photon absorption. Spectral measurements show a fairly stable blue-shifted cut-off in the $2.5 - 2.7$ μm range and gradual increase of the long-wave extent with increasing wavelength of the incident pulses, eventually yielding an octave-spanning supercontinuum, covering the wavelength range from 2.5 to 5.8 μm with the input pulses at 4.7 μm. The recorded spatiotemporal intensity distributions of a single filament revealed pulse splitting after the nonlinear focus, in line with the pulse splitting-based filamentation scenario inherent to normally dispersive dielectric nonlinear media.

http://dx.doi.org/10.1364/ao.XX.XXXXXX

Since its discovery in 1995 [1], femtosecond filamentation in bulk transparent materials attracts a great deal of fundamental and practical interest. Femtosecond filamentation is a universal phenomenon that shares common features regardless of the physical state (solid, liquid or gas) of the nonlinear medium. The underlying physics of femtosecond filamentation is generally complex, as it involves an intricate coupling between spatial and temporal effects: self-focusing, self-phase modulation, multiphoton absorption/ionization, generation of free electron plasma, diffraction and material dispersion [2]. As a result, in the space domain, the beam reshapes into a narrow light string, that is able to propagate over extended distances. In the time domain, the pulse undergoes either splitting if the material group velocity dispersion (GVD) is normal or compression in the range of anomalous GVD. These temporal transformations result in pulse front steepening, which in turn gives rise to a dramatic broadening of the spectrum, termed supercontinuum (SC) generation [3]. So far, most of the knowledge on the topic comes from the studies of filamentation in transparent dielectric materials [2]. As compared to solid-state dielectrics, semiconductors possess smaller bandgaps, but at the same time much larger cubic nonlinearities, considerable free carrier absorption, etc., which eventually may suggest a different balance between the relevant governing effects leading to filamentation and spectral broadening. The feasibility of semiconductor materials to produce an appreciable spectral broadening and SC generation in the mid-infrared was experimentally demonstrated with picosecond laser pulses more than 30 years ago [4]. By virtue of the optical parametric amplification and frequency down-conversion techniques, which made femtosecond and even few optical cycle pulses in the mid-infrared routinely available, semiconductor crystals are currently receiving attention as interesting nonlinear materials for hosting filamentation phenomena. To date, femtosecond filamentation, spectral broadening, and eventually SC generation was studied in bulk semiconductor crystals, such as GaAs [5–8], ZnS [9, 10] and ZnSe [10–14], unveiling filamentation scenarios that lead to pulse compression and multioctave SC generation, that provides a broad coverage of mid-infrared wavelengths.

Owing to cubic crystal symmetry and very large nonlinearity [15, 16], silicon is identified as one of the most important semiconductor materials in the rapidly emerging field of nonlinear photonics for applications in the mid-infrared spectral region [17–19]. More than octave-spanning femtosecond SC generation was reported in various geometries and modifications of highly nonlinear dispersion-engineered silicon waveguides, see e.g. [20–22] and soliton compression was observed in silicon photonic crystals [23]. However, the investigations of nonlinear propagation of femtosecond laser pulses in bulk silicon have been limited to the studies of plasma generation, free carrier dynamics, energy deposition and material modification effects with near-infrared wavelengths, mostly in the regime of two photon absorption [24–28].

In this Letter, we report on filamentation and supercontinuum generation in bulk undoped silicon sample with femtosecond mid-infrared laser pulses. Relevant filamentation parameters: energy thresholds, dependence of the SC spectral width on the incident wavelength and spatiotemporal intensity distributions showing pulse splitting, have been measured with the incident wavelengths of 3.25, 3.6, 4.0 and 4.7 μm in the regimes of single and multiple filamentation.

The experimental setup is schematically depicted in Fig. 1. The mid-infrared pulses were produced by the difference fre-

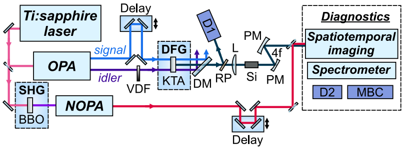

Fig. 1. Schematic of the experimental setup. See text for details.

Table 1. Relevant linear and nonlinear parameters of silicon at the wavelengths of interest. n_0 and g are the linear refractive index and the GVD coefficient, respectively; data from [17]. $K = \langle E_g/\hbar\omega_0 \rangle + 1$ is the order of multiphoton absorption, where $E_g = 1.12$ eV is the bandgap of silicon and $\hbar\omega_0$ is the photon energy. β^K and n_2 are the multiphoton absorption coefficient and the nonlinear refractive index, respectively; data from [15]. $P_{\mathrm{cr}} = 0.15\lambda^2/n_0 n_2$ is the critical power for self-focusing.

λ (μm)	3.25	3.60	4.00	4.70
n_0	3.441	3.438	3.436	3.433
g (fs^2/mm)	+494	+444	+398	+337
K	3	4	4	5
β^K (cm^{2K-3}/GW^{K-1})	2×10^{-3}	3.5×10^{-4}	3×10^{-5}	8×10^{-7}
n_2 ($\times 10^{-16}$ cm^2/W)	270	270	270	270
P_{cr} (MW)	0.17	0.21	0.26	0.36

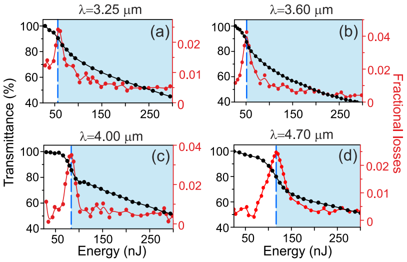

Fig. 2. Experimentally measured nonlinear transmittance and evaluated fractional losses (bottom row) of a 6.4 mm thick silicon sample versus the input pulse energy. The energies corresponding to distinct maxima of fractional losses indicate filamentation thresholds.

quency generation (DFG) between the signal and idler outputs of the Ti:sapphire laser-pumped optical parametric amplifier OPA (Topas-Prime, Light Conversion Ltd.) in a 1 mm-thick KTA crystal. The residual signal and idler radiation was filtered out by a dichroic mirror (DM), and the DFG beam was focused with a BaF$_2$ lens L ($f = +100$ mm) into the focal spot of $70 - 85$ μm FWHM diameter (depending on the wavelength), which was located on the input face of an uncoated silicon sample (Si) of 6.4 mm thickness. The pulse energy was varied using a variable density metal-coated filter VDF (NDL-25C-2, Thorlabs Inc.), which was inserted in the path of the idler wave. The nonlinear transmittance measurements were performed with calibrated detectors D1 (PbSe) and D2 (pyroelectric), used to simultaneously monitor the incident (taken as a reflection from thin ZnSe plate, RP) and transmitted energies, respectively. The intensity profile of the output beam was measured by imaging the output face of the sample with 4× magnification by means of a pair of Ag-coated parabolic mirrors (PM) in a $4f$ configuration onto a micro-bolometric camera MBC (WinCamD, FIR2-16-HR, pixel size 17 μm). The spectral measurements were performed using a home-built scanning prism spectrometer with InAsSb detector, providing an effective detection range of $0.8 - 5.8$ μm. The spatiotemporal profiles of the filament were measured by means of spatiotemporal imaging technique based on recording spatially resolved cross-correlation function via sum-frequency generation between the object pulse and a 27 fs reference pulse at 0.72 μm from a second harmonic (SHG) pumped non-collinear optical parametric amplifier NOPA (Topas-White, Light Conversion Ltd.). For this purpose we used type I phase matching BBO crystal of 20 μm thickness, which provided phase matching and reasonable transparency for the mid-infrared wavelengths of interest [29]. The spatiotemporal intensity distribution of the filament was reconstructed by merging a series of cross-correlation images recorded by varying the time delay between the object and the reference pulses. The central wavelengths of the input pulses were chosen so as to access filamentation regimes in the presence of three (3.25 μm), four (3.6 and 4.0 μm) and five (4.7 μm) photon absorption, respectively, see Table 1. The measured durations of the input pulses at these wavelengths were 57, 60, 126 and 106 fs, respectively. Almost twice longer pulses at the latter two wavelengths were caused by the increased group velocity mismatch between interacting pulses in the DFG crystal.

Figure 2 shows the measured nonlinear transmittance of a 6.4 mm-thick silicon sample versus the input pulse energy for the chosen input pulse wavelengths of 3.25, 3.6, 4.0 and 4.7 μm. Beside multiphoton absorption, the nonlinear losses are also contributed by the absorption of free carriers via inverse Bremsstrahlung that in turn increases the density of the free carriers via avalanche ionization and is most efficient in the vicinity of the nonlinear focus. Initial free carriers may also contribute to the nonlinear losses, however, in undoped silicon at room temperature their concentration is very low, 9.7×10^{-9} cm^{-3} [30], and thus their effect on the energy losses is expected to be negligibly small. Superimposed on the transmittance plots are the evaluated fractional losses ($-dT/dE$), where T and E are the transmittance and pulse energy, respectively. As the rate of the nonlinear absorption peaks at the nonlinear focus of the beam, where the highest intensity is achieved, the distinct maxima of the fractional losses indicate that the nonlinear focus is located right at the output face of the sample, so readily providing the threshold energies for filament formation. Owing to large nonlinear index of refraction, $n_2 = 2.7 \times 10^{-14}$ cm^2/W, which is constant in the wavelength range of interest [15], the measured filamentation thresholds were remarkably low: 55 nJ at the incident wavelength of 3.25 μm, 50 nJ at 3.6 μm, 85 nJ at 4.0 μm and 110 nJ at 4.7 μm. Here and later in text the input pulse energies

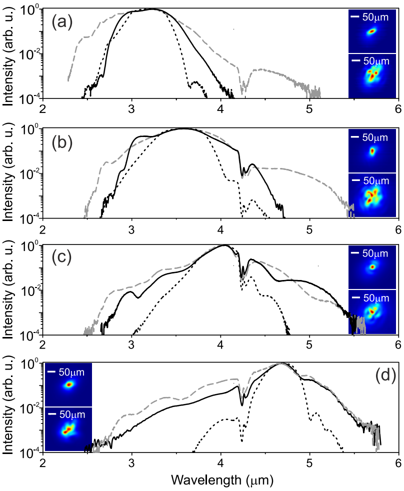

Fig. 3. SC spectra at the output of a 6.4 mm-thick silicon sample, measured in the regimes of single (black solid curves) and multiple (gray dashed curves) filamentation. The input pulse spectra are depicted by dotted curves. Insets show the near-field fluence profiles of single (top insets on each panel) and multiple (bottom insets) filaments.

are given by subtracting Fresnel losses from the front face of the sample.

Figure 3 shows the SC spectra produced by filamentation of the pulses with carrier wavelengths of 3.25, 3.6, 4.0 and 4.7 μm. The black solid curves show the SC spectra recorded with the input pulse energies of 160, 170, 185 and 210 nJ, respectively, which were set to produce a stable blue-shifted cut-off and a single filament at the sample output, as illustrated in the insets. The generation of broader SC spectra with increasing the input wavelength confirms the general trend of the increase of the spectral blue shift from the carrier wavelength with increasing the order of multiphoton absorption from 3 to 5 [31]. The measured blue-shifts of the SC spectra lie in the range of $2.5-2.7$ μm and are almost regardless of the input pulse wavelength, so confirming that the main factor that limits the SC cut-off on the short-wave side is the material GVD [32]. This also explains why the SC spectra generated with shorter wavelengths (3.25 and 3.6 μm) are basically red-shifted. Therefore these results suggest that the spectral extent of the SC in semiconductor crystals is defined by the same limiting factors as in dielectrics. The broadest SC spectrum covering the $2.5-5.8$ μm wavelength range (at the 10^{-4} intensity level), whose width corresponds to more than an optical octave, is produced with the input pulses at 4.7 μm. Also notice a distinct signature of atmospheric CO_2 absorption around 4.25 μm that is clearly visible in all SC spectra. The general trends of the spectral broadening were maintained in the multiple filamentation regime. The gray dashed curves depict the SC spectra recorded with elevated input pulse energies (625 nJ at 3.25 μm, 900 nJ at 3.6 μm, 690 nJ at 4.0 μm and 850 nJ at 4.7 μm). With the input wavelengths of 3.25 and 3.6 μm, slightly broader SC spectra with larger red shifts were generated, whereas the SC spectra produced by longer wavelengths were essentially of the same width, as produced by a single filament.

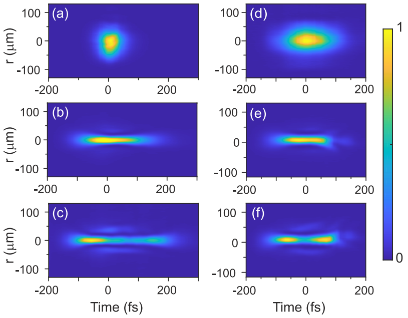

Fig. 4. Spatiotemporal intensity distributions of the input and output wave packets at 3.6 μm (left column) and 4.7 μm (right column), recorded with the input pulse energies slightly below and slightly above filamentation thresholds.

Figure 4 presents the spatiotemporal intensity distributions of the single filaments with carrier wavelengths of 3.6 and 4.7 μm, which were measured by varying the input pulse energy around the threshold values for filamentation (50 and 110 nJ, respectively). Since the sample length was fixed, such energy variation allowed capturing the spatiotemporal profiles of the wave packet virtually before and after the nonlinear focus. The left column of Fig. 4 shows how the incident Gaussian-shaped (in space and time) pulse with a duration of 60 fs and a central wavelength of 3.6 μm [Fig. 4(a)] shrinks in the spatial dimension due to self-focusing, while approaching the nonlinear focus (the input pulse energy 45 nJ), as depicted in Fig 4(b). At the same time, the pulse experiences broadening in time due to material GVD (the calculated dispersion length of 60 fs pulse at 3.6 μm is $\sim$ 3 mm) as well as due to four photon absorption that acts mainly on the pulse top. Figure 4(c) presents the spatiotemporal intensity distribution of the wave packet after it passes the nonlinear focus (the input pulse energy 55 nJ), showing splitting of the pulse on the propagation axis ($r=0$) that is accompanied by formation of a ring-like structure in the central part of the pulse, seen as elongated stripes parallel to the propagation axis if projected in the r,t plane. The recorded transformations are very much in line with spatiotemporal dynamics of femtosecond filaments in normally dispersive dielectric materials, see e.g. [33]. Qualitatively very similar spatiotemporal transformations were captured with the input pulses having a duration of 106 fs and a central wavelength of 4.7 μm, whose spatiotemporal intensity distribution is shown in Fig. 4(d). The input pulse energies of 100 and 130 nJ were used for recording the representative spatiotemporal intensity distributions of the wave packet before and after the nonlinear focus, respectively. In the present case, the dispersive broadening of the pulse before the nonlinear focus was much smaller due to longer input pulse duration and lower material dispersion (the calculated dispersion length of 106 fs pulse at 4.7 μm is $\sim$ 12 mm). On the other hand, the effects related to filament-induced plasma become more pronounced as the cross-section for inverse Bremsstrahlung scales as λ^2 [34]. Before the nonlinear focus, the wave packet develops a faint conical tail, seen as V-shaped structure in the r,t plane in Fig. 4(e) that is attributed to plasma absorption and defocusing of the trailing part of the pulse. The conical tail persists also after the nonlinear focus, where the pulse splitting occurs, as shown in Fig. 4(f). Notice that these features are only barely detectable in Figs. 4(b) and (c).

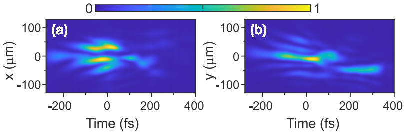

Fig. 5. Central cross-sections of the spatiotemporal intensity distributions of multiple filaments in the (a) x-t and (b) y-t planes, produced by self-focusing of 60 fs, 900 nJ input pulses at 3.6 μm.

Figure 5 shows the central cross-sections of the spatiotemporal intensity distributions of multiple filaments in the x,t and y,t planes. Here multiple filaments were produced by launching 60 fs, 3.6 μm pulses with an energy of 900 nJ. The images show that multiple filamentation yields a complex spatiotemporal profile, although some relevant details, such as pulse splitting in the individual filaments could be easily resolved. The interactions between the adjacent filaments result in an occurrence of skewed structures in the entire space-time domain. These complex spatiotemporal intensity patterns suggest that an extra spectral broadening that is measured in the regime of multiple filamentation, see Fig. 3, is achieved at the cost of loss of spatial and temporal coherence. As a final note, we should mention that no optical damage of silicon sample was observed while performing the experiments at 1 kHz repetition rate.

In conclusion, we detected that the energy thresholds to observe filamentation phenomena in bulk silicon with femtosecond mid-infrared pulses, are generally below 100 nJ. Octave-spanning SC spectra were produced with the input wavelengths of 4.0 and 4.7 μm, in the presence of four and five photon absorption, respectively. Our study revealed that the key physical effects and the basic features of femtosecond filamentation in semiconductors, such as pulse splitting in the range of normal GVD, and the limiting factors that determine the SC spectral extent (the order of multiphoton absorption and material GVD) are essentially identical to those in dielectrics. It was also shown that free carrier absorption does not alter the filamentation dynamics, so supporting the general conclusion of [15] that nonlinear propagation of very short, femtosecond pulses in silicon is less affected by free carriers. Overall, our results suggest that bulk silicon is an attractive nonlinear material which may readily serve for the generation of an octave-spanning SC in the mid-infrared.

This research was funded by the European Regional Development Fund and the Research Council of Lithuania, grant No. 01.2.2-LMT-K-718.

REFERENCES

1. A. Braun, G. Korn, X. Liu, D. Du, J. Squier, and G. Mourou, Opt. Lett. **20**, 73 (1995).
2. A. Couairon and A. Mysyrowicz, Phys. Rep. **441**, 47 (2007).
3. A. Dubietis, G. Tamošauskas, R. Šuminas, V. Jukna, and A. Couairon, Lith. J. Phys. **57**, 113 (2017).
4. P. B. Corkum, P. P. Ho, R. R. Alfano, and J. T. Manassah, Opt. Lett. **10**, 624 (1985).
5. S. Ashihara and Y. Kawahara, Opt. Lett. **34**, 3839 (2009).
6. A. A. Lanin, A. A. Voronin, E. A. Stepanov, A. B. Fedotov, and A. M. Zheltikov, Opt. Lett. **39**, 6430 (2014).
7. A. A. Lanin, A. A. Voronin, E. A. Stepanov, A. B. Fedotov, and A. M. Zheltikov, Opt. Lett. **40**, 974 (2015).
8. E. A. Stepanov, A. A. Lanin, A. A. Voronin, A. B. Fedotov, and A. M. Zheltikov, Phys. Rev. Lett. **117**, 043901 (2016).
9. H. Liang, P. Krogen, R. Grynko, O. Novak, C.-L. Chang, G. J. Stein, D. Weerawarne, B. Shim, F. X. Kärtner, and K.-H. Hong, Opt. Lett. **40**, 1069 (2015).
10. R. Šuminas, A. Marcinkevičiūtė, G. Tamošauskas, and A. Dubietis, J. Opt. Soc. Am. B **36**, A22 (2019).
11. M. Durand, A. Houard, K. Lim, A. Durécu, O. Vasseur, and M. Richardson, Opt. Express **22**, 5852 (2014).
12. O. Mouawad, P. Béjot, F. Billard, P. Mathey, B. Kibler, F. Désévédavy, G. Gadret, J.-C. Jules, O. Faucher, and F. Smektala, Opt. Mater. **60**, 355 (2016).
13. R. Šuminas, G. Tamošauskas, N. Garejev, V. Jukna, A. Couairon, and A. Dubietis, Appl. Phys. Lett. **110**, 241106 (2017).
14. R. I. Grynko, G. C. Nagar, and B. Shim, Phys. Rev. A **98**, 023844 (2018).
15. X. Gai, Y. Yu, B. Kuyken, P. Ma, S. J. Madden, J. V. Campenhout, P. Verheyen, G. Roelkens, R. Baets, and B. Luther-Davies, Laser Photon. Rev. **7**, 1054 (2013).
16. T. Wang, N. Venkatram, J. Gosciniak, Y. Cui, G. Qian, W. Ji, and D. T. H. Tan, Opt. Express **21**, 32192 (2013).
17. J. Leuthold, C. Koos, and W. Freude, Nat. Photon. **4**, 535 (2010).
18. M. Borghi, C. Castellan, S. Signorini, A. Trenti, and L. Pavesi, J. Opt. **19**, 093002 (2017).
19. Y. Zou, S. Chakravarty, C.-J. Chung, X. Xu, and R. T. Chen, Photon. Res. **6**, 254 (2018).
20. R. K. W. Lau, M. R. E. Lamont, A. G. Griffith, Y. Okawachi, M. Lipson, and A. L. Gaeta, Opt. Lett. **39**, 4518 (2014).
21. B. Kuyken, T. Ideguchi, S. Holzner, M. Yan, T. W. Hänsch, J. Van Campenhout, P. Verheyen, S. Coen, F. Leo, R. Baets, G. Roelkens, and N. Picqué, Nat. Commun. **6**, 6310 (2015).
22. N. Singh, D. D. Hudson, Y. Yu, C. Grillet, S. D. Jackson, A. Casas-Bedoya, A. Read, P. Atanackovic, S. G. Duvall, S. Palomba, B. Luther-Davies, S. Madden, D. J. Moss, and B. J. Eggleton, Optica **2**, 797 (2015).
23. A. Blanco-Redondo, C. Husko, D. Eades, Y. Zhang, J. Li, T. F. Krauss, and B. J. Eggleton, Nat. Commun. **5**, 3160 (2014).
24. V. V. Kononenko, V. V. Konov, and E. M. Dianov, Opt. Lett. **37**, 3369 (2012).
25. A. Mouskeftaras, A. V. Rode, R. Clady, M. Sentis, O. Utéza, and D. Grojo, Appl. Phys. Lett. **105**, 191103 (2014).
26. E. V. Zavedeev, V. V. Kononenko, and V. I. Konov, Laser Phys. **26**, 016101 (2016).
27. A. Mouskeftaras, M. Chanal, M. Chambonneau, R. Clady, O. Utéza, and D. Grojo, Appl. Phys. Lett. **108**, 041107 (2016).
28. M. Chanal, V. Yu. Fedorov, M. Chambonneau, R. Clady, S. Tzortzakis, and D. Grojo, Nat. Commun. **8**, 773 (2017).
29. G. Tamošauskas, G. Beresnevičius, D. Gadonas, and A. Dubietis, Opt. Mater. Express **8**, 1410 (2018).
30. K. Misiakos and D. Tsamakis, J. Appl. Phys. **74**, 3293 (1993).
31. A. Brodeur and S. L. Chin, Phys. Rev. Lett. **80**, 4406 (1998).
32. M. Kolesik, G. Katona, J. V. Moloney, and E. M. Wright, Phys. Rev. Lett. **91**, 043905 (2003).
33. A. Jarnac, G. Tamošauskas, D. Majus, A. Houard, A. Mysyrowicz, A. Couairon, and A. Dubietis, Phys. Rev. A **89**, 033809 (2014).
34. E. Yablonovitch and N. Bloembergen, Phys. Rev. Lett. **29**, 907 (1972).

REFERENCES

1. A. Braun, G. Korn, X. Liu, D. Du, J. Squier, and G. Mourou, “Self-channeling of high-peak-power femtosecond laser pulses in air,” Opt. Lett. **20**, 73–75 (1995).
2. A. Couairon and A. Mysyrowicz, “Femtosecond filamentation in transparent media,” Phys. Rep. **441**, 47–190 (2007).
3. A. Dubietis, G. Tamošauskas, R. Šuminas, V. Jukna, and A. Couairon, “Ultrafast supercontinuum generation in bulk condensed media,” Lith. J. Phys. **57**, 113–157 (2017).
4. P. B. Corkum, P. P. Ho, R. R. Alfano, and J. T. Manassah, “Generation of infrared supercontinuum covering $3 - 14\ \mu$m in dielectrics and semiconductors,” Opt. Lett. **10**, 624–626 (1985).
5. S. Ashihara and Y. Kawahara, “Spectral broadening of mid-infrared femtosecond pulses in GaAs,” Opt. Lett. **34**, 3839–3841 (2009).
6. A. A. Lanin, A. A. Voronin, E. A. Stepanov, A. B. Fedotov, and A. M. Zheltikov, “Frequency-tunable sub-two-cycle 60-MW-peak-power free-space waveforms in the mid-infrared,” Opt. Lett. **39**, 6430–6433 (2014).
7. A. A. Lanin, A. A. Voronin, E. A. Stepanov, A. B. Fedotov, and A. M. Zheltikov, “Multioctave, $3 - 18\ \mu$m sub-two-cycle supercontinua from self-compressing, self-focusing soliton transients in a solid,” Opt. Lett. **40**, 974–977 (2015).
8. E. A. Stepanov, A. A. Lanin, A. A. Voronin, A. B. Fedotov, and A. M. Zheltikov, “Solid-state source of subcycle pulses in the midinfrared,” Phys. Rev. Lett. **117**, 043901 (2016).
9. H. Liang, P. Krogen, R. Grynko, O. Novak, C.-L. Chang, G. J. Stein, D. Weerawarne, B. Shim, F. X. Kärtner, and K.-H. Hong, “Three-octave-spanning supercontinuum generation and sub-two-cycle self-compression of mid-infrared filaments in dielectrics,” Opt. Lett. **40**, 1069-1072 (2015).
10. R. Šuminas, A. Marcinkevičiūtė, G. Tamošauskas, and A. Dubietis, “Even and odd harmonics-enhanced supercontinuum generation in polyscrystalline zinc-blende semiconductors,” J. Opt. Soc. Am. B **36**, A22–A27 (2019).
11. M. Durand, A. Houard, K. Lim, A. Durécu, O. Vasseur, and M. Richardson, “Study of filamentation threshold in zinc selenide,” Opt. Express **22**, 5852–5858 (2014).
12. O. Mouawad, P. Béjot, F. Billard, P. Mathey, B. Kibler, F. Désévédavy, G. Gadret, J.-C. Jules, O. Faucher, and F. Smektala, “Filament-induced visible-to-mid-IR supercontinuum in a ZnSe crystal: Towards multi-octave supercontinuum absorption spectroscopy,” Opt. Mater. **60**, 355–358 (2016).
13. R. Šuminas, G. Tamošauskas, N. Garejev, V. Jukna, A. Couairon, and A. Dubietis, “Multi-octave spanning nonlinear interactions induced by femtosecond filamentation in polycrystalline ZnSe,” Appl. Phys. Lett. **110**, 241106 (2017).
14. R. I. Grynko, G. C. Nagar, and B. Shim, “Wavelength-scaled laser filamentation in solids and plasma-assisted subcycle light-bullet generation in the long-wavelength infrared,” Phys. Rev. A **98**, 023844 (2018).
15. X. Gai, Y. Yu, B. Kuyken, P. Ma, S. J. Madden, J. V. Campenhout, P. Verheyen, G. Roelkens, R. Baets, and B. Luther-Davies, “Nonlinear absorption and refraction in crystalline silicon in the mid-infrared,” Laser Photon. Rev. **7**, 1054–1064 (2013).
16. T. Wang, N. Venkatram, J. Gosciniak, Y. Cui, G. Qian, W. Ji, and D. T. H. Tan, “Multi-photon absorption and third-order nonlinearity in silicon at mid-infrared wavelengths,” Opt. Express **21**, 32192–32198 (2013).
17. J. Leuthold, C. Koos, and W. Freude, “Nonlinear silicon photonics,” Nat. Photon. **4**, 535–544 (2010).
18. M. Borghi, C. Castellan, S. Signorini, A. Trenti, and L. Pavesi, “Nonlinear silicon photonics,” J. Opt. **19**, 093002 (2017).
19. Y. Zou, S. Chakravarty, C.-J. Chung, X. Xu, and R. T. Chen, “Mid-infrared silicon photonic waveguides and devices,” Photon. Res. **6**, 254–276 (2018).
20. R. K. W. Lau, M. R. E. Lamont, A. G. Griffith, Y. Okawachi, M. Lipson, and A. L. Gaeta, “Octave-spanning mid-infrared supercontinuum generation in silicon nanowaveguides,” Opt. Lett. **39**, 4518–4521 (2014).
21. B. Kuyken, T. Ideguchi, S. Holzner, M. Yan, T. W. Hänsch, J. Van Campenhout, P. Verheyen, S. Coen, F. Leo, R. Baets, G. Roelkens, and N. Picqué, “An octave-spanning mid-infrared frequency comb generated in a silicon nanophotonic wire waveguide,” Nat. Commun. **6**, 6310 (2015).
22. N. Singh, D. D. Hudson, Y. Yu, C. Grillet, S. D. Jackson, A. Casas-Bedoya, A. Read, P. Atanackovic, S. G. Duvall, S. Palomba, B. Luther-Davies, S. Madden, D. J. Moss, and B. J. Eggleton, “Midinfrared supercontinuum generation from 2 to 6 μm in a silicon nanowire,” Optica **2**, 797–801 (2015).
23. A. Blanco-Redondo, C. Husko, D. Eades, Y. Zhang, J. Li, T. F. Krauss, and B. J. Eggleton, “Observation of soliton compression in silicon photonic crystals”, Nat. Commun. **5**, 3160 (2014).
24. V. V. Kononenko, V. V. Konov, and E. M. Dianov, “Delocalization of femtosecond radiation in silicon,” Opt. Lett. **37**, 3369–3371 (2012).
25. A. Mouskeftaras, A. V. Rode, R. Clady, M. Sentis, O. Utéza, and D. Grojo, “Self-limited underdense microplasmas in bulk silicon induced by ultrashort laser pulses,” Appl. Phys. Lett. **105**, 191103 (2014).
26. E. V. Zavedeev, V. V. Kononenko, and V. I. Konov, “Delocalization of femtosecond laser radiation in crystalline Si in the mid-IR range,” Laser Phys. **26**, 016101 (2016).
27. A. Mouskeftaras, M. Chanal, M. Chambonneau, R. Clady, O. Utéza, and D. Grojo, “Direct measurement of ambipolar diffusion in bulk silicon by ultrafast infrared imaging of laser-induced microplasmas,” Appl. Phys. Lett. **108**, 041107 (2016).
28. M. Chanal, V. Yu. Fedorov, M. Chambonneau, R. Clady, S. Tzortzakis, and D. Grojo, “Crossing the threshold of ultrafast laser writing in bulk silicon,” Nat. Commun. **8**, 773 (2017).
29. G. Tamošauskas, G. Beresnevičius, D. Gadonas, and A. Dubietis, “Transmittance and phase matching of BBO crystal in the $3 - 5\ \mu$m range and its application for characterization of mid-infrared laser pulses,” Opt. Mater. Express **8**, 1410–1418 (2018).
30. K. Misiakos and D. Tsamakis, “Accurate measurements of the silicon intrinsic carrier density from 78 to 340 K,” J. Appl. Phys. **74**, 3293–3297 (1993).
31. A. Brodeur and S. L. Chin, “Band-gap dependence of the ultrafast white-light continuum,” Phys. Rev. Lett. **80**, 4406–4409 (1998).
32. M. Kolesik, G. Katona, J. V. Moloney, and E. M. Wright, “Physical factors limiting the spectral extent and band gap dependence of supercontinuum generation,” Phys. Rev. Lett. **91**, 043905 (2003).
33. A. Jarnac, G. Tamošauskas, D. Majus, A. Houard, A. Mysyrowicz, A. Couairon, and A. Dubietis, “Whole life cycle of femtosecond ultraviolet filaments in water,” Phys. Rev. A **89**, 033809 (2014).
34. E. Yablonovitch and N. Bloembergen, “Avalanche ionization and the limiting diameter of filaments induced by light pulses in transparent media”, Phys. Rev. Lett. **29**, 907–910 (1972).

A6

FEMTOSECOND INFRARED SUPERCONTINUUM GENERATION IN 6H-SIC

A. Šuminienė, V. Jukna, R. Šuminas, G. Tamošauskas,
A. Dubietis

OSA Continuum **4**(3), 911–917 (2021)

Reprinted with permission from OSA Continuum

Femtosecond infrared supercontinuum generation in 6H-SiC crystal

Agnė Šuminienė,* Vytautas Jukna, Rosvaldas Šuminas, Gintaras Tamošauskas, and Audrius Dubietis

Laser Research Center, Vilnius University, Saulėtekio Ave. 10, LT- 10223, Vilnius, Lithuania
**agne.suminiene@ff.stud.vu.lt*

Abstract: We report on supercontinuum generation in silicon carbide (6H-SiC), pumped by tunable femtosecond pulses in the wavelength range of 1.3 - 2.4 µm, which cover the regions of normal, zero, and anomalous group velocity dispersion of the material. More than an octave spanning infrared supercontinuum spectra were measured, demonstrating almost constant blue cut-offs around 0.9 µm. Low energy thresholds for supercontinuum generation (depending on the pump wavelengths, but generally below 200 nJ) were demonstrated due to large nonlinear refractive index of the material ($n_2 = 97 \pm 19 \times 10^{-16}$ cm^2/W), which was experimentally evaluated by measurement of the nonlinear transmission at 2.0 µm.

1. Introduction

Ultrashort, ultrabroadband laser pulses in the near- and mid-infrared spectral region are on demand for applications in vibrational spectroscopy and for development of optical parametric chirped pulse amplification and pulse compression techniques [1–5]. Femtosecond supercontinuum (SC) generation in solid-state media is a unique nonlinear phenomenon which currently serves as a robust and well-established technique for producing ultrabroadband coherent radiation in the optical range [6,7]. Typically, supercontinuum generation is performed in wide-bandgap dielectric crystals, out of these, sapphire and YAG serve as most common and most reliable nonlinear materials [8,9]. For what concerns supercontinuum generation in sole infrared spectral range, narrow-bandgap dielectric crystals such as mixed thallous halides (KRS-5 and KRS-6) [10–12], and strontium barium niobate (SBN) [13] were shown to provide a viable alternative. More than that, semiconductor crystals have emerged as promising nonlinear materials for that purpose due to a combination of attractive optical properties such as large nonlinear index of refraction, wider transparency into the mid-infrared and zero group velocity dispersion (GVD) wavelengths that are shifted to the longer wavelengths compared to dielectrics. So far, supercontinuum generation via femtosecond filamentation has been demonstrated in bulk semiconductor crystals such as ZnS, ZnSe [14–18] and Si [19] where multioctave SC spectra extending from the near- to mid-infrared range were produced.

Silicon carbide (SiC) is a semiconductor material with high potential for hosting nonlinear interactions in this spectral region. In nonlinear photonics, SiC, as compared to silicon, has a considerable advantage due to its more than twice larger bandgap and hence the reduced nonlinear absorption in the near and mid-infrared spectral range. SiC can be grown in over 200 polytypes with different optical parameters and crystalline structures. However, the three commonly used and widely available polytypes are 3C-, 4H-, and 6H-SiC, with the former one being cubic, and the latter two hexagonal, uniaxial crystals. More importantly, 4H-SiC and 6H-SiC possess relatively large second-order nonlinearities [20]. More recently, dispersion of third-order nonlinearities has been calculated for the three SiC polytypes unveiling a large nonlinear refractive index, comparable to that of silicon: the obtained values were within the range from 0.5 to 6.3 $\times 10^{-14}$ cm^2/W in the 0.5-5 µm spectral region [21]. Experiments exploiting

#419234 https://doi.org/10.1364/OSAC.419234
Journal © 2021 Received 7 Jan 2021; revised 5 Feb 2021; accepted 8 Feb 2021; published 25 Feb 2021

large second and third order nonlinearities of SiC demonstrated spectral broadening [22] and optical parametric oscillation [23] in waveguide and microresonator geometries, respectively, and broadband difference frequency generation [24] and optical parametric amplification [25] in bulk.

In this paper we study supercontinuum generation in 6H-SiC with femtosecond wavelength tunable laser pulses. We demonstrate that smooth supercontinuum spectra with fairly stable cut-off wavelengths around 0.9 µm are generated when tuning the wavelength of pump pulses from normal to anomalous GVD region of the crystal. We also measure the nonlinear transmission of the light filament in 6H-SiC sample which is then used to estimate the nonlinear refractive index of the material at 2 µm.

2. Experimental methods and parameters

The experiments were performed using an optical parametric amplifier (OPA, Topas-Prime, Light Conversion) pumped by an amplified Ti:sapphire laser system (Spitfire-PRO, Newport-Spectra Physics). In the experiment either signal or idler wave from the OPA was used, providing the tuning range of the pump pulses from 1.2 to 2.4 µm. The experimental setup is sketched in Fig. 1. The pump pulses were loosely focused by a BaF_2 lens (L) with a focal length $f = 100$ mm onto the front face of the 5 mm-thick 6H-SiC sample with the optical axis aligned perpendicular to the propagation direction of the incident beam. Variable neutral density filter (VDF) allowed fine tuning of the pump pulse energy at the entrance of the sample. The output face of the sample was imaged onto the input slit of a home built scanning prism spectrometer (SPS) using a pair of silver-coated parabolic mirrors positioned in a $4f$ imaging setup. The SPS was equipped with Si and InAsSb detectors enabling an effective detection range of 0.2 - 5.8 µm. For energy transmission measurements, a fraction of the pump beam energy was reflected from a thin fused silica plate (P) and directed to a PbSe detector (RD), which served as a reference, whereas the output beam was directed into a pyroelectric detector (D).

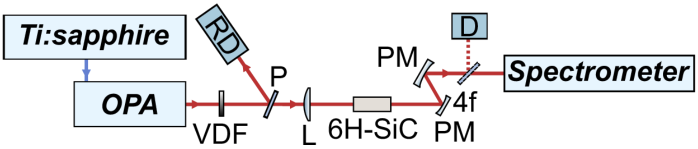

Fig. 1. Schematic of the experiment: VDF - variable neutral density filter, P - fused silica plate, RD - reference PbSe detector, L - lens, PM - parabolic mirror, D - pyroelectric detector.

Table 1 presents the relevant parameters of 6H-SiC crystal which are compared with other nonlinear media used for supercontinuum generation in the near to mid-IR spectral range. 6H-SiC possesses a useful combination of linear and nonlinear optical properties: a reasonable transparency range, large nonlinear refractive index and high optical damage threshold, that could be readily exploited for observation of filamentation phenomena and SC generation in particular. First of all, considering the bandgap of 6H-SiC, three to five photon absorption is expected in the range of available pump wavelengths, thus satisfying the threshold condition ($K \geq 3$ where K is the order of multiphoton absorption) for SC generation [26]. Secondly, compared to YAG, the bandgap of 6H-SiC is a few times smaller, which as a general rule of thumb, indicates that its optical damage threshold is significantly (around five times) lower. However, this is outweighed by the fact that the nonlinear index of refraction is expected to be around 15 times larger than that of YAG, which suggests a much lower critical power for self-focusing and hence the energy threshold for SC generation. Thirdly, the zero GVD wavelength of 6H-SiC is at 2.1 µm allowing the access to femtosecond filamentation in the anomalous GVD regime, characterized by simultaneous compression in space and time and light-bullet formation [27], which in turn yields generation of ultrabroadband, multioctave SC [28,29].

Table 1. Main parameters of 6H-SiC and some other nonlinear media used for supercontinuum generation in the near to mid-infrared: E_g is the energy bandgap, T is the transmission range, n_0 and n_2 are linear and nonlinear refractive indexes, respectively, λ_0 is the zero GVD wavelength, DT is the optical damage threshold for femtosecond pulses. The bandgap and transmission parameters together with damage thresholds for Si and ZnSe were taken from [30]. Linear refractive index values are given for 2 µm. 6H-SiC and ZnSe nonlinear refractive index values were estimated using the van Stryland analysis at 2 µm [31]. The references to other parameter values are given in the table.

Material	E_g (eV)	T (μm)	n_0	λ_0 (μm)	$n_2 \times 10^{-16}$ (cm^2/W)	DT (J/cm^2)
6H-SiC	2.6	0.5-4	2.5537(o); 2.5873(e) [24]	2.1	86	0.60 [32]
Si	1.12	1.1-6.5	3.4401 [33]	>23	270 [34]	0.55
ZnSe	2.71	0.5-20	2.4318 [35]	4.8	74	0.53
YAG	6.5	0.21-5.2	1.8005 [36]	1.6	6.2 [37]	3 [38]

3. Results and discussion

Figure 2 shows the dynamics of spectral broadening versus the pump pulse energy measured using 93 fs pulses with a central wavelength of 2 µm, which falls close to the zero GVD wavelength of 6H-SiC. An explosive spectral broadening is observed above the threshold energy of 73 nJ, where a smooth SC spectrum spanning almost the entire near-IR spectral region and extending into the mid-infrared is produced. The low SC generation energy threshold is determined by the large nonlinear refractive index of 6H-SiC, see Table 1. A fairly constant width of the SC spectrum is maintained with further increase of the pump pulse energy, until a second burst of spectral broadening is observed at approximately 180 nJ, accompanied by spectral modulation that indicates the refocusing of the filament.

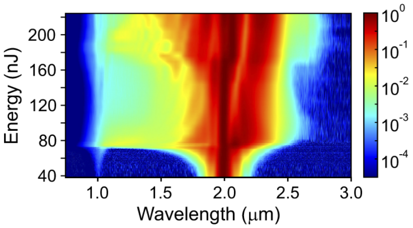

Fig. 2. Measured dynamics of spectral broadening in 6H-SiC crystal recorded with 93 fs, 2 µm pump pulses as a function of pulse energy. Logarithmic intensity scale is used in order to highlight fine spectral features.

Below the SC generation threshold, a faint but clearly distinguishable signal with a center wavelength around 1 µm is observed, which is attributed to phase-mismatched second harmonic generation. Since 6H-SiC is a positive uniaxial crystal, the pump pulse polarization was intentionally set to be ordinary to minimize second harmonic generation in order to avoid spectral "contamination". It should be noted that at the OPA output the signal (1.3 and 1.5 µm) and the idler (2.0 and 2.4 µm) waves are of orthogonal polarizations due to type-II phase matching in the OPA crystal. Therefore, the polarization of the idler wave was rotated by 90 degrees (by means of a periscope) to be identical to that of the signal wave (to be ordinarily polarized in 6H-SiC sample) in order to have the same SC pump polarization that suppresses second harmonic generation with all used pump wavelengths.

Figure 3 presents the SC spectra measured with four different wavelengths: 1.3, 1.5, 2.0 and 2.4 µm, and using pump pulse energies of 55, 70, 90 and 180 nJ, respectively, at which the spectral broadening saturates without filament refocusing. Notice an apparent change of the width and the shape of SC spectra from the red-shifted to symmetric and eventually to the blue-shifted, when the pump wavelength is tuned from normal to anomalous GVD regions of the nonlinear material [the zero GVD wavelength is 2.1 µm, see Fig. 4(a)]. More specifically, with 1.3 µm pump pulses, the measured SC spectrum exhibits a red-shift and covers the wavelength range from 0.85 to 2.13 µm, as evaluated at the 10^{-4} intensity level, see Fig. 3(a). A slightly broader and symmetric SC spectrum in the wavelength range of 0.87-2.40 µm was produced with 1.5 µm pump pulses, as shown in Fig. 3(b). The broadest SC spectra with strongly pronounced blue-shifts were measured in the regions of near-zero and anomalous GVD, with pump wavelenghts of 2.0 and 2.4 µm, as illustrated in Figs. 3(c) and 3(d), respectively. In the first case, the SC spectrum covers the 0.91-2.75 µm wavelength range, while in the latter case the SC spectrum extends from 0.92 to 3.21 µm and spans 1.8 optical octaves. The shapes of all measured SC spectra are smooth and do not contain any significant dips or detached peaks. Also note the generally low energies of the pump pulses (varying from 55 to 180 nJ) required to achieve a fully evolved spectral broadening without the onset of filament refocusing. The apparent increase of the pump pulse energy with the wavelength follows fairly well the square wavelength dependence of the critical power for self-focusing.

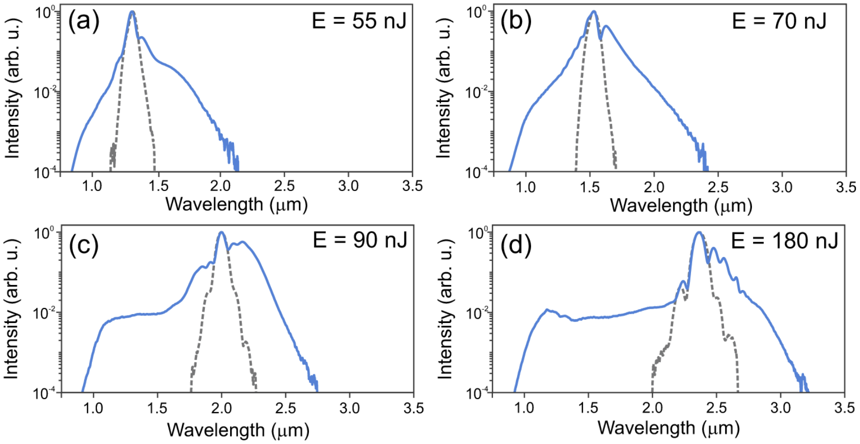

Fig. 3. Supercontinuum spectra generated in 6H-SiC using pump pulses with wavelengths of (a) 1.3 µm, (b) 1.5 µm, (c) 2.0 µm, and (d) 2.4 µm. The energies of the pump pulses are indicated within the figures. The input spectra are depicted by grey dashed curves.

The results are summarized in Fig. 4. Figure 4(a) illustrates the GVD curve of 6H-SiC, indicating the wavelengths at which the whole set of spectral measurements was performed. Figure 4(b) shows the measured SC blue-shifts defined at the 10^{-4} intensity level as a function of the pump pulse wavelength. The increase of the spectral blue shift with the increase of the pump wavelength could be attributed to a higher value of the clamped intensity, as the order of multiphoton absorption gradually increases from 3 at 1.3 µm to 5 at 2.4 µm [26].

Finally, in order to obtain an experimental nonlinear refractive index value, we have measured the energy transmission through 6H-SiC sample of 5 mm thickness. The transmission is affected by the nonlinear losses (multiphoton absorption and absorption by the free electron plasma), which increase significantly as the intensity of pump beam increases due to self-focusing, and which are the largest at the nonlinear focus. Therefore, the peak of the fractional losses (-dT/dE) derived from the transmission curve may be used to accurately determine the onset of filamentation, see [10] for details. The normalized energy transmission curve measured using pump pulses

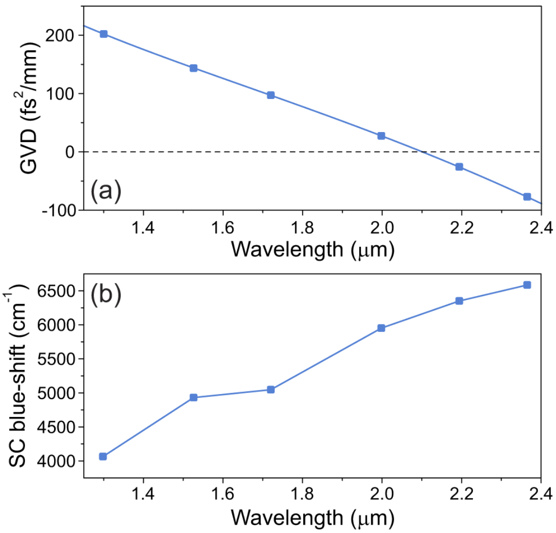

Fig. 4. (a) GVD of 6H-SiC and (b) spectral blue-shift of the SC versus the pump wavelength.

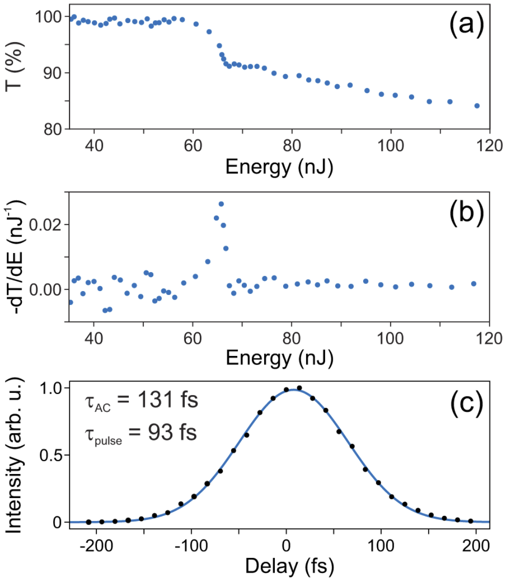

Fig. 5. (a) Normalized energy transmission of a 5 mm-thick 6H-SiC sample versus the pump pulse energy. (b) Fractional losses, where the maximum indicates that the nonlinear focus is positioned exactly at the output face of the sample. (c) Measured intensity autocorrelation function of 2.0 μm pump pulses.

at 2.0 µm, is depicted in Fig. 5(a). Figure 5(b), shows the calculated fractional losses, with a peak at 66 nJ, indicating that the nonlinear focus is produced exactly at the output face of the sample. In other words, this suggests that the self-focusing distance is equal to the length of the sample (5 mm). Assuming the input parameters: the pulse duration of 93 fs at full width at half maximum, see Fig. 5(c), and the beam radius of 53 µm at the $1/e^2$ intensity level at the entrance face of the sample, measured by means of a knife method, and using the Marburger's law [39], we found a nonlinear refractive index value of $n_2 = 97 \pm 19 \times 10^{-16}$ cm^2/W, at 2.0 µm. The measured n_2 value agrees well with the expected one provided in Table 1 and the small discrepancy between the measured and calculated values could be attributed to the margin of error.

4. Conclusion

In conclusion, we have shown that 6H-SiC crystal is an excellent nonlinear material for supercontinuum generation in the near- to mid-infrared spectral region. We demonstrated the generation of smooth, more than an octave-spanning SC spectra produced by femtosecond filamentation in the normal, zero and anomalous GVD regions of the material. We also experimentally evaluated the nonlinear index of refraction of 6H-SiC at 2.0 µm by the measurement of nonlinear transmission and applying the Marburger's law. The obtained value ($n_2 = 97 \pm 19 \times 10^{-16}$ cm^2/W) coincides fairly well with the theoretically calculated one and is supported by the observed low energy thresholds for supercontinuum generation.

Funding. European Regional Development Fund (1.2.2-LMT-K-718-02-0017).

Acknowledgments. The authors thank Dr. Irmantas Kašalynas from Center for Physical Sciences and Technology for providing the 6H-SiC sample. This work has received funding from European Regional Development Fund (project No1.2.2-LMT-K-718-02-0017) under grant agreement with the Research Council of Lithuania (LMTLT).

Disclosures. The authors declare no conflicts of interest.

References

1. U. Megerle, I. Pugliesi, C. Schriever, C. F. Sailer, and E. Riedle, "Sub-50 fs broadband absorption spectroscopy with tunable excitation: putting the analysis of ultrafast molecular dynamics on solid ground," Appl. Phys. B **96**(2-3), 215–231 (2009).
2. G. Auböck, C. Consani, R. Monni, A. Cannizzo, F. Van Mourik, and M. Chergui, "Femtosecond pump/supercontinuum-probe setup with 20 kHz repetition rate," Rev. Sci. Instrum. **83**(9), 093105 (2012).
3. C. Calabrese, A. M. Stingel, L. Shen, and P. B. Petersen, "Ultrafast continuum mid-infrared spectroscopy: probing the entire vibrational spectrum in a single laser shot with femtosecond time resolution," Opt. Lett. **37**(12), 2265–2267 (2012).
4. P. Rigaud, A. Van de Walle, M. Hanna, N. Forget, F. Guichard, Y. Zaouter, K. Guesmi, F. Druon, and P. Georges, "Supercontinuum-seeded few-cycle mid-infrared OPCPA system," Opt. Express **24**(23), 26494–26502 (2016).
5. P. He, Y. Liu, K. Zhao, H. Teng, X. He, P. Huang, H. Huang, S. Zhong, Y. Jiang, S. Fang, X. Hou, and Z. Wei, "High-efficiency supercontinuum generation in solid thin plates at 0.1 TW level," Opt. Lett. **42**(3), 474–477 (2017).
6. A. Dubietis, G. Tamošauskas, R. Šuminas, V. Jukna, and A. Couairon, "Ultrafast supercontinuum generation in bulk condensed media," Lith. J. Phys. **57**(3), 113–157 (2017).
7. A. Dubietis and A. Couairon, *Ultrafast supercontinuum generation in transparent solid-state media* (Springer, 2019).
8. J. Darginavičius, D. Majus, V. Jukna, N. Garejev, G. Valiulis, A. Couairon, and A. Dubietis, "Ultrabroadband supercontinuum and third-harmonic generation in bulk solids with two optical-cycle carrier-envelope phase-stable pulses at 2 µm," Opt. Express **21**(21), 25210–25220 (2013).
9. M. Bradler, P. Baum, and E. Riedle, "Femtosecond continuum generation in bulk laser host materials with sub-μJ pump pulses," Appl. Phys. B **97**(3), 561–574 (2009).
10. A. Marcinkevičiūtė, G. Tamošauskas, and A. Dubietis, "Supercontinuum generation in mixed thallous halides KRS-5 and KRS-6," Opt. Mater. **78**, 339–344 (2018).
11. K. Liu, H. Liang, S. Qu, W. Li, X. Zou, Y. Zhang, and Q. J. Wang, "High-energy mid-infrared intrapulse difference-frequency generation with 5.3% conversion efficiency driven at 3 µm," Opt. Express **27**(26), 37706–37713 (2019).
12. S. Qu, G. C. Nagar, W. Li, K. Liu, X. Zou, S. H. Luen, D. Dempsey, K.-H. Hong, Q. J. Wang, Y. Zhang, B. Shim, and H. Liang, "Long-wavelength-infrared laser filamentation in solids in the near-single-cycle regime," Opt. Lett. **45**(8), 2175–2178 (2020).

13. R. Šuminas, N. Garejev, A. Šuminienė, V. Jukna, G. Tamošauskas, and A. Dubietis, "Femtosecond filamentation, supercontinuum generation, and determination of n_2 in polycrystalline SBN," J. Opt. Soc. Am. B **37**(5), 1530–1534 (2020).
14. H. Liang, P. Krogen, R. Grynko, O. Novak, C.-L. Chang, G. J. Stein, D. Weerawarne, B. Shim, F. X. Kärtner, and K.-H. Hong, "Three-octave-spanning supercontinuum generation and sub-two-cycle self-compression of mid-infrared filaments in dielectrics," Opt. Lett. **40**(6), 1069–1072 (2015).
15. R. Šuminas, G. Tamošauskas, G. Valiulis, V. Jukna, A. Couairon, and A. Dubietis, "Multi-octave spanning nonlinear interactions induced by femtosecond filamentation in polycrystalline ZnSe," Appl. Phys. Lett. **110**(24), 241106 (2017).
16. R. Šuminas, A. Marcinkevičiūtė, G. Tamošauskas, and A. Dubietis, "Even and odd harmonics- semiconductors," J. Opt. Soc. Am. B **36**(2), A22–A27 (2019).
17. O. Mouawad, P. Béjot, F. Billard, P. Mathey, B. Kibler, F. Désévédavy, G. Gadret, J.-C. Jules, O. Faucher, and F. Smektala, "Filament-induced visible-to-mid-IR supercontinuum in a ZnSe crystal: Towards multi-octave supercontinuum absorption spectroscopy," Opt. Mater. **60**, 355–358 (2016).
18. K. Werner, M. G. Hastings, A. Schweinsberg, B. L. Wilmer, D. Austin, C. M. Wolfe, M. Kolesik, T. R. Ensley, L. Vanderhoef, A. Valenzuela, and E. Chowdhury, "Ultrafast mid-infrared high harmonic and supercontinuum generation with n_2 characterization in zinc selenide," Opt. Express **27**(3), 2867–2885 (2019).
19. A. Marcinkevičiūtė, V. Jukna, R. Šuminas, N. Garejev, G. Tamošauskas, and A. Dubietis, "Femtosecond filamentation and supercontinuum generation in bulk silicon," Opt. Lett. **44**(6), 1343–1346 (2019).
20. H. Sato, M. Abe, I. Shoji, J. Suda, and T. Kondo, "Accurate measurements of second-order nonlinear optical coefficients of 6H and 4H silicon carbide," J. Opt. Soc. Am. B **26**(10), 1892–1896 (2009).
21. F. De Leonardis, R. A. Soref, and V. M. Passaro, "Dispersion of nonresonant third-order nonlinearities in Silicon Carbide," Sci. Rep. **7**(1), 40924 (2017).
22. J. Cardenas, M. Yu, Y. Okawachi, C. B. Poitras, R. K. Lau, A. Dutt, A. L. Gaeta, and M. Lipson, "Optical nonlinearities in high-confinement silicon carbide waveguides," Opt. Lett. **40**(17), 4138–4141 (2015).
23. M. A. Guidry, K. Y. Yang, D. M. Lukin, A. Markosyan, J. Yang, M. M. Fejer, and J. Vučković, "Optical parametric oscillation in silicon carbide nanophotonics," Optica **7**(9), 1139–1142 (2020).
24. S. Wang, M. Zhan, G. Wang, H. Xuan, W. Zhang, C. Liu, C. Xu, Y. Liu, Z. Wei, and X. Chen, "4H-SiC: a new nonlinear material for midinfrared lasers," Laser Photonics Rev. **7**(5), 831–838 (2013).
25. H.-T. Fan, C.-H. Xu, Z.-H. Wang, G. Wang, C.-J. Liu, J.-K. Liang, X.-L. Chen, and Z.-Y. Wei, "Generation of broadband 17-μJ mid-infrared femtosecond pulses at 3.75 µm by silicon carbide crystal," Opt. Lett. **39**(21), 6249–6252 (2014).
26. A. Brodeur and S. Chin, "Band-gap dependence of the ultrafast white-light continuum," Phys. Rev. Lett. **80**(20), 4406–4409 (1998).
27. M. Durand, A. Jarnac, A. Houard, Y. Liu, S. Grabielle, N. Forget, A. Durécu, A. Couairon, and A. Mysyrowicz, "Self-guided propagation of ultrashort laser pulses in the anomalous dispersion region of transparent solids: a new regime of filamentation," Phys. Rev. Lett. **110**(11), 115003 (2013).
28. F. Silva, D. Austin, A. Thai, M. Baudisch, M. Hemmer, D. Faccio, A. Couairon, and J. Biegert, "Multi-octave supercontinuum generation from mid-infrared filamentation in a bulk crystal," Nat. Commun. **3**(1), 807 (2012).
29. S. Chekalin, A. Dormidonov, V. Kompanets, E. Zaloznaya, and V. Kandidov, "Light bullet supercontinuum," J. Opt. Soc. Am. B **36**(2), A43–A53 (2019).
30. M. J. Weber, *Handbook of optical materials*, vol. 19 (CRC press, 2002).
31. M. Sheik-Bahae, D. C. Hutchings, D. J. Hagan, and E. W. Van Stryland, "Dispersion of bound electron nonlinear refraction in solids," IEEE J. Quantum Electron. **27**(6), 1296–1309 (1991).
32. G. L. DesAutels, C. Brewer, M. Walker, S. Juhl, M. Finet, S. Ristich, M. Whitaker, and P. Powers, "Femtosecond laser damage threshold and nonlinear characterization in bulk transparent SiC materials," J. Opt. Soc. Am. B **25**(1), 60–66 (2008).
33. J. Leuthold, C. Koos, and W. Freude, "Nonlinear silicon photonics," Nat. Photonics **4**(8), 535–544 (2010).
34. X. Gai, Y. Yu, B. Kuyken, P. Ma, S. J. Madden, J. Van Campenhout, P. Verheyen, G. Roelkens, R. Baets, and B. Luther-Davies, "Nonlinear absorption and refraction in crystalline silicon in the mid-infrared," Laser Photonics Rev. **7**(6), 1054–1064 (2013).
35. T. Amotchkina, M. Trubetskov, D. Hahner, and V. Pervak, "Characterization of e-beam evaporated Ge, YbF_3, ZnS, and LaF_3 thin films for laser-oriented coatings," Appl. Opt. **59**(5), A40–A47 (2020).
36. D. E. Zelmon, D. L. Small, and R. Page, "Refractive-index measurements of undoped yttrium aluminum garnet from 0.4 to 5.0 µm," Appl. Opt. **37**(21), 4933–4935 (1998).
37. R. Adair, L. Chase, and S. A. Payne, "Nonlinear refractive index of optical crystals," Phys. Rev. B **39**(5), 3337–3350 (1989).
38. S. Xu, J. Qiu, T. Jia, C. Li, H. Sun, and Z. Xu, "Femtosecond laser ablation of crystals SiO_2 and YAG," Opt. Commun. **274**(1), 163–166 (2007).
39. J. H. Marburger, "Self-focusing: theory," Prog. Quantum Electron. **4**, 35–110 (1975).

Vilnius University Press
Saulėtekio al. 9, LT-10222 Vilnius
e-mail: info@leidykla.vu.lt,
www.leidykla.vu.lt
Print run copies 15